C.P. No. 918

C.P. No. 918

MINISTRY OF AVIATION

AERONAUTICAL RESEARCH COUNCIL
CURRENT PAPERS

Free-flight Model Measurements of the Dynamic Stability of a Supersonic Strike Aircraft (TSR2)

by

G. K. Hunt, B.Sc.(Eng.), A.F.R.Ae.S.,

with an Appendix by A. Jean Ross, Ph.D.

LONDON· HER MAJESTY'S STATIONERY OFFICE
1967
PRICE 14s 6d NET

U.D.C. No. 533.6.013.412/413 : 533.6.011.35/5

C.P. No. 918*
November 1965

FREE-FLIGHT MODEL MEASUREMENTS OF THE DYNAMIC STABILITY OF A SUPERSONIC STRIKE AIRCRAFT (TSR2)

by

G. K. Hunt, B.Sc.(Eng.), A.F.R.Ae.S.,
with an Appendix by
A. Jean Ross, Ph.D.

SUMMARY

Longitudinal and lateral stability derivatives have been obtained in free flight from eight 1/12-scale models of the TSR2, at Mach numbers between 0·7 and 1·4 and Reynolds numbers between 7 and 15 million.

The measurements indicate some loss of longitudinal and lateral stability at transonic speeds, and the loss of yaw stiffness n_v is shown to be dependent on C_L. At supersonic speeds the sideslip derivatives ℓ_v, n_v and y_v diminish continuously with increasing Mach number.

The aerodynamic effects of a sudden engine failure were produced at $M = 1·3$ on two models, but the response was negligible. The sideslip derivatives n_v and y_v were considerably reduced at transonic speeds by flying with a simulated idle engine.

Four of the models autorotated after lateral disturbances. Some of the characteristics of this behaviour have been determined from the flight records and by simulating the motion on an analogue computer.

---

*Replaces R.A.E. Technical Report No.65253 - A.R.C. 28056

CONTENTS

ILLUSTRATIONS

ILLUSTRATIONS (Contd)

1 INTRODUCTION

The TSR2 was a military strike aircraft designed to operate at transonic speeds at very low altitude and at supersonic speeds at high altitudes. It had a thin delta wing, large all-moving tail surfaces, and a long body containing two turbojet engines, most of the fuel and the war load.

Extensive wind-tunnel tests (for example, Refs.1,2,3,4) were carried out while the aircraft was being designed, but no dynamic stability measurements were obtained and the effects of tunnel constraints and support interference on some of the static stability measurements were uncertain. There was no experience of comparable configurations on which to draw, and therefore a complementary programme of free-flight model tests was undertaken, to determine some of the more important dynamic stability derivatives and to check the tunnel measurements.

In particular there were two static stability characteristics about which further information was required. The transonic tunnel tests had shown the pitching-moment derivative m_w to be dependent on the angle of incidence as well as on Mach number. At these speeds the uncertainty of the tunnel measurements was at its greatest, and the real magnitude of the incidence effect was obscured. At supersonic speeds some of the tunnel tests had indicated an unexpectedly large reduction in the yawing-moment derivative n_v with increasing Mach number. This gave rise to some anxiety, because it implied a need to increase the artificial directional stiffness provided by the autopilot. More stringent operational restrictions would then have to be imposed if the autopilot should fail.

One aspect of the dynamic behaviour of the aircraft at supersonic speeds which proved impossible to estimate satisfactorily was the effect of the sudden failure of one engine. As well as producing asymmetric changes in thrust and drag, this would cause yawing moments due to intake shock movements and spillage, and might produce severe loads on the aircraft.

The free-flight tests were planned in two groups, in which the principal objectives were respectively longitudinal stability measurements at Mach numbers up to 1·5 and lateral stability measurements at Mach numbers up to 1·8. The test schedule is set out in Table 1. The longitudinal-stability models were flown at different lift coefficients, to provide a measure of the dependence of m_w on the angle of incidence, and two of the lateral-stability models were equipped with a device to simulate engine failure. The experimental technique was, essentially, to disturb each model at several different Mach numbers and to measure and analyse the response to each disturbance. The oscillatory motion of the models was influenced by aerodynamic and inertia cross-coupling, but usually these effects were important only at the largest amplitudes. When the analysis was confined to moderate amplitudes it was generally possible to treat the longitudinal short-period oscillation and the Dutch roll separately, and thus to evaluate the derivatives associated with uncoupled motion. This method yielded values of the normal-force and lateral-force derivatives z_w and y_v, the rolling-moment derivative ℓ_v, the pitching and yawing stiffness derivatives m_w and n_v, and the rotary damping derivatives in roll, pitch and yaw ℓ_p, $(m_q + m_{\dot{w}})$ and n_r.

The models were not dynamically similar to the aircraft and their roll behaviour was adversely affected by inertia cross-coupling. If the rate of roll exceeded either of the uncoupled oscillation frequencies it increased rapidly until the model settled into a very fast, stable autorotation. At the highest Mach numbers the smallest practicable lateral disturbance induced autorotation, so the high-speed tests had to be abandoned and all measurements were confined to Mach numbers below 1·5. Even at these Mach numbers autorotation was not entirely avoided, and altogether four of the eight models autorotated during at least part of their respective flights. Therefore, although the object of the tests was to measure stability derivatives, the opportunity was taken to analyse the autorotation and to compare its measured characteristics with calculations.

The models were flown at R.A.E. Aberporth between February 1962 and February 1964. Measurements of the stability derivatives were obtained within the range of Mach numbers between 0·7 and 1·4 at Reynolds numbers, based on the mean chord, between 7 and 15 million.

2 DESCRIPTION OF THE MODELS

2.1 Geometry

Eight models were built, to a common scale of 1/12. The first was intended primarily to prove the launching technique, the flight behaviour and the instrumentation. Its geometry differed from that of the aircraft in several details and, for ease of manufacture, its construction was slightly simplified. The remaining seven models represented the external geometry of the aircraft, and are illustrated in Figs.1 and 2. The only details omitted from the models were the boundary-layer diverters at the intakes, and small excrescences such as fairings over flap hinges. The horizontal datum of the models corresponds to the Horizontal Fuselage Datum of the full-scale aircraft. The essential characteristics of all the models are given in Table 2.

The aircraft had movable centre bodies at the intakes, to enable the intake mass flow to be matched to engine requirements under various flight conditions. The model centre bodies were fixed in a position representing the aircraft configuration at $M = 2$. The flow through the models was regulated by choosing a tailpipe cross-section area which would choke at supersonic speeds and allow the intake to run critically, i.e. with the conical shock on the lip, at $M = 2$. At the lower Mach numbers of the free-flight tests the shock system would have been forward of the lip and some spillage must have occurred. The models carried a pyrotechnic flare inside each tailpipe to facilitate visual tracking from the ground.

The tail surfaces were fixed, with a small differential angle between the two halves of each tailplane. A mean angle was chosen for each model to produce the required longitudinal trim; the differential angle, which was less than half a degree, ensured that the model performed a barrel roll about a ballistic trajectory and did not stray outside the safety limits of the range.

2.2 Construction

Although the models were geometrically similar to the aircraft they were not intended to be dynamically similar. Construction was simple and sturdy, to produce models that were as nearly rigid as possible. Each model was built around a cast magnesium-alloy box, which occupied the space between the ducts and held most of the instrumentation (Fig.2(d)). A vertical aluminium-alloy plate projected forward from the box and formed a load-bearing spine through the forward part of the body (Fig.2(e)). The parts of the rear body which carried the tail loads were cast in magnesium alloy, but the more lightly stressed parts of the outer walls of the ducts and the forward part of the body were moulded in resin-bonded glass cloth, with local reinforcements of metal. The wing and tail surfaces were machined from solid aluminium alloy. All joints in the ducts were sealed. The sides of the forebody were detachable, and this enabled lead ballast to be attached to the spine of the complete model to adjust its c.g. position (Fig.2(e)).

3 EXPERIMENTAL TECHNIQUE

The models were launched from the ground and reached their maximum velocity in about 3 seconds (Fig.6). The booster rockets (Fig.2(c)) were detached when they stopped thrusting and the experimental measurements were made while the models were decelerating in free flight. Boundary-layer transition was allowed to occur naturally.

3.1 Pulse rockets and engine-failure simulator

Every model was equipped with 18 or 20 single-shot pulse rockets in the forward part of the body, attached to the central spine (Fig.2(e)). They were fired at predetermined times through ports in the body skin, downwards to excite the longitudinal short-period oscillation of the model and sideways to excite the Dutch roll. The firing sequence, which was generally different for each model, was accomplished by means of a sequence switch driven by a clock.

In each of the first five models the clock was started by an inertia trip actuated by the initial acceleration of the model, and the firing circuit included two arming switches that were closed by sustained longitudinal acceleration. Thus three components were designed to function only after the model had left the ground, when it was too late to remedy a failure. After model 3 had suffered a clock failure in flight and its replacement, model 5, had flown without a single pulse rocket being fired, the firing system was changed. In each of the last three models the entire firing circuit was duplicated, and both clocks were started by remote control before the model left the ground.

Two of the models, Nos.4 and 7, were equipped with a device for simulating the sudden failure of one engine in flight. This consisted of a perforated door, freely hinged to the inboard wall of the starboard duct. The door could be retracted completely by swinging it forward into a recess in the duct wall, where it was secured by a spring clip. The model was launched with the door retracted and, at a predetermined time, an explosive actuator was fired to release the door from the clip and push it out of the recess. Then the kinetic pressure of the air flowing through the duct slammed the door into position across the duct and held it there for the rest of the flight. The door was near the maximum cross-section of the duct and produced 50 per cent blockage.

3.2 Instrumentation

Every model carried a radio-Doppler transponder to provide measurements of velocity, and standard R.A.E. 465 Mc/s telemetry equipment to provide measurements of pressure and acceleration. The ranges of measurement are set out in Table 3. None of the instrumentation was duplicated, but in the first three representative models (Nos.2,3 and 4) two normal accelerometers were installed at the c.g. One had a range of measurement chosen to cover the predicted maximum accelerations; the other had a high range to cover the larger accelerations associated with autorotation. The positions of the accelerometers in the individual models are set out in Table 4 and a typical arrangement is shown in Fig.3.

Analysis of the Dutch roll requires a knowledge of the amplitude and phase relationships between the roll, yaw and sideslip components. Therefore, in each of the models equipped to measure lateral stability (Nos.4,6,7 and 8) the three lateral accelerometers were matched to have the same response characteristics, so that corrections for instrument phase lags would be simplified.

In the first six models the instrumentation worked well, but in the last two models faults occurred in the data channel telemetering angular acceleration in roll. In model 7 it failed completely half a second after the model left the ground, and in model 8 it developed an intermittent fault which caused sudden changes of signal frequency to occur when the equipment was jolted by the firing of pulse rockets (Fig.4). However, subsequent laboratory experiments enabled the intermittent fault to be diagnosed, and its effects were corrected during analysis of the data without any appreciable loss of accuracy.

Fig.4 shows part of the record of telemetered data from model 8. Apart from the fault on the roll acceleration channel, this is a good example of the kind of record obtained from all the models and illustrates the flight behaviour clearly.

3.3 Pre-flight measurements

When each model was ready to fly its weight, c.g. position and inertia characteristics were measured. The moments of inertia about three axes through the c.g., parallel or perpendicular to the geometric datum planes of the model, were measured by suspending the model on two wires of equal length and swinging it as a bifilar pendulum about each axis in turn. Corrections were applied to account for the mass of the wire attachments. The upper ends of the wires were attached to a beam which could be held at any angle. The angle between the principal axis of inertia of the model and its horizontal datum plane was measured by finding the inclination of the beam, and thus of the model, at which the period of oscillation of the model in yaw was a maximum. The product of inertia was then calculated.

3.4 Experimental accuracy

The models were tracked from the ground by radar, synchronised kinetheodolites and a multi-station radio-Doppler system. Thus there were several ways in which histories of the position and velocity of every model could be obtained with considerable accuracy. The uncertainty in the velocity measurements arose almost entirely from the correction for wind velocity, and is about

±10 ft/sec. The local speed of sound was calculated from radio-sonde measurements of air temperature, and is accurate to within ±1 ft/sec. The resultant uncertainty in Mach number is therefore about ±0·01.

Most of the uncertainty in the experimental values of m_w and z_w is due to the uncertainty of measurement of the longitudinal short-period frequency. This was about ±2 per cent, and the resultant uncertainty in m_w is about ±4 per cent and in z_w about ±6 per cent. The damping of the short-period oscillation was measured to within ±10 per cent, and the resultant uncertainty in $(m_q + m_{\dot{w}})$ is about ±20 per cent.

The lateral derivatives that were evaluated from vector diagrams depend on the amplitude ratios and phase angles between the component oscillations of the Dutch roll. The ratio of the sideslip amplitude to that of $\dot{r}$ was determined to within about ±2 per cent and the corresponding phase angle to within about $\pm\frac{1}{2}$ degree. The remaining amplitude ratios were measured to within about ±5 per cent and the phase angles to within ±3 degrees. The resultant uncertainties in the derivatives are, approximately, ℓ_p ±12 per cent, ℓ_v ±6 per cent, n_r ±8 per cent and n_v ±4 per cent. The uncertainty in the values of y_v obtained analytically is about ±6 per cent, like that of z_w.

In general the linear normal and lateral accelerometers were offset from the roll axes of the models by distances of the order of an inch (Table 4). As a result they recorded linear accelerations induced by the oscillations in roll as well as by those in pitch and yaw. The accelerations due to the rolling motion were generally less than 0·1g, and since this is smaller than the uncertainty of measurement of most of the accelerometers the flight measurements were not corrected for this effect.

Three of the models carried a longitudinal accelerometer with a range of 5g and an uncertainty of measurement of 0·05g. At Mach numbers near 1·4 the retardation of the models was about 2·5g and the uncertainty of measurement was thus about ±2 per cent. At Mach numbers near 0·8 the deceleration was about 0·5g, so the uncertainty of measurement was about ±10 per cent. The drag of the models without longitudinal accelerometers was obtained by differentiation of the radio-Doppler velocity measurements with generally similar uncertainties. At transonic speeds, where the rate of change of drag was the greatest, the radio-Doppler measurements were probably slightly inferior to the accelerometer measurements.

In calculating the uncertainties[12] in the results presented in this report it has been assumed that errors which occurred in the flight measurements were independent of each other. It should be emphasised that these are the maximum uncertainties associated with individual numerical values. The errors in the curves drawn through all the data are likely to be much smaller.

4 FLIGHT BEHAVIOUR

4.1 Autorotation

Before the tests began the responses of a model to pulse-rocket disturbances were calculated with the aid of an analogue computer, using aerodynamic data for $M = 1{\cdot}6$. It was found that when the model c.g. was within the range of aircraft c.g. positions a single lateral pulse rocket could initiate a stable autorotation. The risk appeared to be eliminated by moving the c.g. forward, and accordingly all the models were ballasted to bring their c.g. positions close to the mean quarter-chord point.

The first three models were launched at Mach numbers near 1·5. Model 1 rolled rapidly after a lateral disturbance, but it recovered and flew on normally. Since the wing of the first model had a surface formed by a number of flat faces, the rapid rolling was attributed to an asymmetric flow separation from one of the ridge lines. This judgment seemed to be vindicated when the second and third models, which had the correct wing sections, did not autorotate. However, model 4 was launched at $M = 1{\cdot}8$, and the disturbance which it received when it shed its booster rocket started an autorotation which persisted for the rest of the flight. This suggested that the behaviour of the first model had been due to cross-coupling effects and not to a local flow separation. Further calculations, of the effects of combined lateral and longitudinal disturbances, showed that the autorotation of both models was accountable in terms of their known aerodynamic and inertial characteristics. Moreover it became clear that if booster-rocket separation had not caused model 4 to autorotate a single lateral pulse rocket at $M = 1{\cdot}7$ would have done so. Therefore attempts to measure lateral stability at the higher Mach numbers were abandoned and the four remaining models were all flown at Mach numbers below 1.5.

In order to reduce still further the risk that these models would autorotate, the magnitudes of the pulse-rocket yawing moments were held below the least values calculated to cause autorotation. In spite of this two of the last four models autorotated (Nos.6 and 7) but only at subsonic speeds. A full account of the calculations is given in the Appendix.

The initial development of the autorotation was extremely rapid, with angular accelerations in roll up to 5000 deg/sec^2. At the same time the angle of incidence increased to 10 degrees or more, and there were corresponding increases in the normal acceleration and the drag. The high drag caused the speed to fall very rapidly: for example, model 4 decelerated from M = 1·8 to M = 0·8 in 3 seconds. The first model in the series was the only one to recover from autorotation, but it did not accurately represent the aircraft and its rates of rotation differed from those of the other models. Three of the fully-representative models autorotated, at rates that were at least an order of magnitude higher than that of the intended barrel roll and were roughly proportional to Mach number. Some of the characteristics of their motion are discussed in section 6.3.

4.2 General behaviour

Because the models were all forced to roll continuously, their flight paths approximated to ballistic trajectories (Fig.5). Models 4, 6 and 7 fell short of the rest because they lost speed very rapidly when they autorotated. A typical Mach number history for one model is shown in Fig.6, and the variation of Reynolds number with Mach number for all the models is shown in Fig.7.

When they were not autorotating, all the models rolled slowly in the intended direction (Fig.8). Apparent differences between the rolling effectiveness of the control surfaces on the individual models are accountable in terms of the small amounts of twist, within the prescribed tolerances, which occurred in the wing and tail surfaces during manufacture. The roll behaviour of model 5 differed somewhat from that of the other models, and its rate of roll changed sharply at about M = 0·97.

In spite of their forward c.g. positions all the models experienced a pronounced transonic change of longitudinal trim. This was severe enough to excite a short-period oscillation (Fig.38) or to modify the motion if the model was already oscillating (Fig.39).

It proved very difficult to excite a pure longitudinal oscillation. The pulse rockets were all offset from the model centre lines and even when they were fired downward in symmetrical pairs they usually produced both a longitudinal and a lateral disturbance, probably because they failed to synchronise perfectly. Fortunately the amplitudes of the lateral oscillations excited in this way were usually not large enough to affect the longitudinal motion significantly through cross-coupling.

Evidence of cross-coupling appeared in the records of the motion excited by booster separation and by the lateral disturbances. The Dutch roll that followed a lateral disturbance was always accompanied by a longitudinal oscillation, which diverged at first as energy was fed into it from the lateral motion (Figs.4 and 39). Sometimes the waveform of the roll oscillation was distorted, but usually this was significant only at the largest amplitudes (Fig.4). The longitudinal oscillations were more strongly damped than the Dutch roll. This enabled the lateral oscillations to be analysed when the contribution to them from the longitudinal motion, through cross-coupling, had become negligible.

5 METHODS OF ANALYSIS

5.1 The equations of motion

For the purpose of analysis every flight was divided into a sequence of convenient time intervals during each of which the aerodynamic derivatives, and thus the Mach number, were assumed to be constant. Usually the intervals between the firing of successive groups of pulse rockets were appropriate but at transonic speeds, where some of the derivatives changed rapidly with Mach number, shorter intervals had to be used.

The assumption of a constant Mach number allowed the motion to be regarded as having only five degrees of freedom. This motion is described, relative to body axes, by the classical equations of aircraft motion which are set out in the Appendix. The equations have been simplified by neglecting the very small aerodynamic derivatives; these include all second derivatives and all acceleration derivatives except $m_{\dot{w}}$. For flight simulation on the analogue computer the ℓ_{vw} cross-coupling term and all the inertia cross-coupling terms were retained, but they were not taken into account in the analysis of the flight records. The longitudinal analysis[5] was based on the assumption of a pure longitudinal motion, and thus specifically excluded cross-coupling effects. The lateral motion was analysed by means of vector diagrams[6,7], which can represent a damped oscillation only when all components of the motion have the same frequency and damping factor. Therefore the cross-coupling terms could not be handled and were, necessarily, assumed to be zero. Most of them were in fact extremely small and their omission from the analysis is unimportant. Omission of the aerodynamic terms in ℓ_{vw} and n_{vw} may have introduced small errors, and these are discussed in section 5.3.

5.2 Longitudinal motion

The longitudinal short-period oscillation was analysed by using the method evolved by Voepel specifically to suit the requirements of free-flight model experiments. The analysis is set out in full in Ref.5, and leads to the following expressions for the derivatives and the manoeuvre margin:

$$m_w \simeq -\frac{i_B}{\mu_1}(\omega_{n1}\hat{t})^2 \tag{1}$$

$$z_w \simeq -\frac{\hat{t}}{V}\omega_{n1}^2 D_1 \tag{2}$$

$$(m_q + m_{\dot{w}}) \simeq -i_B(z_w + 2\hat{t}\lambda_1) \tag{3}$$

$$H_m \simeq \frac{m_w}{z_w} \simeq \frac{i_B \bar{c}}{D_1} \quad . \tag{4}$$

All the necessary information was obtained from the records of normal acceleration. When longitudinal and lateral oscillations occurred simultaneously it was sometimes necessary to begin the analysis at the second or third cycle, after both oscillations had damped sufficiently to make cross-coupling insignificant.

Additional values of z_w were obtained by plotting C_L against α.

5.3 Lateral motion

The principal method of evaluating the lateral derivatives was to solve the equations of motion graphically by constructing vector diagrams[6,7]. Supplementary values of n_v and some values of y_v were calculated by methods analogous to those used to obtain m_w and z_w from the longitudinal motion.

The telemetered data provided histories of the angular acceleration in roll $\dot{p}$, the lateral accelerations at the nose, c.g. and tail, and the differential pressures induced by sideslip on the probes fixed in the noses of the models. The flight records were analysed to determine the frequency and damping of the Dutch roll, and the amplitude ratios and phase relationships between the component oscillations in sideslip, roll and yaw. The $\dot{r}$ vector was chosen arbitrarily as the reference to which all amplitude ratios and phase angles were related.

The characteristics of the motion in yaw and in sideslip were determined from the lateral acceleration measurements. Although sideslip measurements were provided by the probes in the model noses, the amplitude and phase angle of the sideslip oscillation were obtained with greater accuracy from a vector solution of the kinematic equation

$$a_y = \frac{V}{g}(\dot{\beta} + r) \quad . \tag{5}$$

The roll and yaw equations each contained three unknown derivatives, and these had to be reduced to two before vector solutions could be obtained. Therefore estimated values of the derivatives that contributed least to the Dutch roll, namely ℓ_r and n_p, were used. The vector diagrams (Fig.27) then yielded values of ℓ_p, ℓ_v, n_r and n_v.

The terms coupling the lateral and longitudinal motions can be represented by vectors that rotate with respect to those representing the uncoupled motion. A qualitative indication of the relative importance of these coupling terms, and of the errors introduced by leaving them out of the analysis, is obtained by superimposing the circles swept out by the coupling vectors on the diagrams of the uncoupled motion. The relative magnitudes of the coupling terms, and thus the sizes of the circles, change continuously as the oscillations damp out. Two of the largest coupling terms, calculated from values of the coupling derivatives obtained from wind-tunnel tests, are represented in this way in Fig.27. They are shown at an instant approximately half-way between two successive disturbances, when the longitudinal oscillation had damped to about 15 per cent of its initial amplitude and the lateral oscillation to about 60 per cent. Although these coupling terms are not insignificant it is clear that their omission from the analysis has not introduced gross errors into the results.

The side-force derivative y_v was evaluated in two ways, by plotting C_y against β and by means of the expression

$$y_v = -\frac{\hat{t}}{V}\,\omega_{n2}^2\,D_2 \quad . \tag{6}$$

This is analogous to equation (2) and was derived[8] in a similar way, taking account of the freedom in roll.

Some additional values of n_v were obtained by means of an expression derived by Thomas and Neumark[9]:

$$n_v = \frac{i_C}{\mu_2}(\omega_{n2}\,\hat{t})^2 - \frac{i_E}{i_A}\ell_v \quad . \tag{7}$$

All the necessary experimental data were obtained from the records of lateral acceleration; the ℓ_v term was small compared to the frequency term and was obtained accurately enough by using estimated values of ℓ_v. The values of n_v given by equation (7) agree closely with those obtained from the vector diagrams, because both methods derive from the same equation and both take some account of the freedom in roll. In practice, different errors and uncertainties were introduced because the experimental data were manipulated in different ways in the two techniques, and the results were affected slightly by the values chosen for n_p in the vector diagram and for ℓ_v in equation (7). Nevertheless equation (7) enabled n_v to be calculated when there were not enough data available to construct a vector diagram, or when the record of roll acceleration was of poor quality.

The experimental results were not significantly affected by the steady rolling motion that was imposed on every model for the sake of safety. Its contribution to inertia cross-coupling was negligibly small and its associated sideslip angle, induced through the derivative n_p, was too small to be detected in the flight records.

5.4 Adjustments for different c.g. positions

The values of m_w and n_v in this report have been adjusted to relate to a common axis position at 0·262 $\bar{c}$. This is the c.g. position of model 8, which provided the most reliable data. The adjusted values were obtained from the original measurements by means of the relationships

$$m_{w_A} = m_{w_M} - \frac{\Delta x}{\bar{c}} z_w \tag{8}$$

$$n_{v_A} = n_{v_M} + \frac{\Delta x}{s} y_v \quad . \tag{9}$$

The values of z_w and y_v for these expressions were read from the smooth curves in Figs.15 and 32.

The measurements of the damping derivatives $(m_q + m_{\dot{w}})$ and n_r have not been adjusted, and each value relates to the c.g. position of the model from which it was obtained.

6 DISCUSSION OF RESULTS

In Figs.15 to 32 the free-flight measurements are compared with corresponding data from other sources, suitably adjusted to a c.g. position at $0{\cdot}262\ \bar{c}$. The static derivatives are compared with wind-tunnel measurements[1] obtained from a model with faired intakes. The dynamic derivatives are compared with estimates[10], which were calculated by theoretical methods but incorporated as much information as possible from the wind-tunnel tests. Inevitably some judgment was used in combining theories appropriate to different ranges of Mach number.

6.1 Longitudinal stability

Many of the longitudinal oscillations were accompanied by lateral oscillations. This seldom affected the short-period frequency but the transfer of energy between the two modes often had a significant effect on the longitudinal damping. All measurements affected by cross-coupling have been rejected, and thus there are fewer points on the damping curve (Fig.13) than on the frequency curve (Fig.12). Where reliable damping measurements were not available the reduced frequency (Fig.14) was calculated from the damped frequency measurements only, with very little loss of accuracy because the frequencies were so high.

The two methods used to evaluate z_w have produced results that support each other very well (Fig.15). They define the curve clearly at subsonic and supersonic speeds, although at transonic speeds they are rather scattered. At Mach numbers around 0·9 the measurements appear to lie on two distinct curves, but this may be fortuitous. Only one curve has been drawn through the data; its ordinates were calculated from those of the m_w and H_m curves, which are comparatively well defined at transonic speeds (Figs.16 and 18). The transonic loss of z_w, indicated by the majority of the free-flight measurements, does not appear in the wind-tunnel measurements and there is insufficient evidence to show its cause.

The m_w curve (Fig.16) reflects the shape of the frequency curves, because m_w is related to the square of the reduced frequency. At Mach numbers between 0·8 and 0·9 the measurements from model 2 lie consistently above those from model 8 and thus confirm, at least at low lift coefficients, that m_w is a function of C_L at transonic speeds.

Measurements of rotary damping in pitch $(m_q + m_{\dot{w}})$ are confined to Mach numbers below 1·3 (Fig.17). At low supersonic speeds they confirm the estimate[10], but at subsonic speeds they indicate a constant level of rotary damping generally slightly greater than the estimate.

6.2 Lateral stability

The amplitudes of some of the Dutch roll oscillations, especially those of model 2, were very small (Fig.19). While their frequency could be measured satisfactorily it was sometimes impossible to measure the damping. Thus there are fewer experimental points on the damping curve (Fig.21) than on the frequency curves (Figs.20 and 22).

There is a pronounced trough in the frequency curves at high subsonic speeds, with a minimum value at about $M = 0{\cdot}96$. Between this Mach number and $M = 1{\cdot}25$ the measurements from models 2, 6 and 8 lie on three quite separate curves, which differ by amounts that are too great to be caused by the differences between the model inertias and c.g. positions.

The amplitude ratios and phase relationships between the oscillations in sideslip, roll and yaw are plotted in Figs.23 and 24. The vector diagrams were drawn from the actual experimental data, not from the smoothed curves.

The experimental values of ℓ_p and n_r (Figs.28 and 30) confirm the estimates[10] at subsonic speeds, but at supersonic speeds both derivatives are larger than the estimates.

The experimental curves of the three sideslip derivatives have several features in common (Figs.29, 31 and 32). They all show a marked change in level at transonic speeds, and at supersonic speeds they tend to fall as the Mach number increases. At transonic speeds there is a more or less severe trough in all the curves, with a minimum value at about $M = 0{\cdot}96$. These variations in the sideslip derivatives are probably associated with variations in fin effectiveness, but it is impossible to deduce from the free-flight measurements what the cause of the troughs may be. The corresponding troughs in the wind-tunnel curves are much smaller.

The n_v curves (Fig.31) reflect the pattern of the frequency curves, and at Mach numbers between 0·9 and 1·25 the results from three models lie on widely separated lines which indicate a progressive loss of n_v with increasing lift coefficient. The relationship between C_L and n_v is not linear. These measurements show that, within the range of lift coefficients covered by the free-flight tests, n_v is extremely sensitive to C_L at transonic speeds.

6.3 Autorotation

Three of the fully-representative models autorotated (models 4, 6 and 7). Their weights, moments of inertia and tailplane settings differed slightly from each other, but the characteristics of their autorotation were surprisingly consistent.

The mean rate of roll was roughly proportional to Mach number and was of the order of 1000 degrees/sec (Fig.34). When pulse rockets were fired they excited oscillations that were superimposed on the rolling motion. Sometimes the pulse rockets checked the autorotation momentarily, by reducing the rate of roll and the angle of incidence, but the models always reverted to autorotation (Figs.33(b) and 36). The oscillations in roll, pitch and yaw that were excited by the pulse rockets were all coupled together, at a frequency slightly less than double the mean rate of roll (Fig.35).

Normal-force and side-force coefficients during autorotation are plotted in Figs.36 and 37. The highest levels are associated with the fully-developed autorotation; the troughs in the curves show the temporary effects of pulse-rocket disturbances.

The analogue computations predicted the mean rates of roll adequately (Fig.34) but they indicated frequencies of oscillation about the mean rates that were roughly half those measured in flight. Analytical treatment of the equations that were set up on the computer, with some simplifying assumptions, showed that in fact two frequencies are possible at any Mach number. The higher one corresponds to the actual frequency measured in flight and the lower one to the analogue solution (Fig.35). The factors that determine which frequency occurs in a particular situation were not investigated. The roll oscillations that occurred in flight were damped (Fig.33) whereas those indicated by the computer were undamped or divergent (for example, Fig.51(a)). This difference probably occurred because the equations were linearised and related to a constant flight velocity, whereas the actual motion was non-linear and the flight speed was falling rapidly.

The dynamic behaviour of the aircraft cannot be inferred from the model behaviour because they were not dynamically similar. Therefore, following the autorotation incidents on the models, the roll behaviour of the full-scale aircraft was re-examined throughout the flight envelope, using an analogue computer. The same equations were used for the aircraft as for the models, with the latest aerodynamic data. These calculations indicated that the aircraft would not get into an autorotational motion from any likely flight condition. This result should be reliable, because the onset of model autorotation and the resultant rates of roll were predicted correctly by the same procedure.

6.4 Effects of simulated engine failure

The sudden failure of one engine in flight was simulated in model 7 by partially blocking the starboard duct at M = 1·295 (see section 3.1). The blocking device remained in position for the rest of the flight and thus permitted measurement of some of the effects of flying with one engine out.

When the duct was blocked the model was still oscillating slightly after separating from its booster rocket. The only immediate effects of the sudden blockage were an extremely small change in the lateral trim and a barely detectable increase in the amplitude of the lateral oscillation (Fig.39). There was no longitudinal disturbance or change of trim. At Mach numbers below 1·295 the longitudinal stability remained the same as that of the symmetrical models (Figs.40, 41, 42 and 43) but the lateral stability was significantly worse. Although the damping of the Dutch roll was not affected (Fig.44) the transonic losses of n_v and y_v were more severe and were spread over a wider range of Mach numbers (Figs.45 and 46). Unfortunately none of the other lateral derivatives could be evaluated because of the failure of the angular accelerometer used for the roll measurements.

Spillage from the intake would have increased as soon as the duct was blocked, and would have become progressively greater as the Mach number decreased. This would have affected the flow over the rear body, particularly if the spillage air separated from the sharp lip of the intake, and could have brought about a loss of fin effectiveness. Only flow changes affecting the fin could have caused simultaneous changes in y_v and n_v of the kind measured here. There is nothing to show why these effects were confined to Mach numbers between 0·8 and 1·25 or why the tailplane, and thus the longitudinal stability, was not similarly affected. It must be remembered that the intake geometry was fixed in these tests. The effects of an actual engine failure might be alleviated by altering the intake geometry, but the complex nature of the intake flow[11] makes this impossible to predict. It seems likely that the adverse effect of spillage on the lateral stability will be greater at higher angles of incidence, because then more air will spill over the top of the intakes to affect the fin.

6.5 Duct flow and drag

The only measurements that were made in the ducts were the static pressures at the maximum cross-sections and at the ends of the tailpipes. The ratio between these two pressures served to indicate whether the tailpipe had choked at supersonic speeds. Measurements were made in both ducts in the first five models but only in one duct in the other three.

The measurements established that the tailpipes were invariably choked at supersonic speeds, but they also showed that there were considerable differences between the pressure ratios in the individual ducts (Fig.47). These were far too large to have been caused by the small differences in duct geometry allowed by the dimensional tolerances, and they suggest that there were major differences between the internal flow patterns. These could have originated at the intakes. The forebody boundary layers were not diverted, and in passing through the intake shocks they may have thickened or separated in different ways. From so little information it is impossible to determine, even roughly, how the internal drag may have been affected.

The curves of total drag for six models are plotted together in Fig.48. All the models trimmed at different lift coefficients and the drag measurements therefore include different amounts of drag due to lift and trim drag. They also include unknown contributions from the internal drag of the ducts, and in any case they are subject to some uncertainty of measurement (see section 3.4). In view of the uncertain quality of the drag measurements a drag breakdown has not been attempted.

7 CONCLUSIONS

In general the longitudinal stability measurements support the tunnel measurements and the estimates, but there is an unexpected drop in z_w and m_w at transonic speeds. At supersonic speeds the estimated fall in rotary damping $(m_q + m_{\dot{w}})$ with increasing Mach number is confirmed.

There are several notable differences between the lateral stability measurements and the corresponding estimates and tunnel measurements. At subsonic speeds ℓ_v and y_v are significantly lower than the tunnel measurements, and at supersonic speeds ℓ_p and n_r are considerably higher than the estimates. The three sideslip derivatives ℓ_v, n_v and y_v have several features in common, of which the most important are a pronounced drop at transonic speeds and a steady fall with increasing Mach number at supersonic speeds. Both these effects are consistent with losses of fin effectiveness. At transonic speeds and low lift coefficients the n_v measurements show a remarkable sensitivity to C_L.

The transient effects of a simulated engine failure at M = 1·295 were negligible. With one engine duct partially blocked the longitudinal stability remained unaffected, but the transonic loss of lateral stability became more severe and was spread over a wider range of Mach numbers. These effects must be associated with the increased spillage from the intake, and are likely to become worse at higher angles of incidence.

Some of the models autorotated after lateral disturbances, and their behaviour was investigated by means of an analogue computer. The accuracy with which the computer forecast model behaviour indicates that the conditions causing autorotation of the full-scale aircraft can be reliably determined in the same way. Since aircraft with most of their mass distributed lengthwise are particularly prone to autorotation, future free-flight tests of such configurations should always be preceded by a thorough investigation of their dynamic behaviour.

Appendix

ANALOGUE COMPUTATION OF THE EFFECTS OF CROSS-COUPLING ON THE RESPONSE OF THE MODELS

by

A. Jean Ross, Ph.D.

A.1 Introduction

As described in this Report, the experimental technique was to disturb the free-flying model from its equilibrium flight path by a series of pulse rockets fired at intervals, so that the stability derivatives could be obtained by analysis of the resulting response. The first analogue computation was done before the flight tests began in order to determine·

(i) whether the proposed pulse rockets were of sufficient thrust, and suitable duration, to give disturbances of sufficient magnitude for accurate measurement,

(ii) the time required between the firing of successive pulse rockets to allow the oscillations to decay, and

(iii) the effects of any cross-coupling of the longitudinal and lateral modes.

Since the models had the majority of their mass distributed along the fuselage, and therefore small inertia in roll, their behaviour in roll could be expected to be lively. In fact, it was found that the rate of roll could, under some flight test conditions, become large enough to cause the model to autorotate, and the cross-coupling problem became the primary one. A fourth objective of the computations was added during the course of the flight tests, to determine the maximum disturbance, due to separation from the booster rocket or due to the pulse rockets, for which the model would not autorotate, so that the remaining experiments could be planned to avoid autorotation.

A.2 Equations of motion, and data used in the analogue computation

It was assumed that the variation in forward speed following a disturbance would be small for the first few seconds, so that the equations of motion appropriate to five degrees of freedom (v, w, p, q, r) were used. The inertia cross-coupling terms were all retained (including the product-of-inertia terms, since wind-body axes were used) and the aerodynamic cross-coupling arising from the rolling and yawing moments due to combined incidence and sideslip were also considered. For horizontal flight, at very small lift, the equations of motion become:-

$$y_v \frac{v}{V} + y_B = \frac{m}{\rho S V}\left\{\frac{\dot{v}}{V} - p\frac{w}{V} + r\right\} \tag{A1}$$

$$z_w \frac{w}{V} + z_B = \frac{m}{\rho S V}\left\{\frac{\dot{w}}{V} - q + p\frac{v}{V}\right\} \tag{A2}$$

$$\ell_v \frac{v}{V} + \ell_p \frac{ps}{V} + \ell_r \frac{rs}{V} + \ell_{vw}\frac{v}{V}\,\frac{w}{V} + \ell_\xi \xi + \ell_B = \frac{1}{\rho S V^2 s}\{A\dot{p} - (B - C)\,qr - E(pq + \dot{r})\} \tag{A3}$$

$$m_w \frac{w}{V} + m_{\dot{w}} \frac{\dot{w}\bar{c}}{V^2} + m_q \frac{q\bar{c}}{V} + m_B = \frac{1}{\rho S V^2 \bar{c}}\{B\dot{q} - (C - A)\,rp + E(p^2 - r^2)\} \tag{A4}$$

$$n_v \frac{v}{V} + n_p \frac{ps}{V} + n_r \frac{rs}{V} + n_{vw}\frac{v}{V}\,\frac{w}{V} + n_B = \frac{1}{\rho S V^2 s}\{C\dot{r} - (A - B)\,pq + E(qr - \dot{p})\} \tag{A5}$$

where the notation is that of the Royal Aeronautical Society Data Sheets, with $\ell_2 = \bar{c}$ for the longitudinal stability group. The dot represents differentiation with respect to true time, and the disturbance is represented by the "coefficients" y_B, z_B etc. The equations have to be rewritten for use on an analogue computer, and a short-hand notation was introduced for the quotient of the dimensional derivative and the mass (or moment of inertia), e.g.

$$Y'_v = -y_v \cdot \frac{\rho S V}{m}$$

$$L'_v = -\ell_v \cdot \frac{\rho S V^2 s}{A}$$

where a minus sign is introduced, if necessary, to make all such quotients positive. The full list is given in the list of symbols, which also gives the definitions of the various inertia ratios, following the suggestions of Ref.13. For convenience, we also write α and β in place of $\frac{w}{V}$ and $\frac{v}{V}$ respectively. In the required form we have,

$$\dot{\alpha} = -Z'_w\alpha + q - p\beta + Z'_B \qquad (A6)$$

$$\dot{\beta} = -Y'_v\beta + p\alpha - r + Y'_B \qquad (A7)$$

$$\dot{p} = -L'_v\beta - L'_p p + L'_r r - L'_{vw}\alpha\beta - L'_\xi \xi_0 - b_x qr + e'_x(pq + \dot{r}) + L'_B \qquad (A8)$$

$$\dot{q} = -M'_w\alpha - M'_{\dot{w}}\dot{\alpha} - M'_q q + b'_y pr - e'_y(p^2 - r^2) + M'_B \qquad (A9)$$

$$\dot{r} = N'_v\beta - N'_p p - N'_r r - N'_{vw}\alpha\beta - b_z pq - e'_z(qr - \dot{p}) + N'_B \qquad (A10)$$

The rolling moment due to aileron, $L'_\xi \xi_0$, is included to represent the asymmetric aileron setting necessary on the free-flight models for flight path control.

Equations of similar form have been studied analytically, after some simplifying assumptions have been made, e.g. in Refs.14,15 and 16. When the disturbances are small, the product terms may be neglected, so that the equations separate into the two familiar groups, equations (A6) and (A9) giving the longitudinal short-period oscillation, and equations (A7), (A8) and (A10) giving the lateral modes, usually two subsidences and the Dutch-roll oscillation. Next, if a constant rate of roll, p_0 say, is imposed on the system, then with w, v, q and r assumed to be small, equation (A8) determines the now variable aileron input, and the remaining four equations may again be linearised; for moderate roll rates, the character of the response is similar to that for $p_0 = 0$, with two distinct oscillations corresponding to the longitudinal short-period and the Dutch roll, but with frequencies and dampings dependent on p_0. However, if p_0 is greater than the lower of the natural frequencies of the two uncoupled oscillations, (the "critical" roll rate), then the motion becomes divergent. These different types of response also arise when the rate of roll is variable, and attains large magnitudes so that the equations can no longer be linearised. The longitudinal and lateral oscillations are no longer sinusoidal, and if p increases beyond the critical roll rate, the response will diverge from oscillations about zero to oscillations about the non-zero steady state values, i.e. autorotation.

The first analogue computations were based on estimates and wind-tunnel measurements of the derivatives, summarised in Ref.17, and calculated model inertias. The estimated change of yawing moment due to sideslip with incidence was small at low incidences, and so n_{vw} was taken to be zero. As revised values of some of the derivatives became available from the free-flight tests, and the inertias could be measured on the completed models, the new information was incorporated into the later computations. However, the changes made were not significant as regards the character of the response, and the values used for the results shown in the figures are given in Table 5. A constant height of 5000 ft was assumed.

Various checks were made to ensure accuracy of the responses. The frequencies and dampings of the uncoupled longitudinal and lateral oscillations were calculated for each case considered, and were compared with those obtained from analysis of the computer results for the cases in which the oscillations separated, as in Fig.49(b). For the responses which were oscillations about a non-zero steady state, it was possible to compare with the approximate steady state values (as derived in section 3 below), and also to reduce the magnitude of the input until the oscillations separated, and then check these responses. The frequency and damping of the longitudinal and lateral modes, the approximate steady state values, and the approximate frequency of the coupled oscillation, for the examples shown in the figures, are given in Table 6. A comparison was also made with results from a digital computer for one example, and although there were slight differences in magnitude and phasing of the coupled motion, the agreement was thought to be satisfactory; the differences were probably due to small errors in the potentiometer calibrations on the analogue computer.

A.3 Analytic approximations

The frequencies and dampings of the uncoupled longitudinal and lateral modes were obtained "exactly" from the linear simultaneous differential equations[9]. Some of the properties of the coupled motion were also derived by making approximations to the coupled equations, as follows.

A.3.1 Steady states

Since the simultaneous equations obtained by putting the accelerations and applied forces and moments to zero in equations (A6) to (A10) are non-linear, it is possible that non-zero solutions exist. This was demonstrated by Pinsker[15], who derived an approximation for the steady rate of autorotation, neglecting all the damping terms except z_w, m_q and ℓ_p. Thomas and Price[16] retained all the usual derivatives in their analysis, which was for equations referred to principal inertia axes, and the corresponding calculation for the present equations referred to wind-body axes is given below.

The non-linear simultaneous equations to be solved may be written in the form

$$Z'_w \alpha_s + p_s \beta_s = q_s \tag{A11}$$

$$p_s \alpha_s - Y'_v \beta_s = r_s \tag{A12}$$

$$L'_v \beta_s + L'_p p_s - L'_r r_s - e'_x p_s q_s = - L'_{vw} \alpha_s \beta_s + b_x q_s r_s \tag{A13}$$

$$M'_w \alpha_s + M'_q q_s - b'_y p_s r_s + e'_y p_s^2 = e'_y r_s^2 \tag{A14}$$

$$N'_v \beta_s - N'_p p_s - N'_r r_s - b_z p_s q_s = e'_z q_s r_s + N'_{vw} \alpha_s \beta_s . \tag{A15}$$

For a first approximate solution, the terms written on the R.H.S. of equations (A13) to (A15) were neglected, so that q_s and r_s may be substituted from equations (A11) and (A12). The condition that the three resulting equations should be compatible, when considered as linear simultaneous equations in α_s and β_s, leads to the solution $p_s = 0$ or to the biquadratic,

$$\begin{aligned} & p_s^4 [b'_y (b_z L'_p + e'_x N'_p) - e'_y (b_z L'_r - e'_x N'_r)] \\ & - p_s^2 [(M'_w - b'_y Y'_v Z'_w)(b_z L'_p + e'_x N'_p) + b'_y (N'_v L'_p + L'_v N'_p) \\ & + e'_y (L'_v N'_r - N'_v L'_r) - M'_q (L'_p N'_r + N'_p L'_r) \\ & + e'_y Z'_w \{b_z L'_v - e'_x N'_v + Y'_v (b_z L'_r - e'_x N'_r)\}] \\ & + (M'_w + M'_q Z'_w) \{L'_p N'_v + N'_p L'_v + Y'_v (L'_p N'_r + N'_p L'_r)\} = 0 . \end{aligned} \tag{A18}$$

It has been shown[15] that motion about the smaller critical roll rate, p_{crit}, is unstable, and diverges to the larger rate, p_s. The corresponding steady values of α_s, β_s, q_s, r_s, may then be obtained. An attempt was made to derive a new value of p_s from equation (A14) by numerical iteration, but the process was found to be divergent when the terms on the R.H.S. of equations (A13) to (A15) were also included. However, the approximations are sufficiently accurate to use as a check on the analogue computer results, and to give a guide to the critical rate of roll. For the models under consideration, the roots of equation (A18) are very close to Phillips' approximation[14] for the imposed constant roll rates, $\sqrt{N'_v}$ and $\sqrt{M'_w}$, which define the stability boundaries of the motion, (see Table 6).

A.3.2 Frequency of coupled oscillations

The equations of motion for small perturbations about the non-zero steady states are obtained by writing $\alpha = \alpha_s + \alpha'$, $\beta = \beta_s + \beta'$ etc. in equations (A6) to (A10), and may be linearised by neglecting second-order terms in the perturbations α', β' etc. In his treatment, Phillips[14] obtained the frequencies for the constrained motion, $p = p_o = \text{const}$, $\alpha_s = \beta_s = q_s = r_s = 0$, and neglecting damping terms, obtained the stability quartic

$$D^4 + D^2\left[M'_w + N'_v + p_o^2(1 + b'_y\,b_z)\right] + \left(M'_w - b'_y\,p_o^2\right)\left(N'_v - b_z\,p_o^2\right) .$$

At the steady state, $p_o = p_s \approx \sqrt{M'_w/b'_y}$, and so only one non-zero frequency results,

$$\omega = \left[M'_w\left(1 + b_z + \frac{1}{b'_y}\right) + N'_v\right]^{\frac{1}{2}} . \tag{A19}$$

For the autorotational state, (i.e. the roll rate is no longer controlled) the stability polynomial is a quintic,

$$\begin{aligned} D\Big\{D^4 + D^2\Big[M'_w + N'_v + \alpha_s(L'_v + \alpha_s\,L'_{vw}) + \left(1 + b'_y\,b_z + \alpha_s^2\,b_x\,b'_y\right)p_s^2\Big] \\ + M'_w\left[N'_v + \alpha_s(L'_v + \alpha_s\,L'_{vw})\right] + M'_w\,p_s^2(b_x\,\alpha_s^2 - b_z) + N'_v\,p_s^2\left(2b_x\,b'_y\,\alpha_s^2 - b'_y\right) \\ + \alpha_s(L'_v + \alpha_s\,L'_{vw})\,b'_y(1 + b_z)\,p_s^2 + p_s^4\left(b'_y\,b_z + \alpha_s^2\,b_x\,b'_y\right)\Big\} \end{aligned} \tag{A20}$$

where again the damping terms have been neglected, but the aerodynamic coupling term, L'_{vw}, retained. The biquadratic factor has two non-zero roots, one being near Phillips' approximation[14], and the other remaining finite when the approximate steady state values of α_s and p_s are substituted. The numerical values are given in Table 6 for some of the flight conditions considered.

A.4 Response calculations

A.4.1 Response to applied lateral disturbance

It had been hoped that the free-flight tests would extend to a maximum Mach number of about 1·8, but it was found that, with the model weight and inertias, and the aircraft c.g. position, the Dutch-roll oscillation was divergent, and so the first analogue computations were for $M = 1{\cdot}6$. The model was assumed to be ballasted to bring the c.g. to $0{\cdot}44\,\bar{c}$, i.e. the aft limit of the aircraft c.g. The response to a pulse rocket with a thrust of 140 lb wt, firing for 0·07 sec (represented by a square wave input) is shown in Fig.49(a), as angles of incidence and sideslip, and angular velocities. The applied yawing moment, N_B, corresponds to the maximum moment arm possible in the model, and a small rolling moment, L_B, due to the offset position of the pulse rockets, is also included. It is seen that the response is violent, and becomes an undamped oscillation about non-zero values of the linear and angular velocities. The critical roll rate, above which the motion diverges to the higher steady-state value, is of the order of 20 rad/sec, and the approximate steady-state values are in good agreement with the analogue computer results. The frequency of the coupled oscillation, 4·8 cycles/sec, corresponds to the lower frequency given by equation (A20) of 5·3 cycles/sec, rather than that given by equation (A19), or the larger root of equation (A20). When the applied yawing moment is halved, the critical roll rate is not attained, and the longitudinal and lateral modes separate (see Fig.49(b)). The periods and dampings are in satisfactory agreement with those calculated for the uncoupled oscillations, although it is difficult to measure the damping of the longitudinal mode accurately from the size of response obtained on the computer records.

Since a reduction in pulse rocket size was impracticable, it was decided to move the c.g. of the model to a position further forward. This change, together with the increased inertias measured on a model, led to satisfactory responses, although the resulting change in critical roll rate is negligible for the c.g. position finally chosen. However, with the decrease in the pulse-rocket yawing moment arm, and increase in yaw inertia, the initial rate of yaw is reduced, which leads to smaller angles of sideslip, and so to smaller rates of roll (from the $\mathcal{L}_v\beta$ term). The responses shown in Fig.50 are for the derivatives corresponding to those obtained from the free flight experiments. Analysis of the separated oscillations (i.e. to the right of the arbitrary dotted line in the $\dot{p}$ and $\dot{q}$ responses) again gives results in reasonable agreement with those for the modes considered independently of each other. On the basis of these results, and similar ones for $M = 1{\cdot}2$, it was decided to fly the models with their c.g. at about $0{\cdot}28\,\bar{c}$.

A.4.2 Response to applied longitudinal disturbance

The responses to pulse rockets fired to produce square wave inputs of lift and pitching moment, of duration 0·07 seconds, were obtained at $M = 1{\cdot}2$ and $M = 1{\cdot}6$, with the model rotating at a roll rate of 1·75 rad/sec (100°/sec). The cross-coupling terms have little effect, the roll rate remaining small, and so the analysis of the longitudinal response of the free-flight models could be expected to be straightforward.

A.4.3 Response to "separation" disturbance

The fourth free-flight model flown in the test series began to autorotate directly after it had separated from its booster rocket, and so a further investigation was made using the analogue computer, to see if the motion could be explained in terms of the aerodynamic and inertia characteristics of the model. The first three models had been launched at $M = 1{\cdot}5$, but the initial velocity of the fourth model was appreciably higher, which probably accounted for the difference in behaviour. However, the disturbances applied to the model at separation are completely random, (due to the complex flow about the rocket motor and slight misalignment of the mounting), so that a check was needed on the possible behaviour of future models. From previous experience, it was known that initial peak angles of incidence and sideslip immediately after separation could be of the order of ±3° to ±4°, and the response to disturbances of such magnitude was first investigated, for the particular case of model 4.

The magnitudes of the applied pitching and yawing moments M_D and N_D (square waves of 0·05 sec duration) were chosen so that the uncoupled responses in α and β gave initial peak values of about 4° (0·07 rad), see Fig.51(c). The responses were then recorded for all the combinations of signs of the simulated separation disturbances. The constant rolling moment due to the aileron setting was also included, to give a steady roll rate of 100°/sec (= 1·75 rad/sec). It was found that the motion became oscillatory about non-zero values of the angular and linear velocities if the separation disturbance caused initial positive α and positive β, whereas with α and β both negative, or of opposite sign, the disturbance damped out satisfactorily within about one second. Examples of each type of response are shown in Figs.51(a) and (b) for $M = 1{\cdot}7$. The critical roll rate is again about 20 rad/sec, and the approximations to the steady state values are shown in Fig.51(a), where the two sets of responses show the effect of the ℓ_{vw} term. With $\ell_{vw} = 0$, the oscillation about the steady state is divergent, and the approximations to the steady state values are good, but with $\ell_{vw} = -0{\cdot}4$, the final angle of incidence is reduced, and the responses, particularly that in $\dot{p}$, indicate the presence of an additional mode of relatively long period. Two other oscillatory modes are present in both sets of responses, but the one with the higher frequency damps out, so that it does not seem possible to analyse it. The frequency of the residual oscillation may be obtained from the response in $\dot{p}$ (or p), giving 6·3 cycles/sec with $\ell_{vw} = -0{\cdot}4$, and 5·9 cycles/sec with $\ell_{vw} = 0$. For the corresponding approximate values obtained from equation (A20), the value of a_s indicated by the analogue results was used from Fig.51(a), (since the approximation to a_s was derived neglecting L'_{vw}) to give the frequencies listed in Table 6*. The analogue results are again close to the lower of the pair of approximate values.

Having demonstrated that the autorotation due to disturbances at separation at M = 1·7 is predictable using the equations of motion given in equations (A6) to (A10), the calculations were repeated for separation at M = 1·4. The magnitudes of the applied pitching and yawing moments were varied, until a limiting condition was found. With zero pitching moment, the yawing moment was increased negatively until autorotation occurred, the limiting peak angle of sideslip being about 0·09 rad (≈ 5°). This is outside the range previously observed on free-flight models, and so the magnitude of the yawing moment was decreased so that $\beta_{max} = 4°$, and the limiting pitching moment was then found. For an initial peak angle of incidence of about 0·05 rad (≈ 3°), autorotation occurred if the aileron moment was put to zero, while the disturbance damped out normally with the applied constant roll rate of 1·75 rad/sec. Similar limits on a_{max} and β_{max} were obtained for the simulation of a model ballasted for the c.g. at the leading edge of the mean chord (0 $\bar{c}$). Doubling the inertia in roll was found to alleviate the problem, but this was impractical for the actual experiment. However, in the light of this information, the mounting of the model on its booster rocket was slightly altered, to ensure minimum separation disturbance.

A.4.4 Limiting pulse-rocket disturbance

A lateral pulse-rocket disturbance at M = 1·7, of proposed test magnitude, was also shown by the computer to cause autorotation, and so it was decided to restrict the remaining model tests to a maximum Mach number of 1·5.

---

*Although a_s is greatly reduced when ℓ_{vw} is included, it was found that the term $a_s\,(L'_v + a_s\,L'_{vw})$ arising in equation (A20), evaluated using the analogue value of a_s, is very close to $a_s\,L'_v$ evaluated with the approximate value of a_s, so that the change in frequency due to ℓ_{vw} is small.

It was then felt advisable to determine the limiting applied disturbance for satisfactory response at M = 1·4. The weight, c.g. position and moments of inertia of model 4 were retained, but revised values of some derivatives were used. The sign and magnitude of the yawing moment were varied, and some of the results are shown in Fig.52. The maximum positive yawing moment was found to be about 700 lb ft (see Fig.52(a)), and, as expected, the magnitude of the negative yawing moment which leads to near-critical roll rates is smaller. With zero rolling moment, the limit on N_B is about -480 lb ft (Fig.52(b)).

This data was used to decide on the firing sequence for the lateral pulse rockets in the remaining free-flight models. Those mounted on the port side ahead of the c.g. were fired first (positive yawing moment) and the starboard ones during the later subsonic phase of flight. In the event, the negative moments did cause autorotation on two of the models at subsonic speeds.

A.5 Comparison of computed and flight results

Since the estimates and wind-tunnel measurements of the derivatives are generally in fairly close agreement with those obtained from the free-flight tests, the frequencies and dampings of the uncoupled longitudinal and lateral oscillations as measured from the analogue computer results and in flight also agree well (c.f. Figs.4 and 50). Of more interest is the comparison of the autorotational characteristics. The variation of the mean roll rate has been obtained from the models which autorotated (Fig.34) and agrees well with the analogue results at M = 1·4 and 1·7. No analogue computations have been done for subsonic speeds, but the approximation for the steady roll rate, equation (A18), (which slightly overestimates the experimental and analogue results at supersonic speeds), gives $p_s = 720°/\text{sec}$ at M = 0·7, based on estimates of the derivatives[10]. Although a little below the experimental value, the approximation indicates a similar variation with Mach number to that obtained experimentally. The frequency of the coupled oscillation present in the experimental responses at subsonic speeds is close to that given by Phillips' approximation[14] at M = 0·7 (see Fig.35) and the ratio $p_s/\omega \approx$ const, indicated by equation (A19), is substantiated. (Equation (A20) gives frequencies of 3·9 and 0·9 at M = 0·7). It is not possible to derive the experimental frequencies at supersonic speeds, as Model 4 decelerated so rapidly, but it is interesting to note that the predominant mode in the analogue responses seems to be the one with the lower frequency, while the logical extrapolation of the experimental curve lies close to the higher frequency, see Fig.35. There is evidence of a higher frequency mode being present in the analogue responses, e.g. Fig.51, but it does not seem possible to analyse it.

Table 1

SCHEDULE OF TESTS

Model No.	Purpose	Date of flight	Flight behaviour	Mach No. range	Measurements obtained
1	To check the design of the models and the experimental techniques, and to obtain some approximate aerodynamic data.	2 Feb. 1962	At $M = 1{\cdot}3$ the first lateral disturbance set up autorotation which persisted down to $M = 0{\cdot}8$. The rest of the flight was satisfactory and all systems worked correctly.	1·56 to 0·60	Sufficient to show the design and instrumentation to be satisfactory. A few values of longitudinal and lateral stability derivatives were obtained.
2	To measure longitudinal stability derivatives near zero lift.	26 Mar. 1962	Entirely satisfactory. Some longitudinal disturbances excited small-amplitude lateral oscillations as well as longitudinal oscillations.	1·48 to 0·78	z_w, m_w and $(m_q + m_{\dot{w}})$ with, in addition n_v and y_v.
3	As model 2 but at lift coefficients near 0·1.	15 May 1962	The pulse-rocket system failed after firing only twice.	1·48 to 0·74	A few values of the longitudinal derivatives, and of n_v and y_v.
4	To measure the transient effects of a simulated engine failure in supersonic flight, and to measure the effects on the stability derivatives of flying with one engine cut, near zero lift.	23 July 1962	The model autorotated throughout its flight. All systems worked correctly.	1·80 to 0·33	Trim, roll rates and oscillation frequencies during autorotation.
5	As model 3.	29 Aug. 1962	The pulse-rocket system failed completely.	1·46 to 0·75	Drag, trim and duct pressures only.

Table 1 (Contd)

Model No.	Purpose	Date of flight	Flight behaviour	Mach No. range	Measurements obtained
6	To measure lateral stability derivatives at all speeds and longitudinal stability derivatives at high subsonic speeds, near zero lift.	5 Dec. 1962	Satisfactory until autorotation was set up by a lateral disturbance at M = 0·87. The autorotation persisted for the rest of the flight.	1·43 to 0·36	All the required measurements at Mach numbers down to 0·87. At lower Mach numbers, data on trim, roll rates and oscillation frequencies during autorotation.
7	As model 4.	26 Mar. 1963	The telemetry channel transmitting angular acceleration in roll failed $\frac{1}{2}$ second after the model left the ground. All other systems worked correctly. Autorotation was set up by a lateral disturbance at M = 0·8 and persisted for the rest of the flight.	1·49 to 0·53	Longitudinal derivatives at all Mach numbers down to 0·8. Only y_v and n_v could be obtained from the lateral motion.
8	To measure longitudinal stability derivatives at all speeds and lateral stability derivatives at transonic speeds, near zero lift.	5 Feb. 1964	An intermittent fault occurred in the data channel telemetering angular acceleration in roll. All other systems worked correctly and there was no autorotation.	1·47 to 0·74	All the required measurements. No data were lost or degraded by the intermittent fault in the telemetry equipment.

Table 2

MODEL WEIGHT AND INERTIA CHARACTERISTICS

Moments of inertia were measured about axes through the c.g., parallel and normal to the Horizontal Datum

Model number	1	2	3	4	5	6	7	8
Weight (lb)	200	201	202	205	209	210	202	213
c.g. position, as a fraction of $\bar{c}$	0·257	0·264	0·260	0·264	0·247	0·259	0·262	0·262
Moment of inertia in roll, A (slug ft^2)	0·933	0·948	0·854	0·923	0·920	0·918	0·945	0·953
Moment of inertia in pitch, B (slug ft^2)	16·663	17·122	16·777	17·164	17·626	17·168	17·089	17·698
Moment of inertia in yaw, C (slug ft^2)	17·515	17·860	17·749	17·940	18·382	17·895	17·822	18·562
Product of inertia, E (slug ft^2)	0·145	0·148	0·147	0·149	0·305	0·148	0·147	0·231
Inclination of principal axes to horizontal datum (degrees)	$\frac{1}{2}$	$\frac{1}{2}$	$\frac{1}{2}$	$\frac{1}{2}$	1	$\frac{1}{2}$	$\frac{1}{2}$	$\frac{3}{4}$
Inertia coefficients: i_A	0·064	0·063	0·057	0·060	0·059	0·056	0·063	0·060
i_B	1·104	1·097	1·077	1·084	1·092	1·058	1·095	1·076
i_C	1·205	1·228	1·184	1·176	1·183	1·146	1·186	1·172
i_E	0·010	0·010	0·010	0·010	0·020	0·009	0·010	0·015

Table 3

MEASUREMENT RANGES OF MODEL INSTRUMENTATION

Measurement \ Model No.	1	2	3	4	5	6	7	8
Normal acceleration forward	±10g	±5g	±5g	±5g	±5g	±5g	±5g	±5g
c.g.	±15g	±7½g	±7½g	±7½g	±7½g	±7½g	±7½g	±7½g
c.g. (high range)	-	±30g	±30g	±30g	±30g	-	-	-
aft	±20g	±10g	±10g	±10g	±10g	±10g	±10g	±10g
Angle of incidence (differential pressure)	±5 psi	±5 psi	±5 psi	±7½ psi	±7½ psi	±10 psi	±10 psi	±10 psi
Pitot pressure	-	-	-	-	-	0 to 80 psia	0 to 80 psia	0 to 80 psia
Angle of sideslip (differential pressure)	±5 psi	±5 psi	±5 psi	±7½ psi	±7½ psi	±10 psi	±10 psi	±10 psi
Lateral acceleration forward	±5g	-	-	±7½g	-	±7½g	±5g	±3g
c.g.	±7½g	±7½g	±7½g	±7½g	±7½g	±7½g	±5g	±3g
aft	±10g	-	-	±7½g	-	±7½g	±5g	±3g
Angular acceleration in roll	-	-	-	±100 rad/sec^2	-	±56 rad/sec^2	±56 rad/sec^2	±56 rad/sec^2
Longitudinal deceleration	-	0 to 5g	0 to 5g	0 to 5g	0 to 5g	-	-	-
Maximum duct pressure port	0 to 30 psig	0 to 30 psig	0 to 30 psig	0 to 30 psig	0 to 30 psig	0 to 30 psig	-	-
starboard	0 to 30 psig	0 to 30 psig	0 to 30 psig	0 to 30 psig	0 to 30 psig	-	0 to 30 psig	0 to 30 psig
Duct exhaust pressure port	-5 to +10 psig	-5 to +10 psig	-5 to +10 psig	-5 to +10 psig	-5 to +10 psig	-5 to +10 psig	-	-
starboard	-5 to +10 psig	-5 to +10 psig	-5 to +10 psig	-5 to +10 psig	-5 to +10 psig	-	-5 to +10 psig	-5 to +10 psig

Table 4

POSITIONS OF ACCELEROMETERS

The coordinates of each instrument are given in inches as follows:

x	forward from the c.g.
y	starboard from the model centre line
z	downwards from the Horizontal Datum

Coordinate	x							y				z			
Model number	2	3	4	5	6	7	8	4	6	7	8	4	6	7	8
<u>Linear accelerometers</u>															
Normal forward	17.25	17.21	15.25	17.21	16.48	17.81	15.02	0	0.91	0	0	1.38	9.13	0.09	0.10
c.g.	0	- 0.06	0	- 0.04	- 0.31	- 0.09	- 0.03	- 0.46	0	0.83	0.89	0.16	1.37	1.45	1.45
c.g. (high range)	0	- 0.06	0	- 0.04	-	-	-	- 1.29	-	-	-	0.16	-	-	-
aft	-28.70	-28.76	-29.26	-28.74	-26.92	-26.44	-26.73	0	-0.49	-0.28	-0.21	-0.12	1.24	0.14	0.38
Lateral forward	-	-	36.10	-	16.48	17.81	15.02	0	-0.19	0	0	3.0	1.43	2.26	2.20
c.g.	0	- 0.06	0	- 0.04	- 1.59	- 0.09	- 0.03	1.22	0.46	-0.80	-0.85	0.16	1.15	1.63	1.63
aft	-	-	-27.76	-	-27.72	-27.33	-27.73	0	0	0.16	0.34	0.06	-0.65	-0.32	0.57
Longitudinal	- 1.50	- 1.56	+ 1.74	- 1.54	-	-	-	0	-	-	-	0.16	-	-	-
<u>Angular accelerometer</u>															
Roll	-	-	-12.62	-	-13.26	-12.33	-12.43	0	-0.11	0	0	0.48	0.65	1.45	0
<u>Nose probe</u> (tip)	52.07	51.94	52.06	52.01	51.11	51.33	50.92	-	-	-	-	-	-	-	-

Table 5

DATA USED FOR RESPONSES SHOWN IN FIGS.49-52

$S = 4{\cdot}88$ sq ft; $\bar{c} = 1{\cdot}58$ ft; $s = 1{\cdot}55$ ft

Fig. No.	49	50	51	52
M	1·6	1·6	1·7	1·4
c.g.	0·44 $\bar{c}$	0·28 $\bar{c}$	0·264 $\bar{c}$	0·264 $\bar{c}$
W (lb)	186	202	205	205
A (slug ft^2)	1·07	1·08	0·923	0·923
B (slug ft^2)	10·7	15·7	17·16	17·16
C (slug ft^2)	11·4	16·4	17·94	17·94
E (slug ft^2)	0·352	0·352	0·149	0·149
Y_B (lb wt)	140 for 0·07 sec	140 for 0·07 sec	-	- , 200 for 0·05 sec
L_B (lb ft)	+35 for 0·07 sec	+35 for 0·07 sec	-	- , for 0·05 sec
N_B (lb ft)	-408 for 0·07 sec	-378 for 0·07 sec	-	- , for 0·05 sec
y_v	-0·375	-0·375	-0·365	-0·398*
z_w	-1·42	-1·42	-1·37	-1·56*
ℓ_v	-0·088	-0·088	-0·083	-0·094
ℓ_{vw}	0	0	-0·4 or 0	-0·6
ℓ_p	-0·175	-0·175	-0·172	-0·183**
ℓ_r	0·115	0·131	0·127	0·141
m_w	-0·342	-0·543	-0·539	-0·575
$m_{\dot{w}}$	-0·094	-0·108	-0·099	-0·160
m_q	-0·581	-0·505	-0·694	-0·778
n_v	0·093	0·156	0·120	0·206*
n_{vw}	0	0	0	0
n_p	0·010	0·010	0·012	0·002
n_r	-0·71	-0·74	-0·719	-0·783

*Experimental free flight values.

**Confirmed by later experiments.

Table 6

CALCULATED CHARACTERISTICS OF THE RESPONSES

Fig. No.	49	50	51	52
M	1·6	1·6	1·7	1·4
Uncoupled motion				
Longitudinal				
ν_1 (c/s)	6·29	6·45	7·14	6·02
$C_{\frac{1}{2}}$	1·23	1·59	1·44	1·27
Lateral				
ν_2 (c/s)	2·68	3·12	3·15	3·15
$C_{\frac{1}{2}}$	2·04	2·37	1·86	2·14
Coupled motion				
Approx. steady state				
$\pm p_{crit}$ (rad/sec)	20·2	21·9	19·5	21·4
$\sqrt{N'_v}$ (rad/sec)	19·8	21·4	19·0	20·5
$\pm p_s$ (rad/sec)	42·7	42·9	45·4	38·6
$\sqrt{M'_w}$ (rad/sec)	39·5	41·1	44·8	38·1
α_s (rad)	0·28		0·36	0·29
$\pm\beta_s$ (rad)	0·067		0·059	0·061
q_s (rad/sec)	1·65		1·22	1·26
$\pm r_s$ (rad/sec)	12·2		16·5	11·3
Approx. frequencies				
Equation (A19) (c/s)	12·2		12·7	11·0
Equation (A20), $L'_{vw} = 0$ (c/s)	11·6, 5·3		12·0, 8·2	10·5, 6·1
Equation (A20), (with analogue α_s) (c/s)			11·9, 8·0	10·1, 6·1

SYMBOLS

a_y	lateral acceleration of the c.g., as a multiple of g
A	moment of inertia in roll, slug ft^2
b_x	$= (C - B)/A$
b'_y	$= (C - A)/B$
b_z	$= (B - A)/C$
B	moment of inertia in pitch, slug ft^2
$\bar{c}$	geometric mean chord of gross wing, ft
C	moment of inertia in yaw, slug ft^2
C_L	lift coefficient $\Big\}$ $= \text{force}/\frac{1}{2}\rho V^2 S$
C_D	drag coefficient
$C_{\frac{1}{2}}$	number of cycles to half amplitude
D_1	distance of longitudinal focal point from c.g., ft
D_2	distance of lateral focal point from c.g., ft
e'_x	$= E/A$
e'_y	$= E/B$
e'_z	$= E/C$
E	product of inertia, slug ft^2
g	acceleration due to gravity, ft/sec^2
i_A	$= A/ms^2$
i_B	$= B/m\bar{c}^2$
i_C	$= C/ms^2$
i_E	$= E/ms^2$
ℓ_B	$= L_B/\rho SV^2 s$
ℓ_p	$= L_p/\rho SVs^2$
ℓ_r	$= L_r/\rho SVs^2$
ℓ_v	$= L_v/\rho SVs$
ℓ_{vw}	$= L_{vw}/\rho Ss$
ℓ_ξ	$= L_\xi/\rho SV^2 s$
L	rolling moment, lb ft
L_B	rolling moment due to pulse rocket, lb ft
L'_B	$= L_B/A$
L_p	$= \partial L/\partial p$
L'_p	$= -L_p/A$
L_r	$= \partial L/\partial r$
L'_r	$= L_r/A$
L_v	$= \partial L/\partial v$
L'_v	$= -L_v/A$

SYMBOLS (Contd)

L_{vw} $= \partial^2 L/\partial v \, \partial w = \partial(L_v)/\partial w$

L'_{vw} $= -L_{vw}/A$

L_ξ $= \partial L/\partial \xi$

L'_ξ $= -L_\xi/A$

m mass of model, slugs

m_B $= M_B/\rho S V^2 \bar{c}$

m_q $= M_q/\rho S V \bar{c}^2$

m_w $= M_w/\rho S V \bar{c}$

$m_{\dot{w}}$ $= M_{\dot{w}}/\rho S \bar{c}^2$

M Mach number; pitching moment, lb ft

M_B pitching moment due to pulse rocket, lb ft

M'_B $= M_B/B$

M_D pitching moment due to booster-rocket separation, lb ft

M_q $= \partial M/\partial q$

M'_q $= -M_q/B$

M_w $= \partial M/\partial w$

M'_w $= -M_w/B$

$M_{\dot{w}}$ $= \partial M/\partial \dot{w}$

$M'_{\dot{w}}$ $= -M_{\dot{w}}/B$

n_B $= N_B/\rho S V^2 s$

n_p $= N_p/\rho S V s^2$

n_r $= N_r/\rho S V s^2$

n_v $= N_v/\rho S V s$

n_{vw} $= N_{vw}/\rho S s$

N yawing moment, lb ft

N_B yawing moment due to pulse rocket, lb ft

N'_B $= N_B/C$

N_D yawing moment due to booster-rocket separation, lb ft

N_p $= \partial N/\partial p$

N'_p $= -N_p/C$

N_r $= \partial N/\partial r$

N'_r $= -N_r/C$

N_v $= \partial N/\partial v$

N'_v $= N_v/C$

N_{vw} $= \partial^2 N/\partial v \, \partial w = \partial(N_v)/\partial w$

N'_{vw} $= -N_{vw}/C$

SYMBOLS (Contd)

p	rate of roll, rad/sec unless specified otherwise
p_{crit}	critical value of p
p_o	applied steady rate of roll
p_s	steady-state value of p
P_{max}	pressure at maximum cross-section of duct
P_{exh}	duct exhaust pressure
q	rate of pitch, rad/sec
q_s	steady state value of q
r	rate of yaw, rad/sec
r_s	steady-state value of r
s	semi-span of gross wing, ft
S	area of gross wing, ft^2
t	time, sec
$\hat{t}$	$= m/\rho SV$
v	sideslip velocity, ft/sec
V	forward velocity, ft/sec
w	vertical velocity, ft/sec
W	weight of model, lb
x	distance forward from the c.g., ft unless specified otherwise
y	distance to starboard from the model centre-line, ft unless specified otherwise
y_v	$= Y_v/\rho SV$
y_B	$= Y_B/\rho SV^2$
Y	side force, lb
Y_B	side force due to pulse rocket, lb
Y'_B	$= Y_B/mV$
Y_v	$= \partial Y/\partial v$
Y'_v	$= -Y_v/m$
z	distance downward from the horizontal datum, ft unless specified otherwise
z_B	$= Z_B/\rho SV^2$
z_w	$= Z_w/\rho SV$
Z	normal force, lb
Z_B	normal force due to pulse rocket, lb
Z'_B	$= Z_B/mV$
Z_w	$= \partial Z/\partial w$
Z'_w	$= -Z_w/m$

SYMBOLS (Contd)

α	$= w/V$ = angle of incidence, rad
α_s	steady-state value of α
β	$= v/V$ = angle of sideslip, rad
β_s	steady-state value of β
λ_1	exponential index of longitudinal damping
λ_2	exponential index of lateral damping
μ_1	$= m/\rho S\bar{c}$ = density ratio in longitudinal equations
μ_2	$= m/\rho Ss$ = density ratio in lateral equations
ν	frequency of coupled oscillations, cycles/sec
ν_1	frequency of the longitudinal short-period oscillation, cycles/sec
ν_2	frequency of the Dutch roll, cycles/sec
ξ_0	aileron angle, rad
ρ	air density, slug/ft^3
ω	$= 2\pi\nu$, rad/sec
ω_1	$= 2\pi\nu_1$ rad/sec
ω_2	$= 2\pi\nu_2$ rad/sec
ω_{n1}	$= (\omega_1^2 + \lambda_1^2)^{\frac{1}{2}}$ = longitudinal undamped natural frequency, rad/sec
ω_{n2}	$= (\omega_2^2 + \lambda_2^2)^{\frac{1}{2}}$ = lateral undamped natural frequency, rad/sec

REFERENCES

No.	Author	Title, etc
1	P. G. Hutton	Results of tests on a 1/25 scale stability model of the TSR2 in the A.R.A. 9 ft × 8 ft transonic tunnel. Aircraft Research Association Test Note P23, Parts 1, 2 and 3. 1962
2	M. C. Allen	Longitudinal and lateral stability and control effectiveness tests on the 1/64 scale type 571 Model 13. Vickers Armstrongs (Aircraft) Ltd. W.T. Report 2557, Parts 1 and 2. 1962
3	E. S. Greening	Longitudinal stability tests at M = 0·95, 1·39 and 1·66 on a 1/25 scale TSR2 model in the 4 ft × 4 ft wind tunnel. English Electric Aviation Ltd. W.T. Report AX/TSR2/72. 1963
4	E. S. Greening	Longitudinal stability tests in the E.E.A. 4 ft high-speed tunnel at Mach numbers from 0·7 to 0·95 on a 1/25 scale TSR2 model with and without external stores. English Electric Aviation Ltd. W.T. Report AX/TSR2/73. 1963
5	J. A. Hamilton P. A. Hufton	Free-flight techniques for high-speed aerodynamic research. Journal, R.Ae.S., <u>60</u>, 151 - 185, 1956
6	K. H. Doetsch	The time vector method for stability investigations. A.R.C. R & M 2945, August 1953
7	K. J. Turner	Measurements of dynamic stability from three simplified free-flight models of a supersonic research aircraft (Bristol ER.134) over the Mach number range 1·2 - 2·6. A.R.C. C.P. 816, March 1961

REFERENCES (Contd)

No.	Author	Title, etc
8	H. Voepel	Free-flight techniques for high-speed aerodynamic research. Unpublished M.O.A. work, 1960
9	H. H. B. M. Thomas S. Neumark	Interim note on stability and response characteristics of supersonic aircraft (linear theory). A.R.C. 18263, November 1955
10	-	TSR2 Aerodynamic Data (Basic Aircraft). English Electric Aviation Ltd. Aero Technical Notes Ae.159 and Ae.160. 1962
11	T. A. Cook	Supersonic wind-tunnel tests on a half conical centre-body side intake. A.R.C. 26334, July 1964
12	J. Picken	The uncertainty of processed data from free-flight experiments. R.A.E. Technical Note Aero 2604. 1959
13	C. H. E. Warren A. K. Weaver H. R. Hopkin S. Neumark	A proposed scheme of notation and nomenclature for the aerodynamics of aeroplanes and missiles. Unpublished M.O.A. work 1957
14	W. H. Phillips	Effect of steady rolling on longitudinal and directional stability. NACA Technical Note 1627. 1948
15	W. J. G. Pinsker	Preliminary note on the effect of inertia cross-coupling on aircraft response in rolling manoeuvres. A.R.C. C.P. 435, November 1955
16	H. H. B. M. Thomas P. Price	A contribution to the theory of aircraft response in rolling manoeuvres including inertia cross-coupling effects. A.R.C., R & M 3349, April 1960
17	-	TSR.2: Stability and control derivatives for rigid aircraft to Drawing 57193 sheet 00/17 issue A. English Electric Aviation Ltd. Aero Tech Note Ae/S/48. 1960

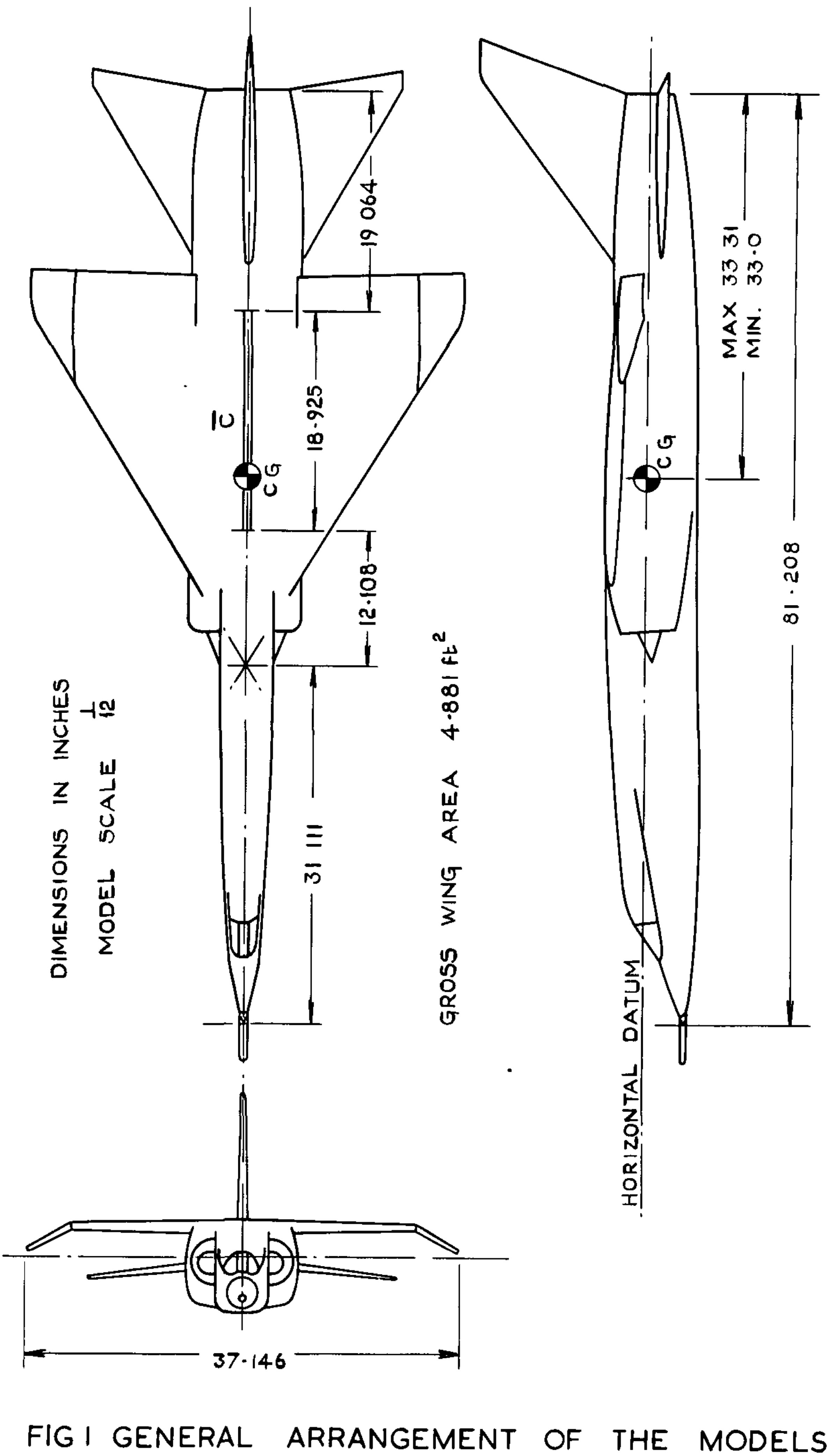

DIMENSIONS IN INCHES

MODEL SCALE $\frac{1}{12}$

GROSS WING AREA 4·881 ft^2

FIG I GENERAL ARRANGEMENT OF THE MODELS

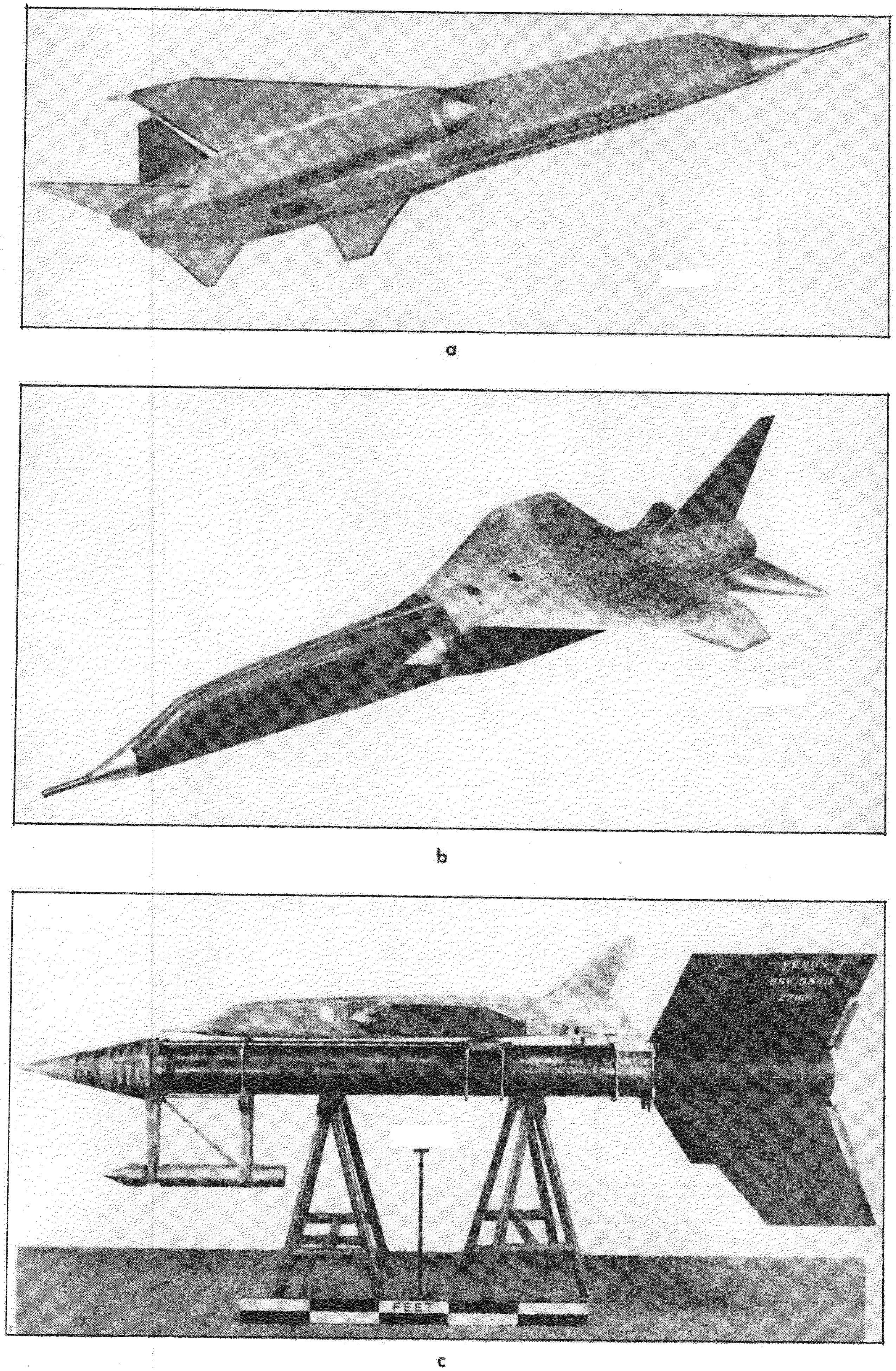

a

b

c

Fig.2. Photographs of the models

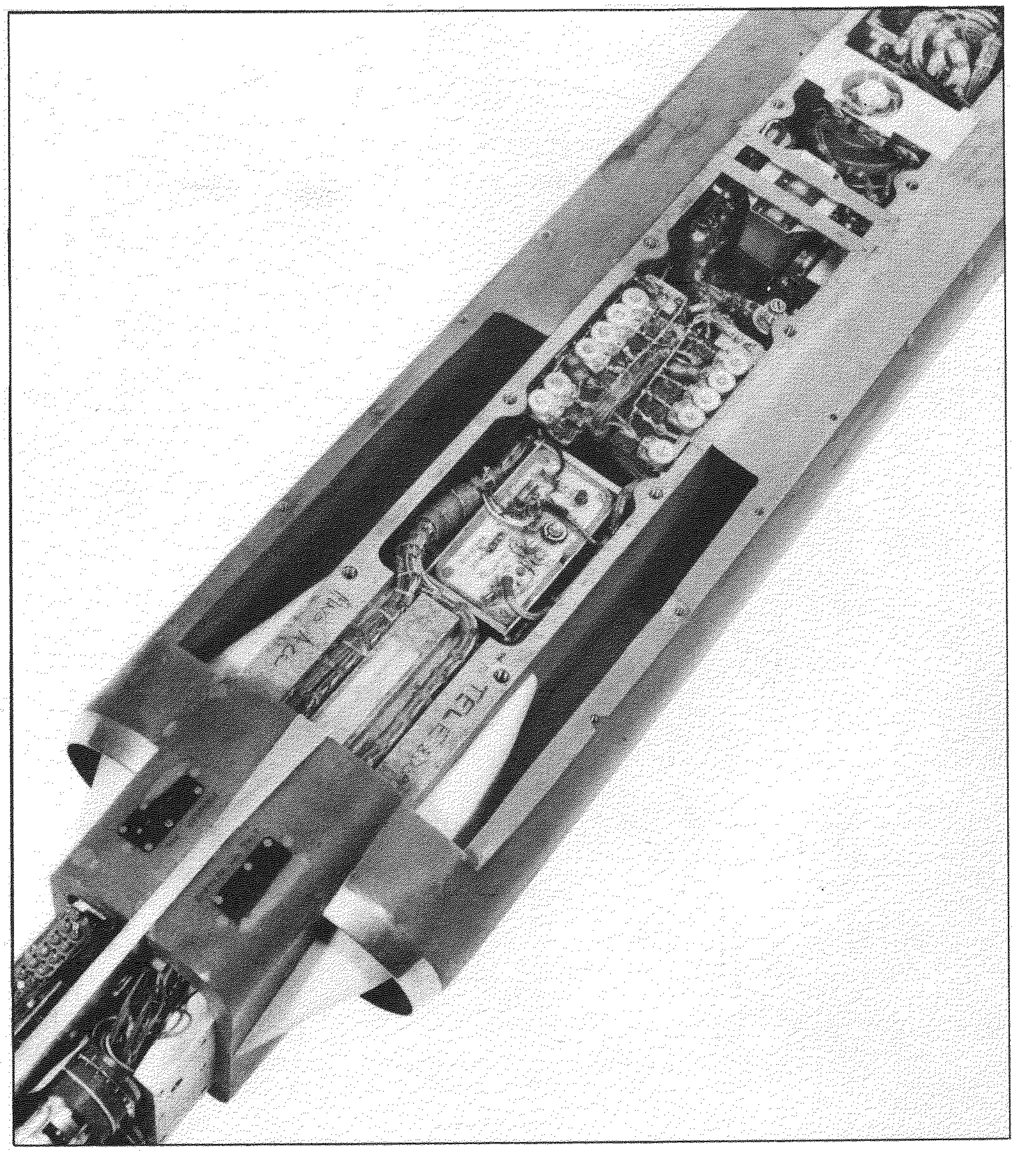

d

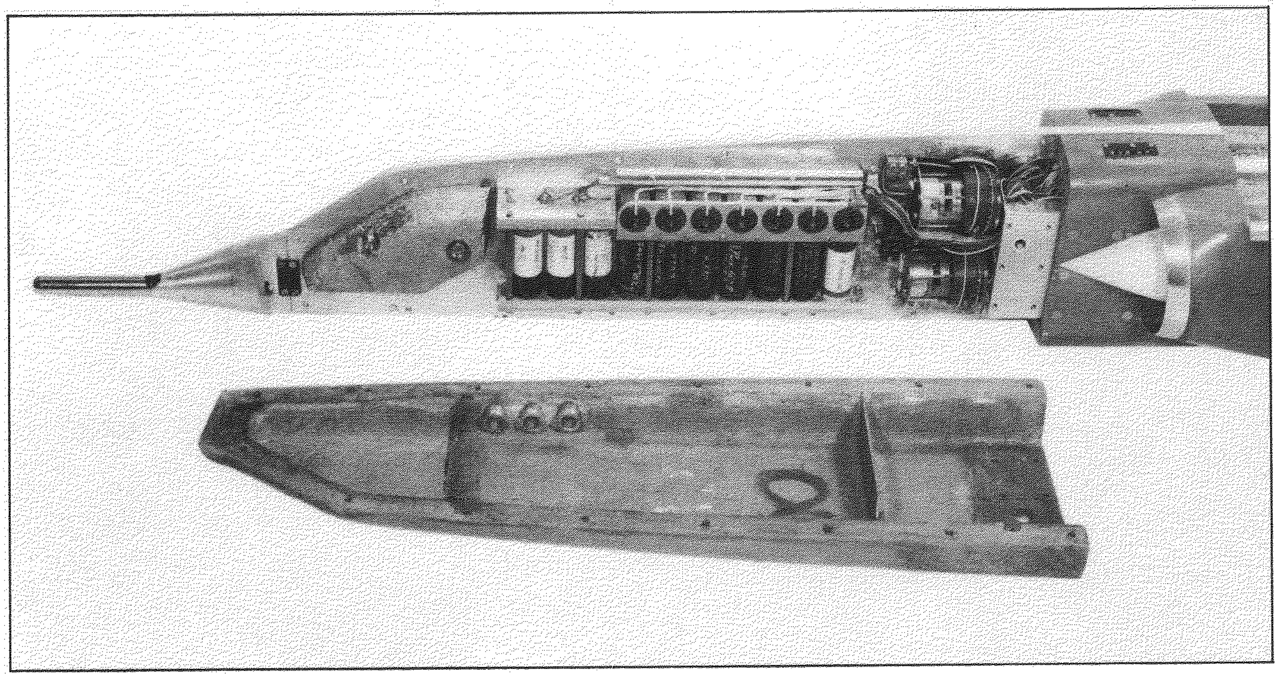

e

Fig.2 (cont'd). Photographs of the models

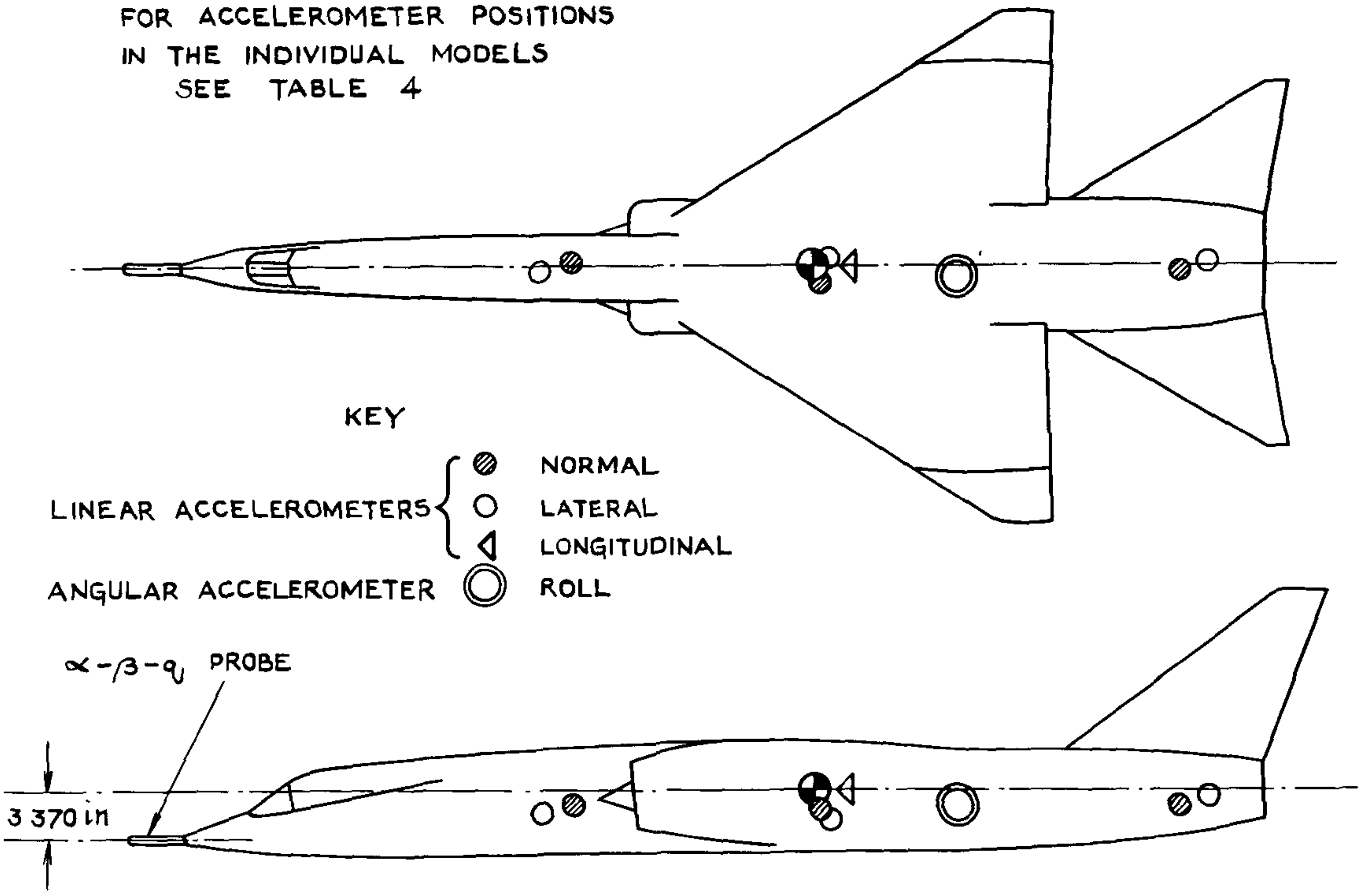

FIG. 3 TYPICAL ARRANGEMENT OF INSTRUMENTS

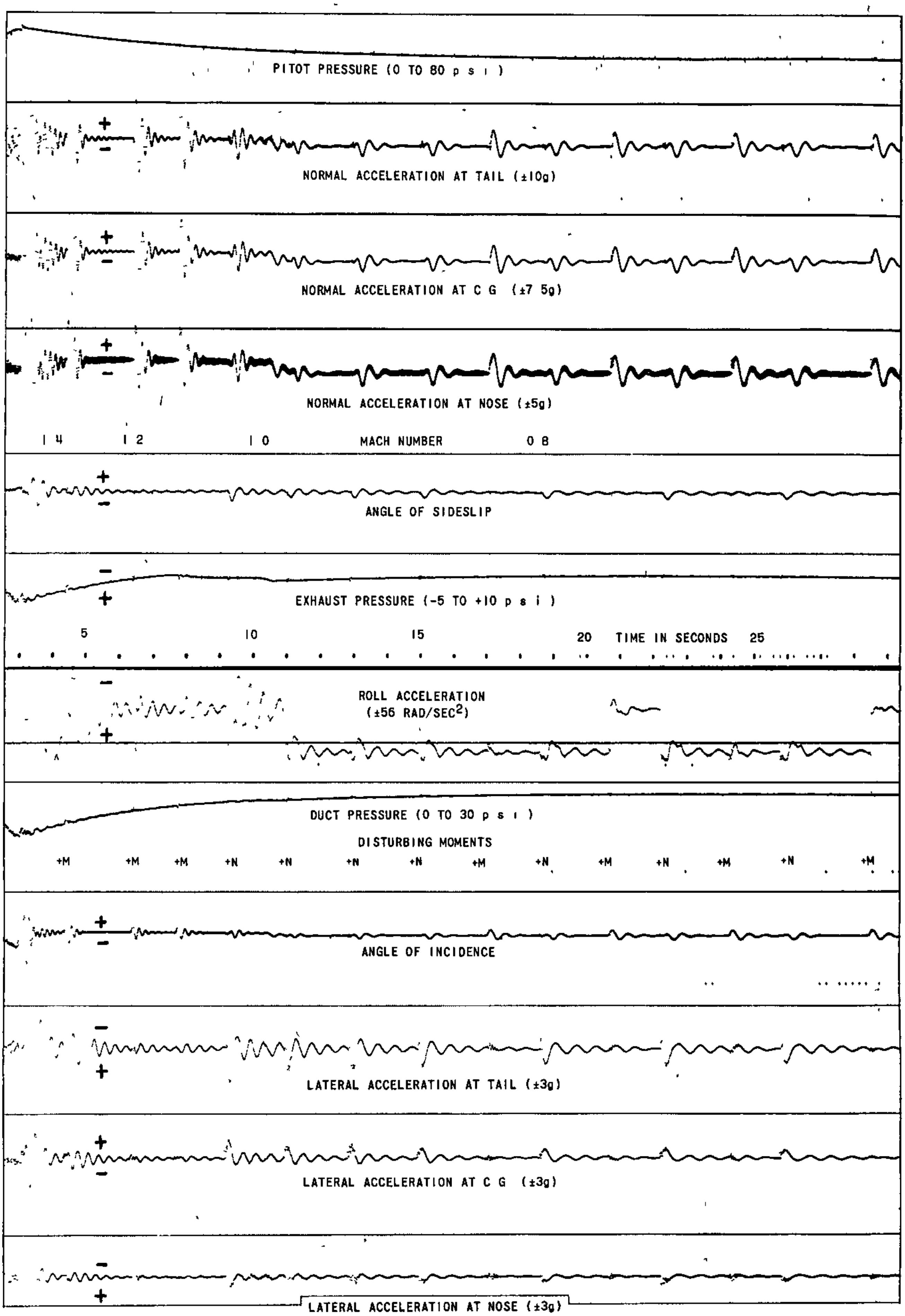

Fig 4 Typical Telemetry Record (Model 8)

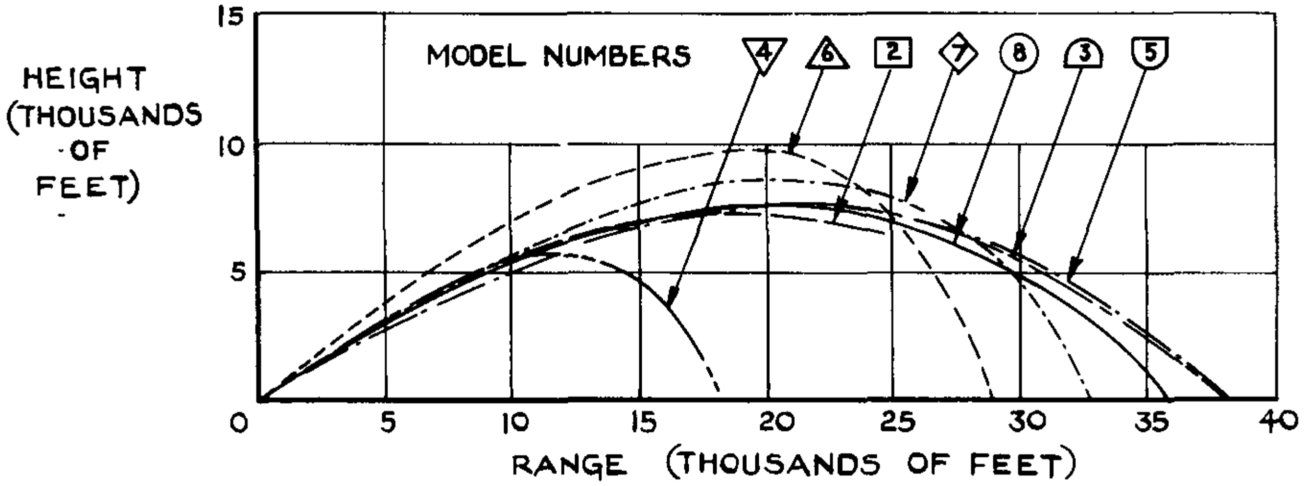

FIG. 5 MODEL FLIGHT PATHS

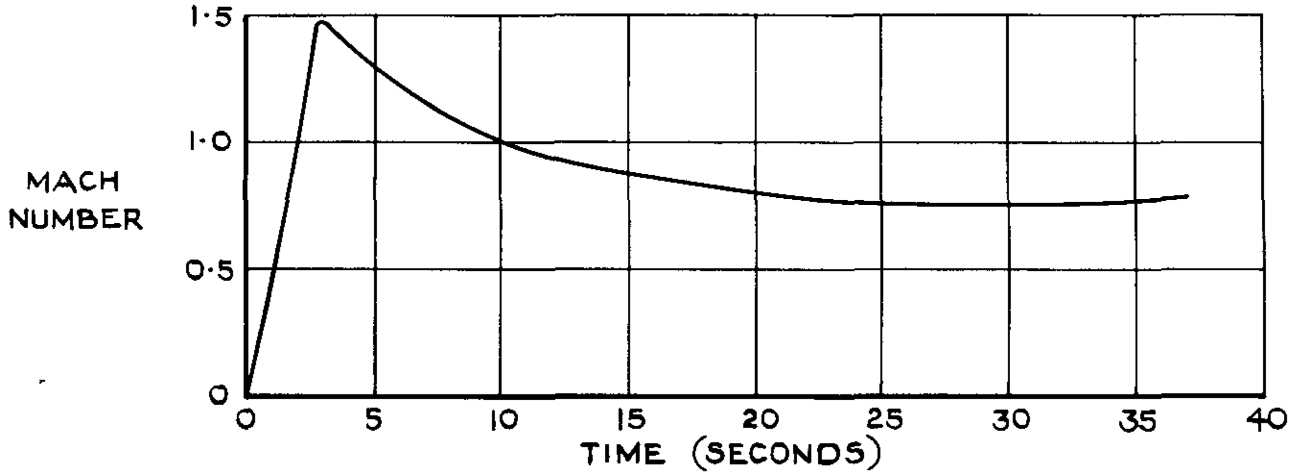

FIG. 6 TYPICAL VARIATION OF MACH NUMBER WITH TIME (MODEL 8)

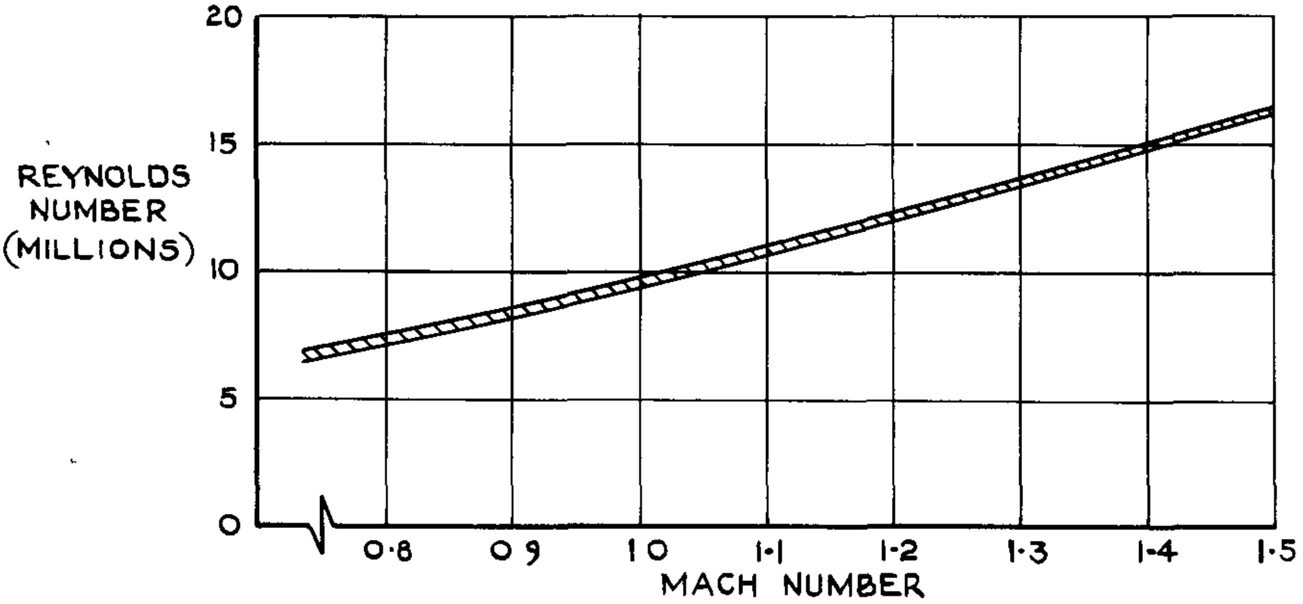

FIG 7 REYNOLDS NUMBER (BASED ON $\bar{C}$)

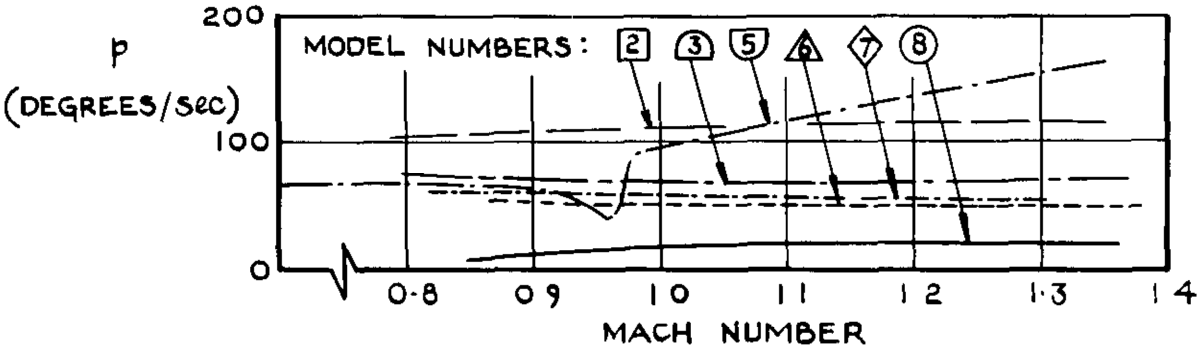

FIG.8 MEAN RATES OF ROLL

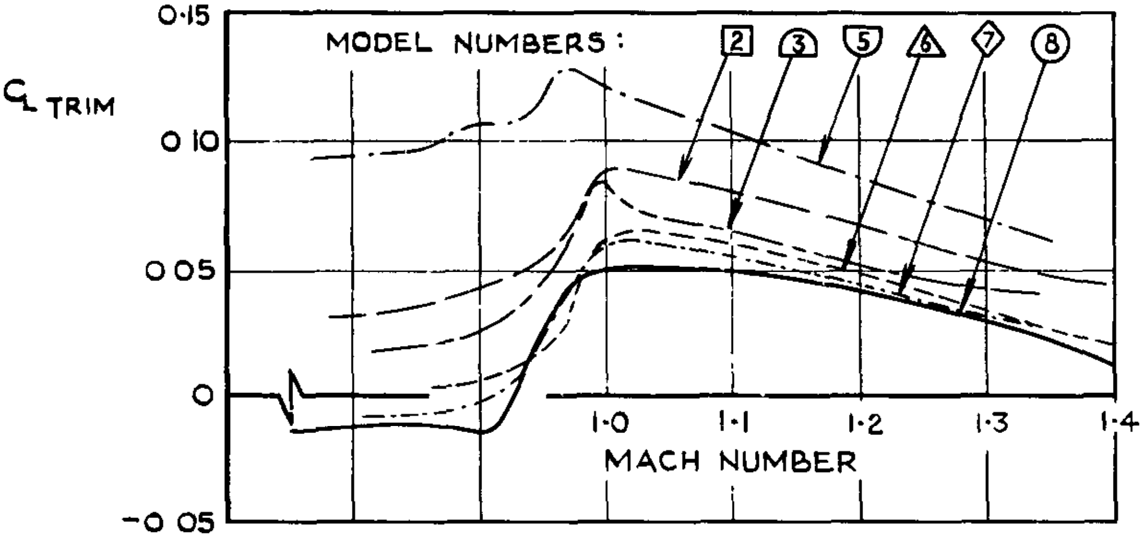

FIG.9 MEAN LIFT COEFFICIENTS

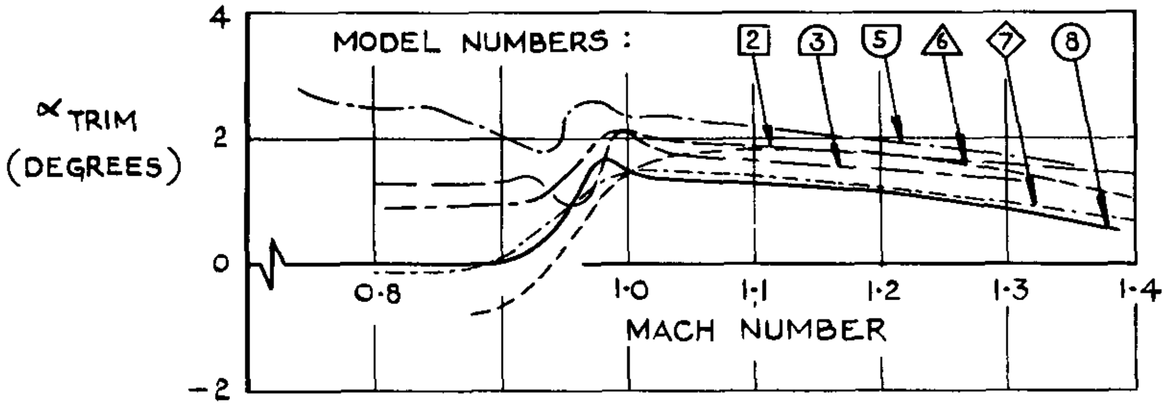

FIG.10 MEAN INDICATED ANGLES OF INCIDENCE

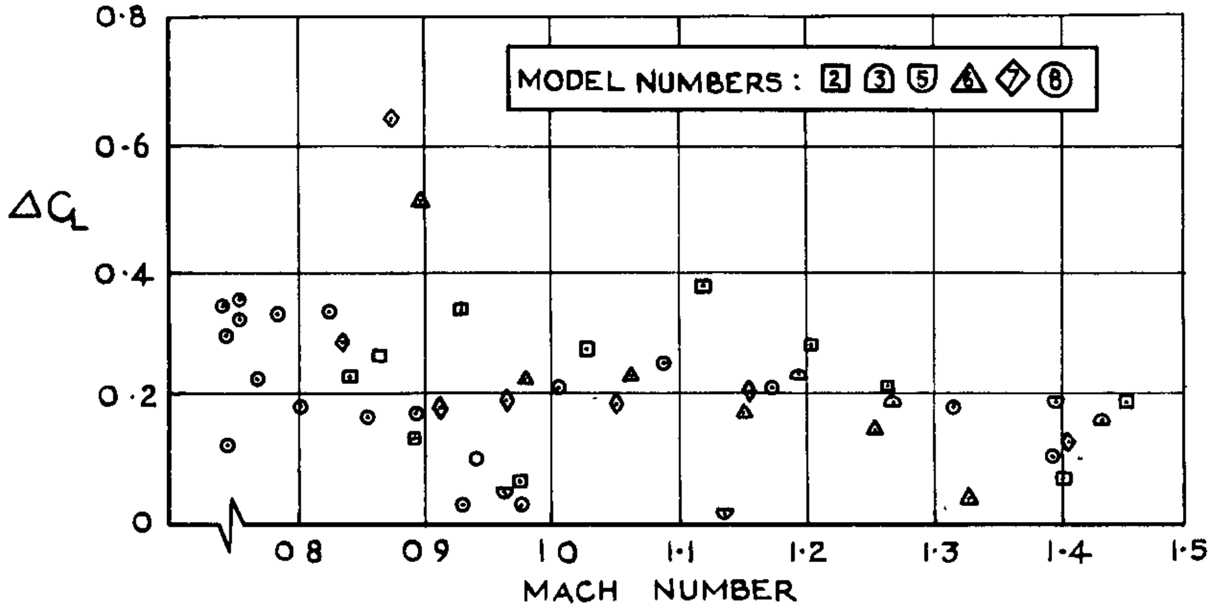

(a) LIFT COEFFICIENT

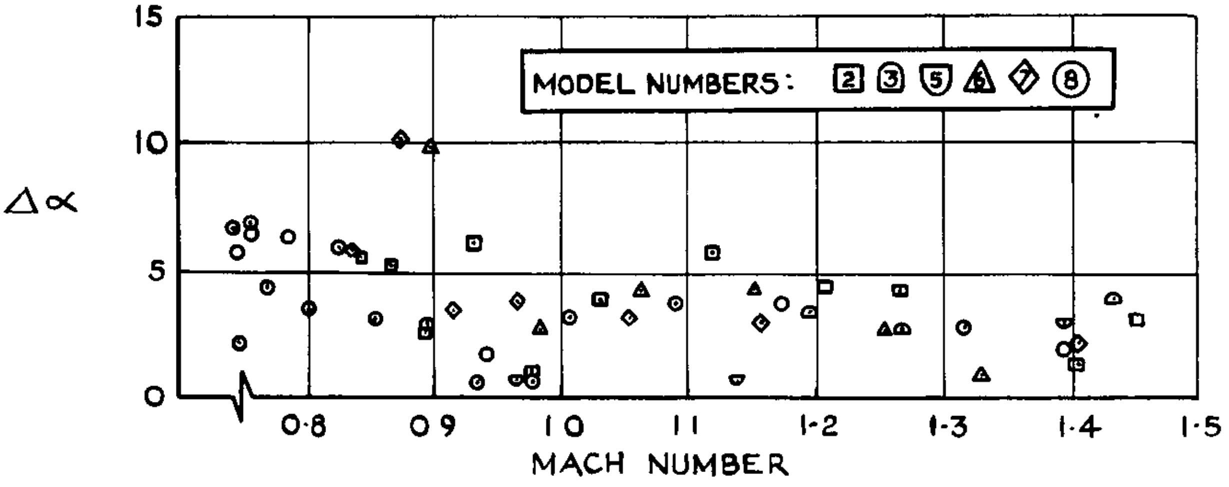

(b) INDICATED ANGLE OF INCIDENCE

FIG.11 MAXIMUM AMPLITUDES OF LONGITUDINAL OSCILLATIONS

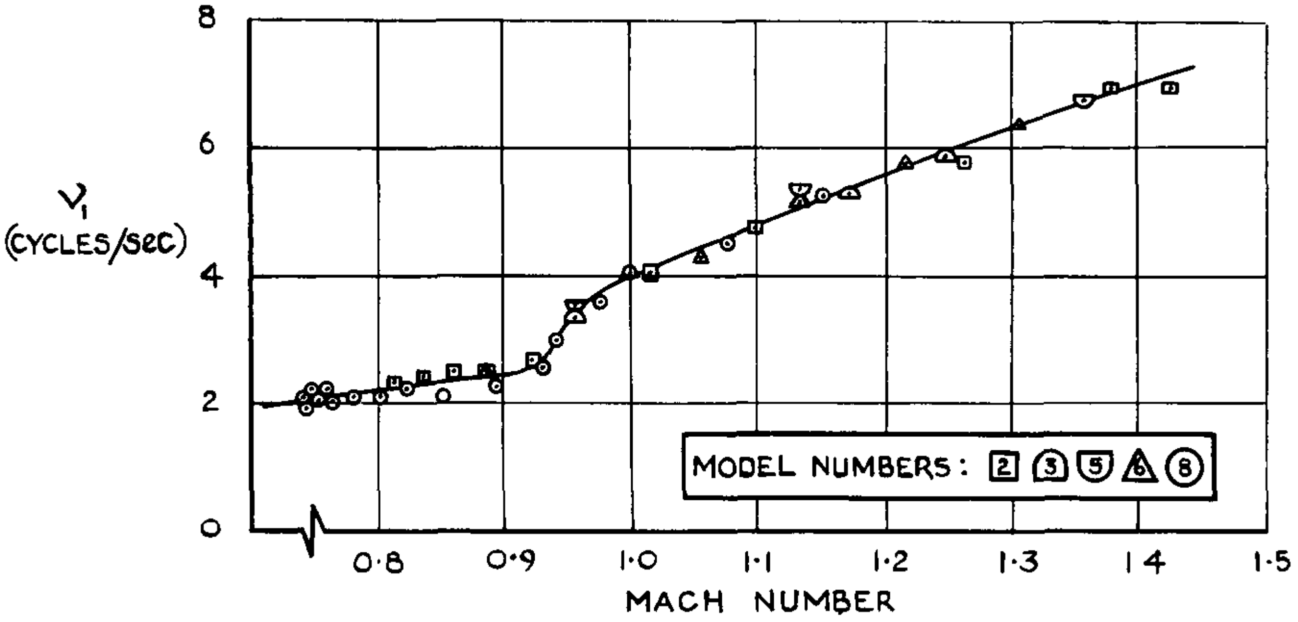

FIG. 12 FREQUENCY OF LONGITUDINAL SHORT-PERIOD OSCILLATION

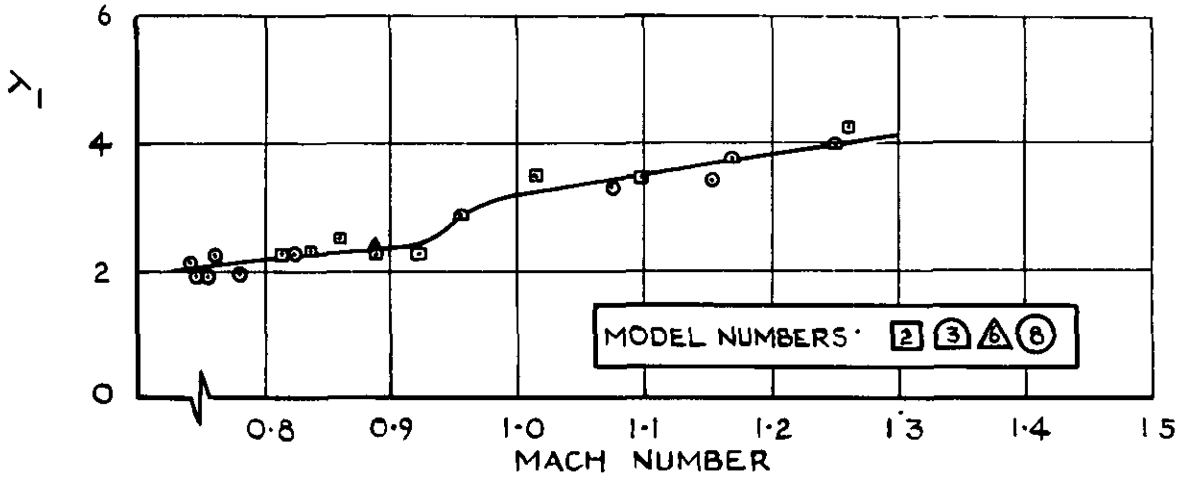

FIG. 13 TOTAL DAMPING OF LONGITUDINAL SHORT-PERIOD OSCILLATION

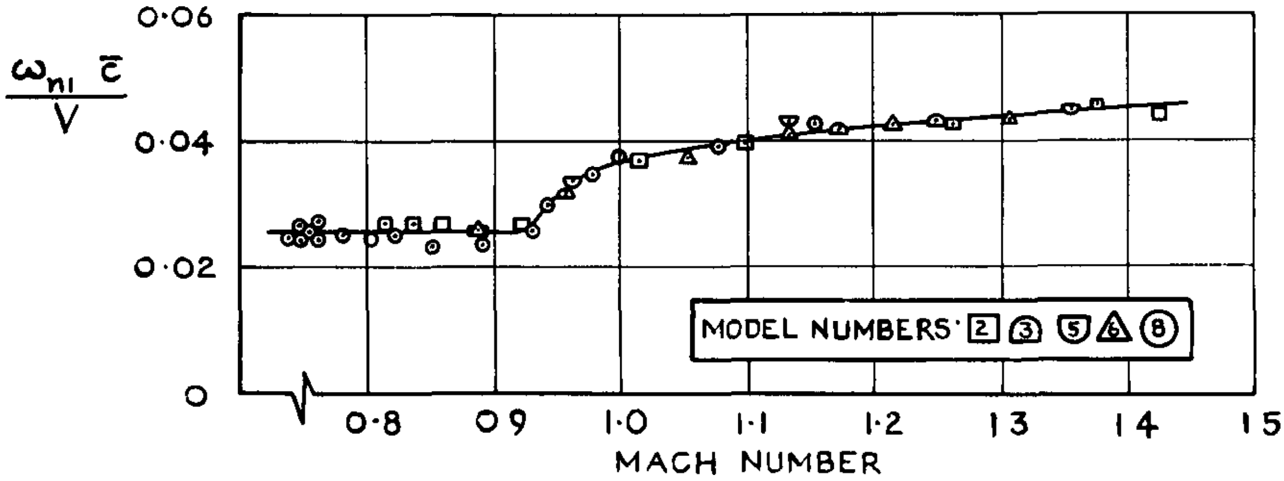

FIG. 14 REDUCED FREQUENCY OF LONGITUDINAL SHORT-PERIOD OSCILLATION

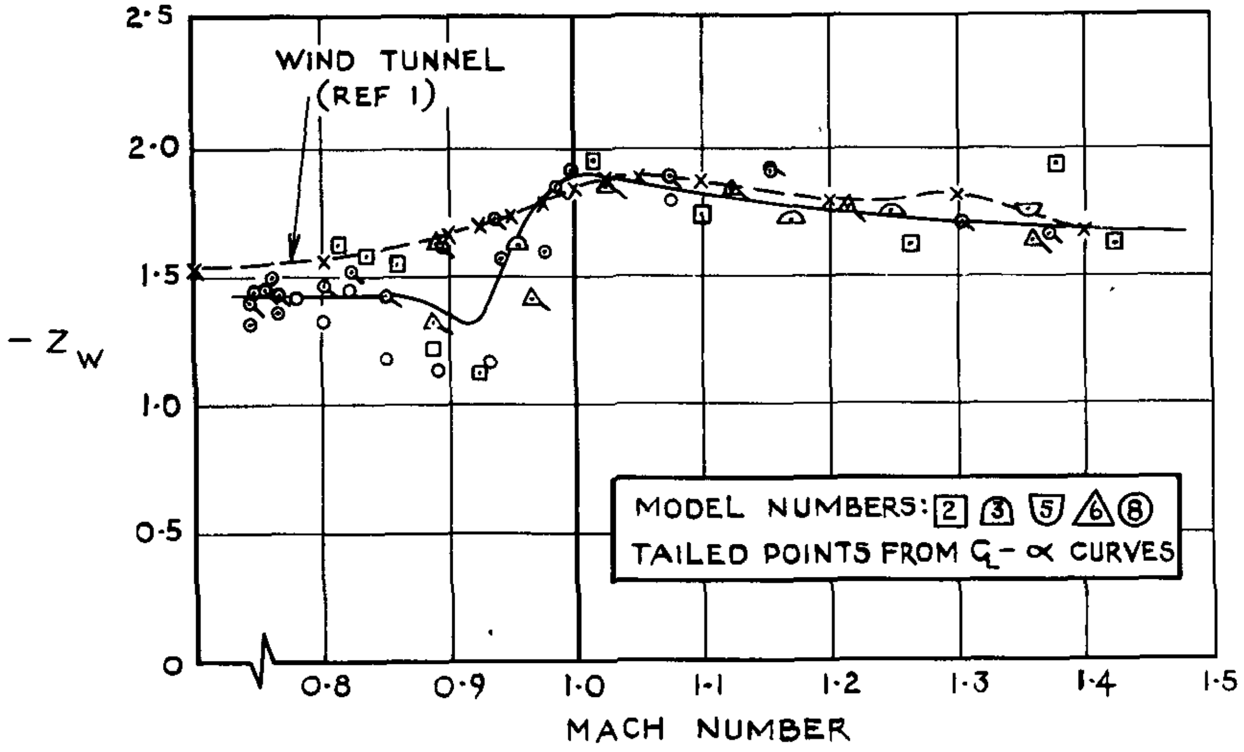

FIG. 15 NORMAL-FORCE DERIVATIVE z_w

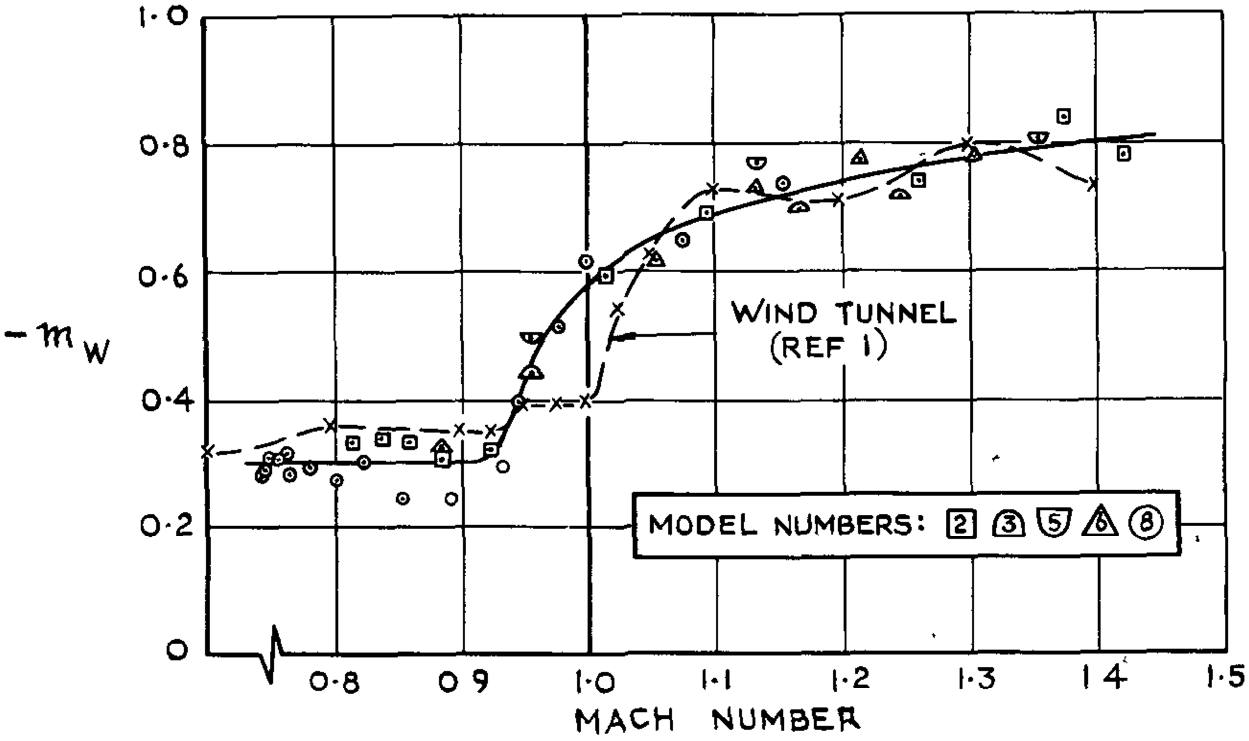

FIG. 16 PITCHING-MOMENT DERIVATIVE m_w

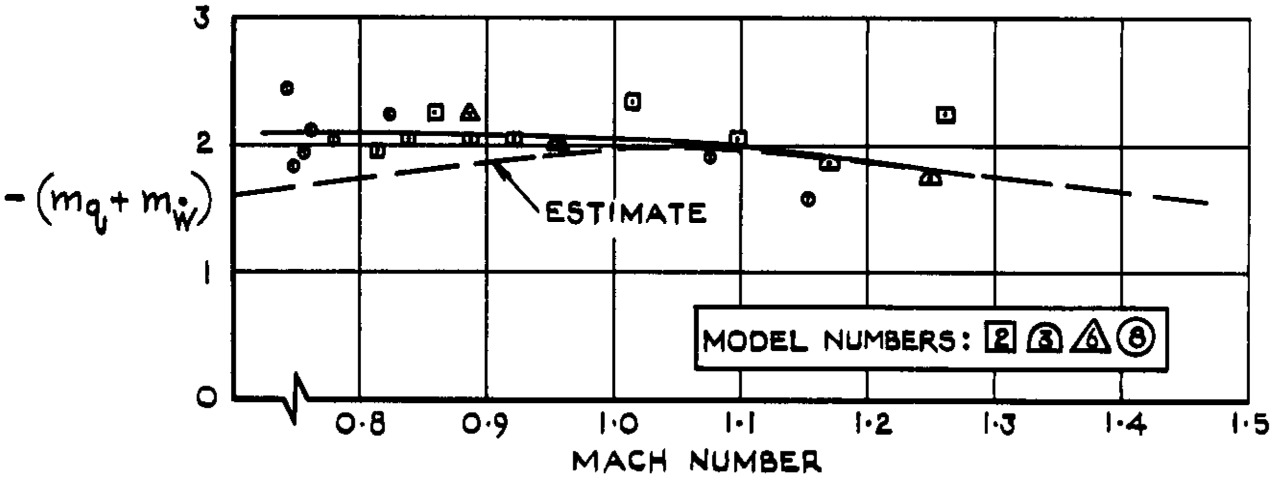

FIG.17 ROTARY DAMPING IN PITCH $(m_q + m_{\dot{w}})$

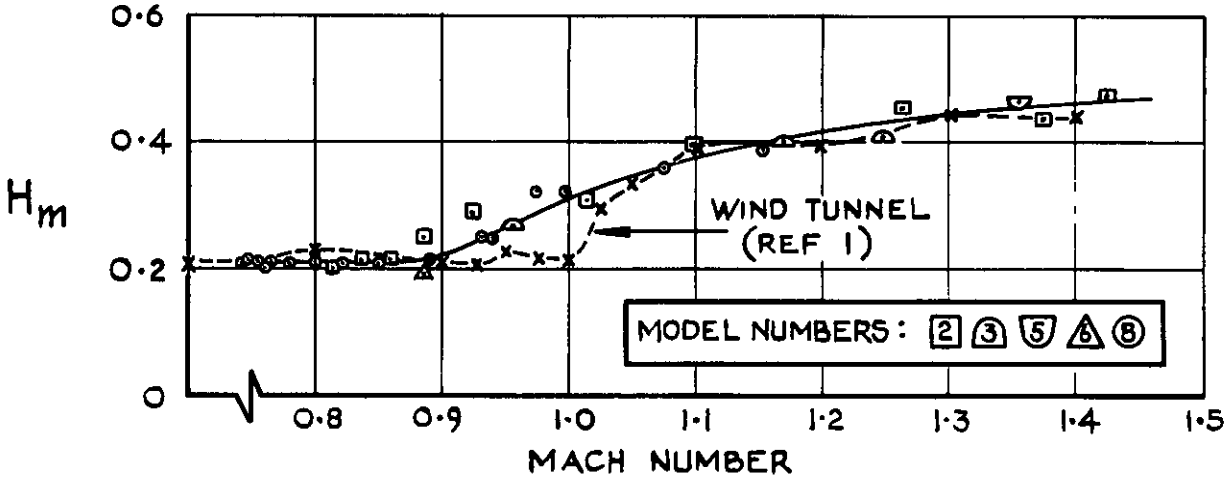

FIG. 18 MANOEUVRE MARGIN

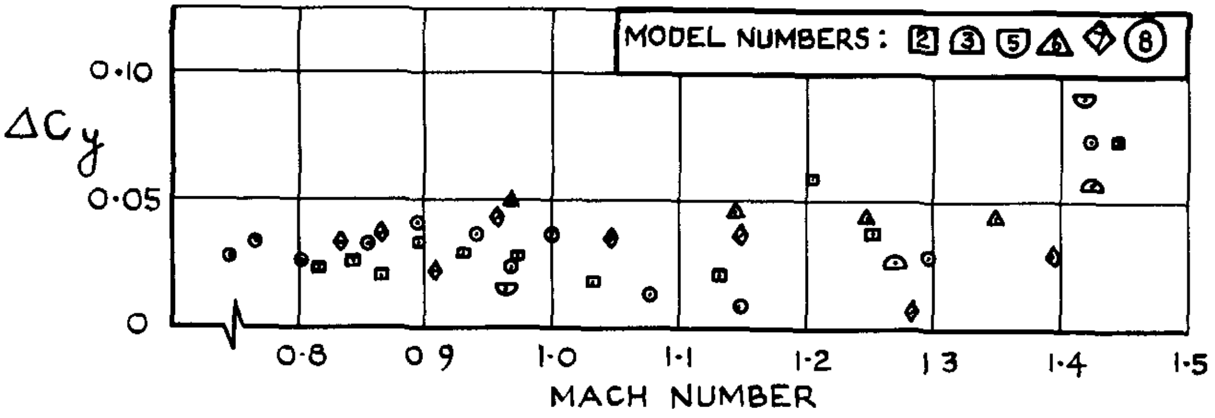

(a) LATERAL-FORCE COEFFICIENT

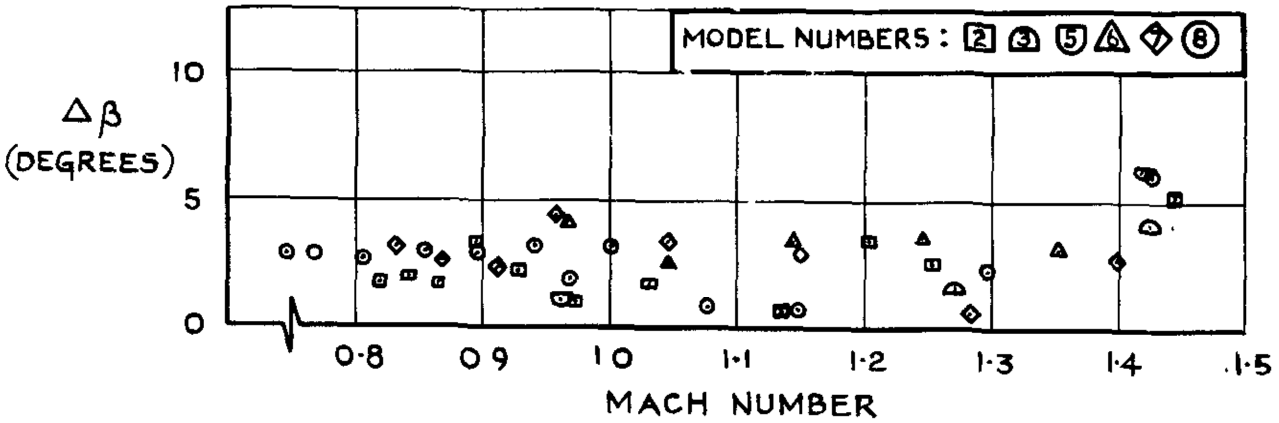

(b) INDICATED ANGLE OF SIDESLIP

FIG. 19 MAXIMUM AMPLITUDES OF LATERAL OSCILLATIONS

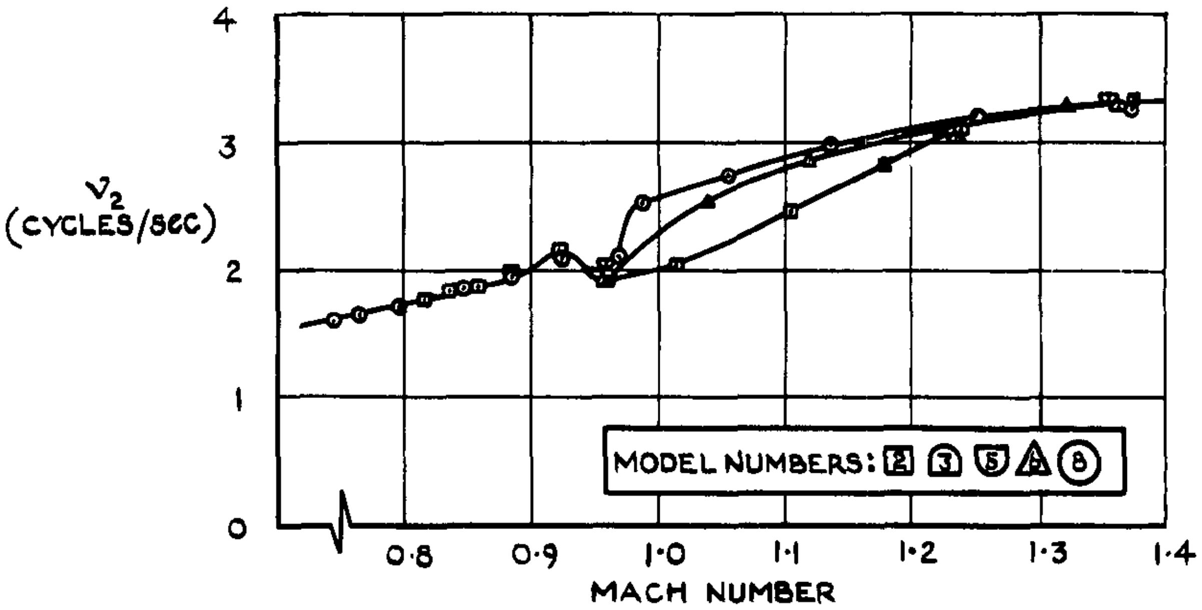

FIG. 20 FREQUENCY OF DUTCH ROLL

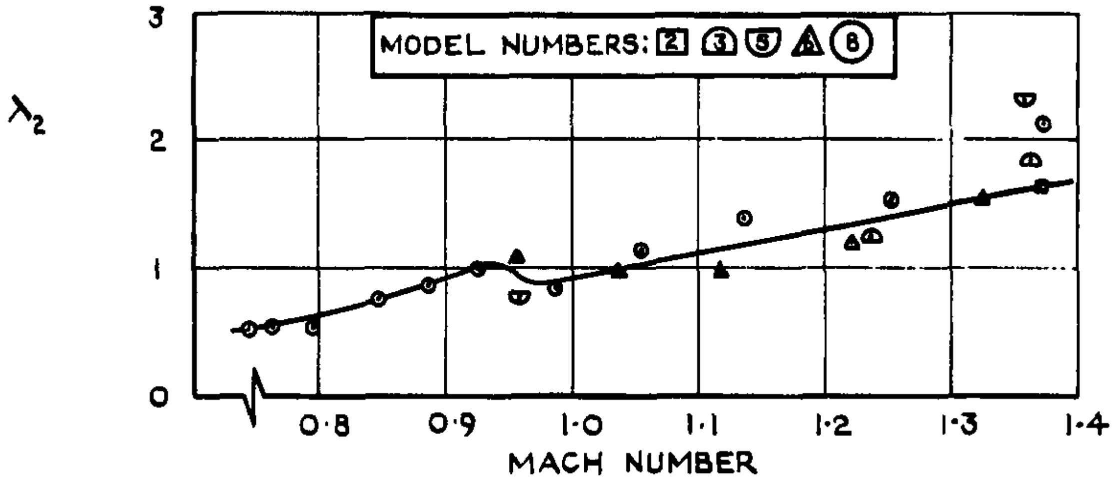

FIG. 21 TOTAL DAMPING OF DUTCH ROLL

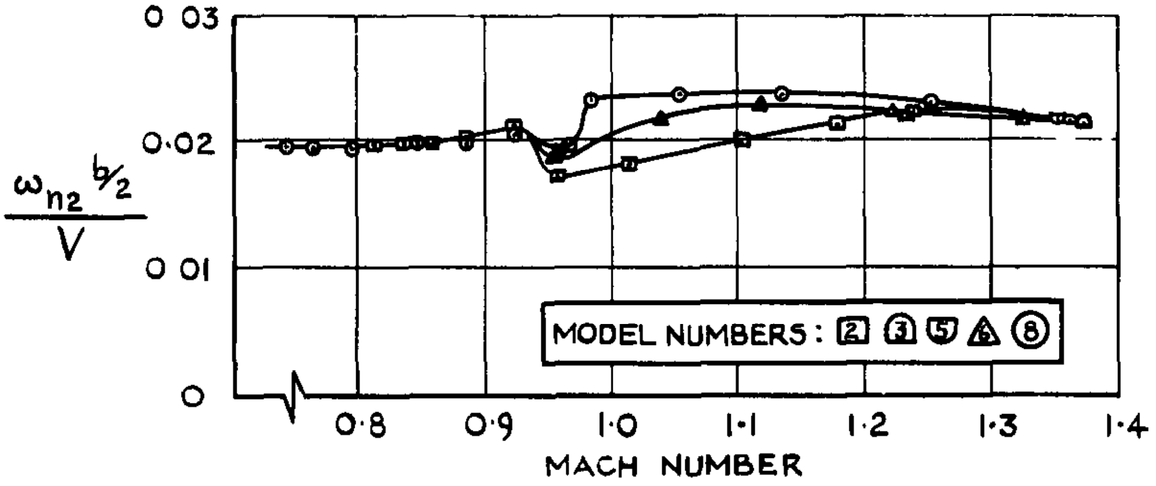

FIG. 22 REDUCED FREQUENCY OF DUTCH ROLL

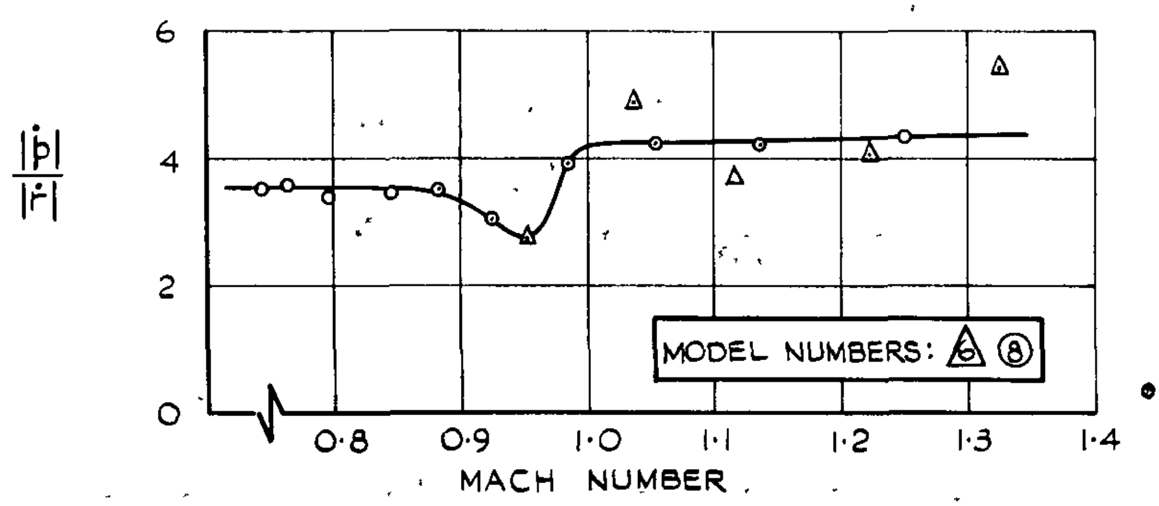

(a) ROLL: YAW RATIO

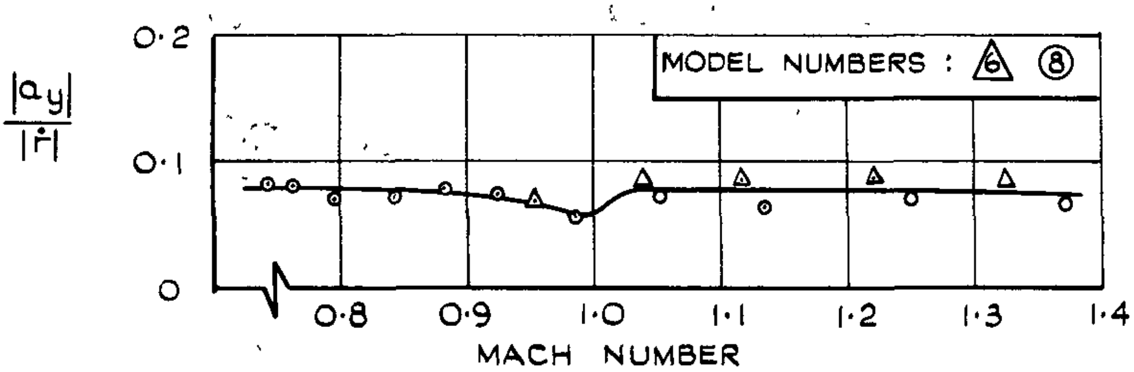

(b) LATERAL ACCELERATION: YAW RATIO

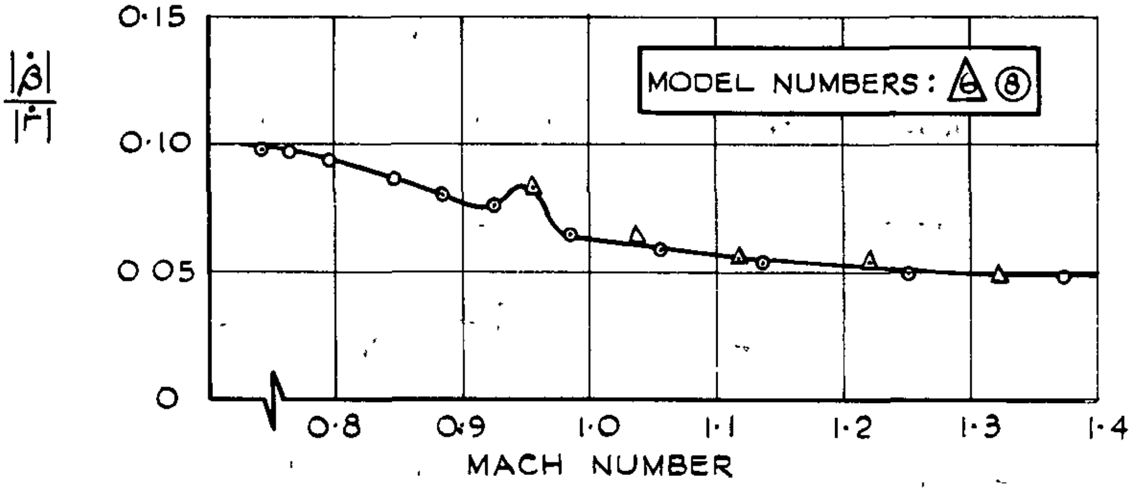

(c) SIDESLIP: YAW RATIO

FIG. 23 AMPLITUDE RATIOS OF DUTCH ROLL

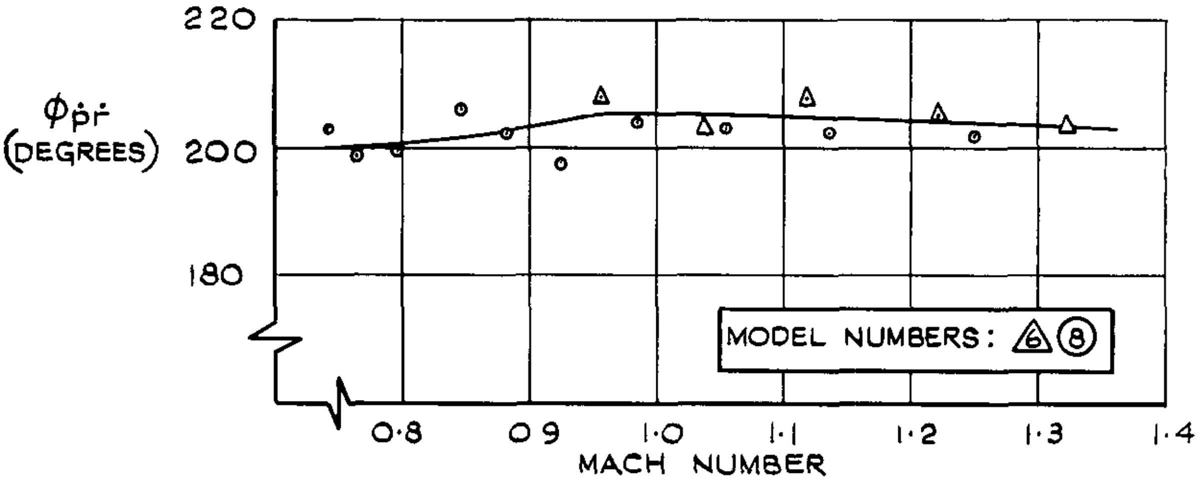

(a) ROLL-YAW PHASE ANGLE

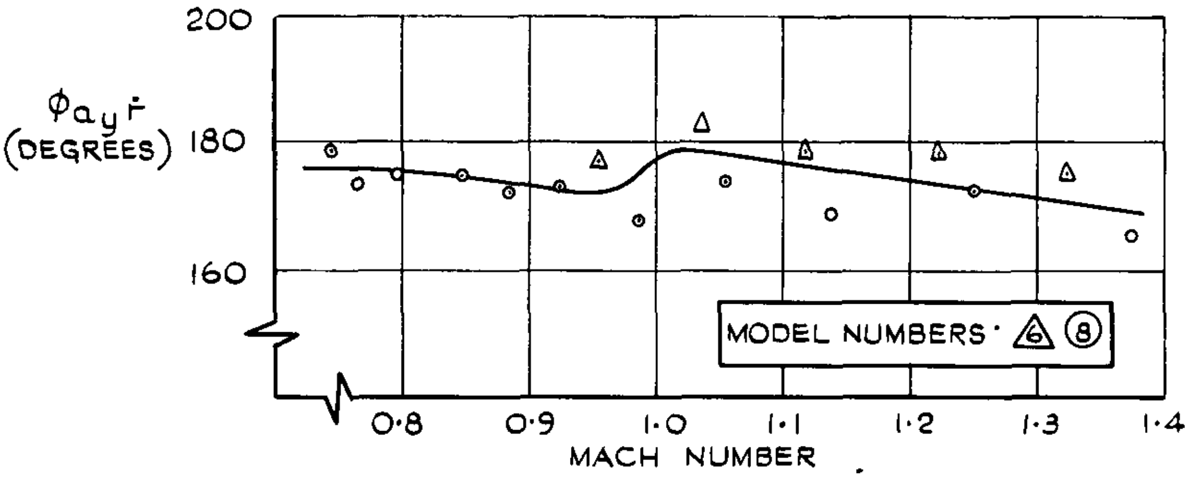

(b) LATERAL ACCELERATION - YAW PHASE ANGLE

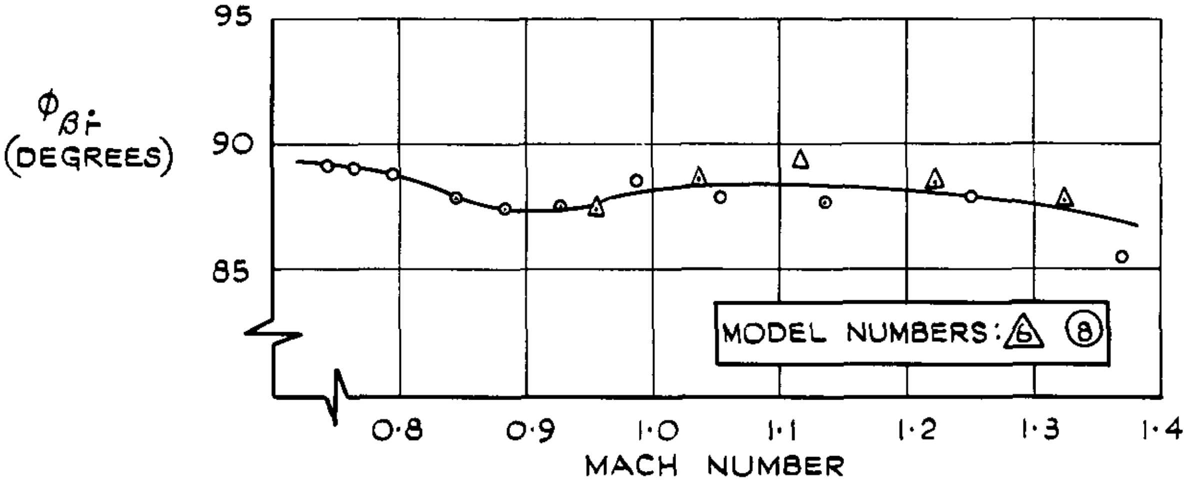

(c) SIDESLIP-YAW PHASE ANGLE

FIG. 24 PHASE RELATIONSHIPS OF DUTCH ROLL

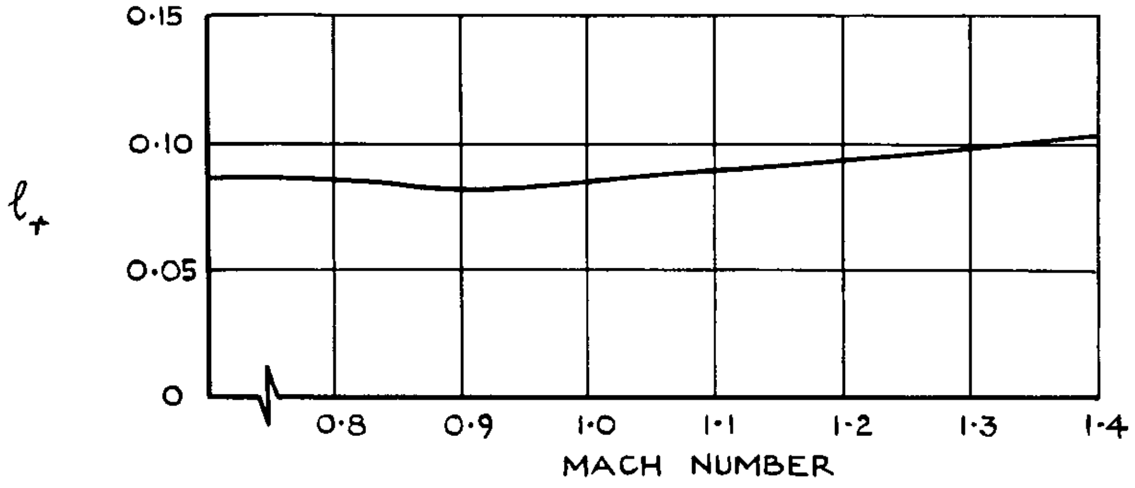

FIG. 25 ESTIMATE OF ROLLING-MOMENT DERIVATIVE l_r USED IN ANALYSIS

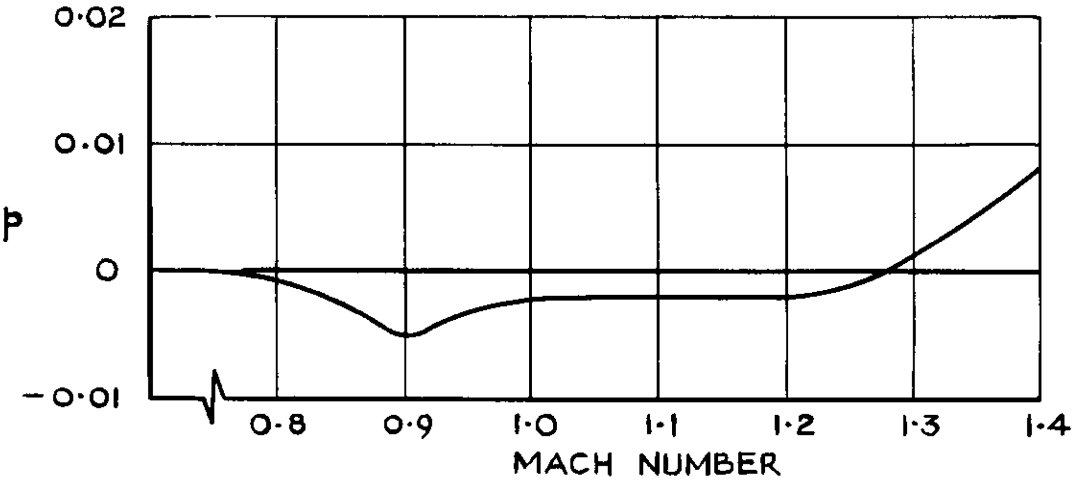

FIG. 26 ESTIMATE OF YAWING-MOMENT DERIVATIVE n_p USED IN ANALYSIS

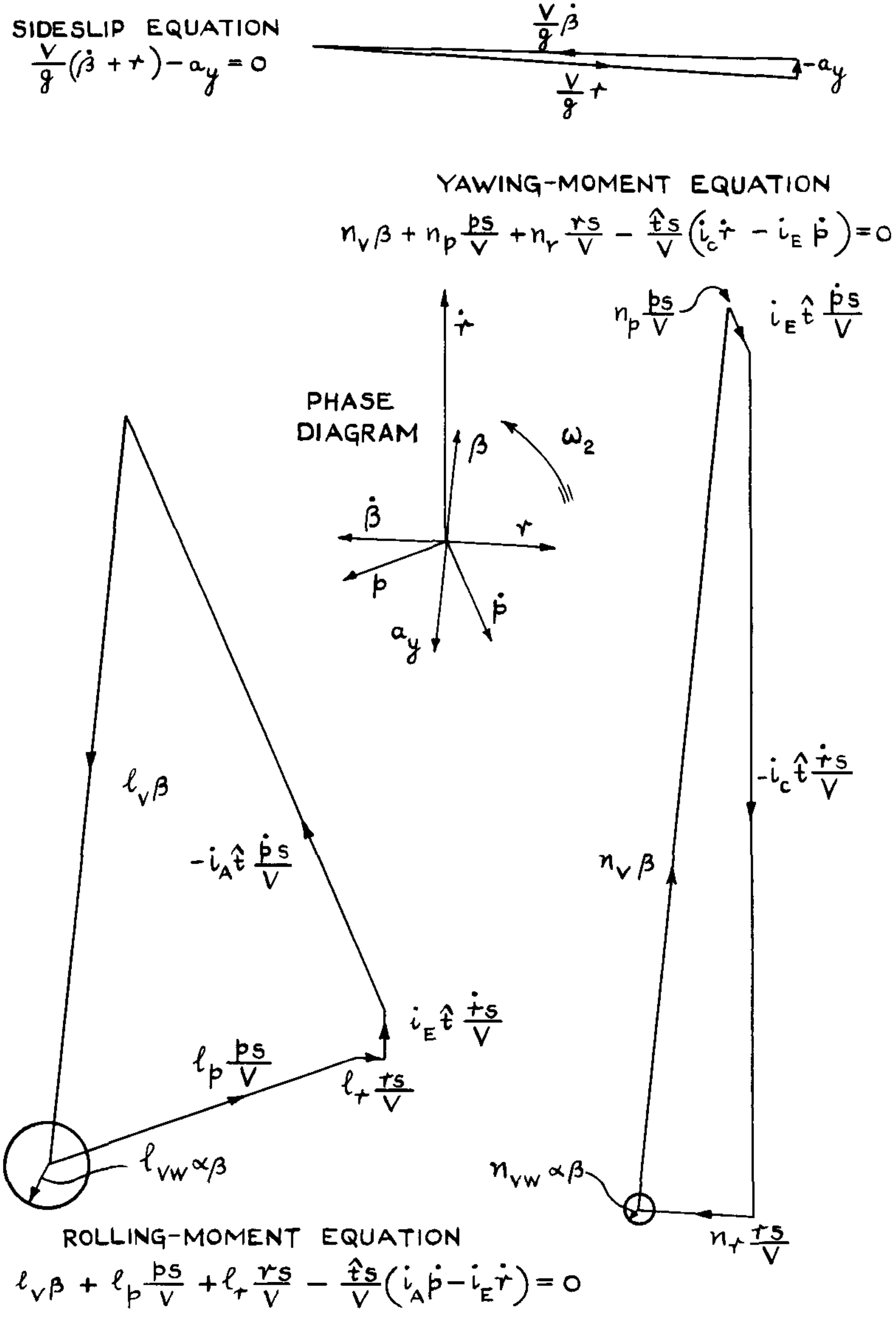

FIG. 27 VECTOR DIAGRAMS OF DUTCH-ROLL OSCILLATION AT M = 1·05 (MODEL 8)

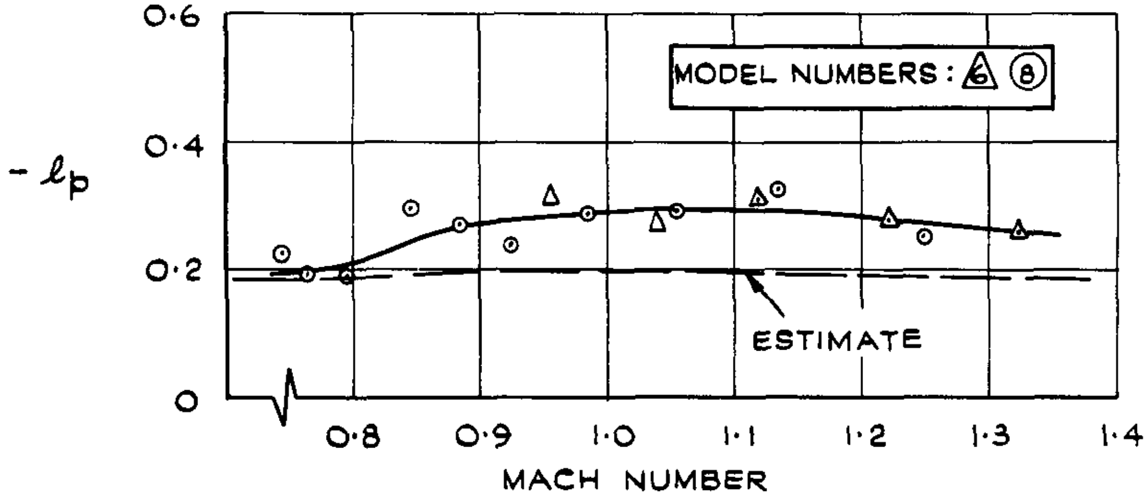

FIG. 28 ROLL-DAMPING DERIVATIVE ℓ_p

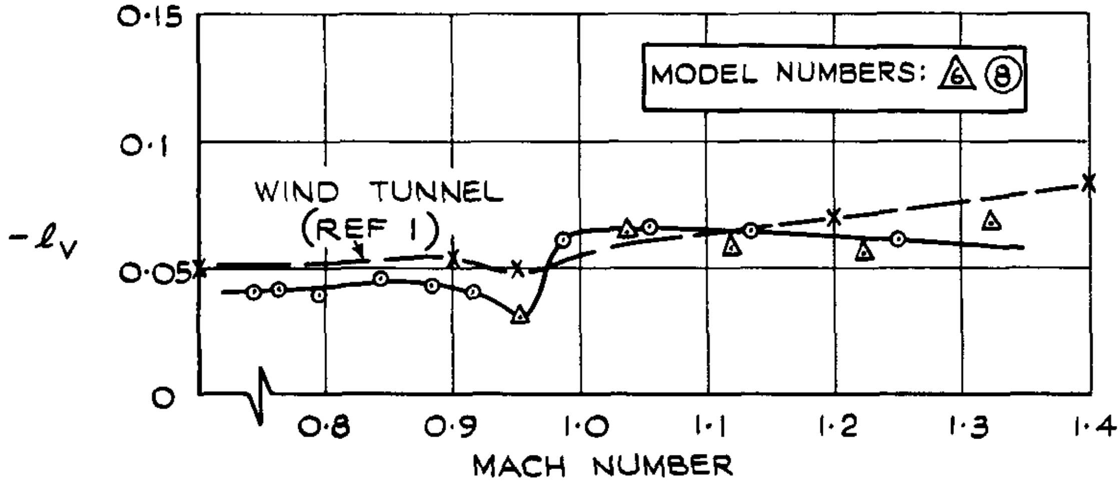

FIG. 29 ROLLING-MOMENT DERIVATIVE ℓ_v

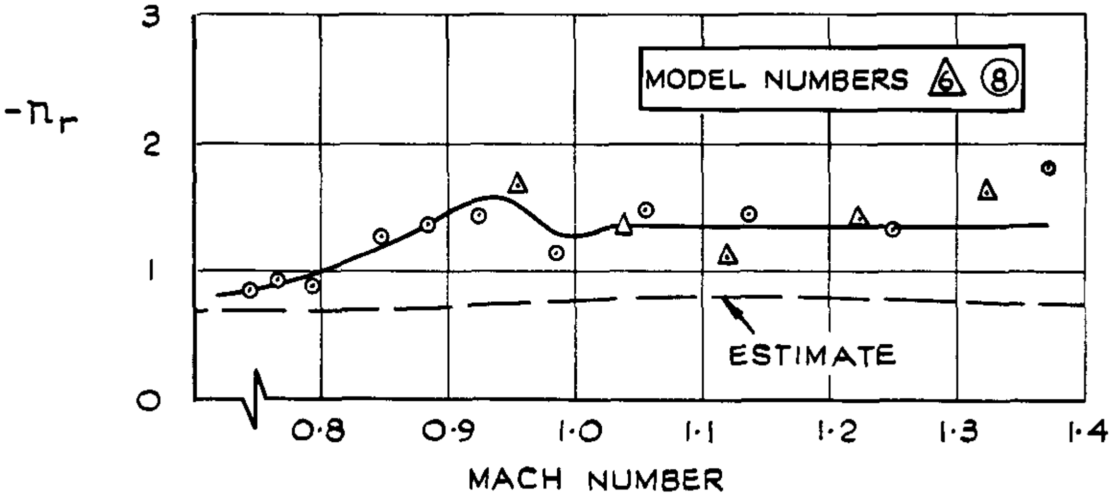

FIG. 30 YAW-DAMPING DERIVATIVE n_r

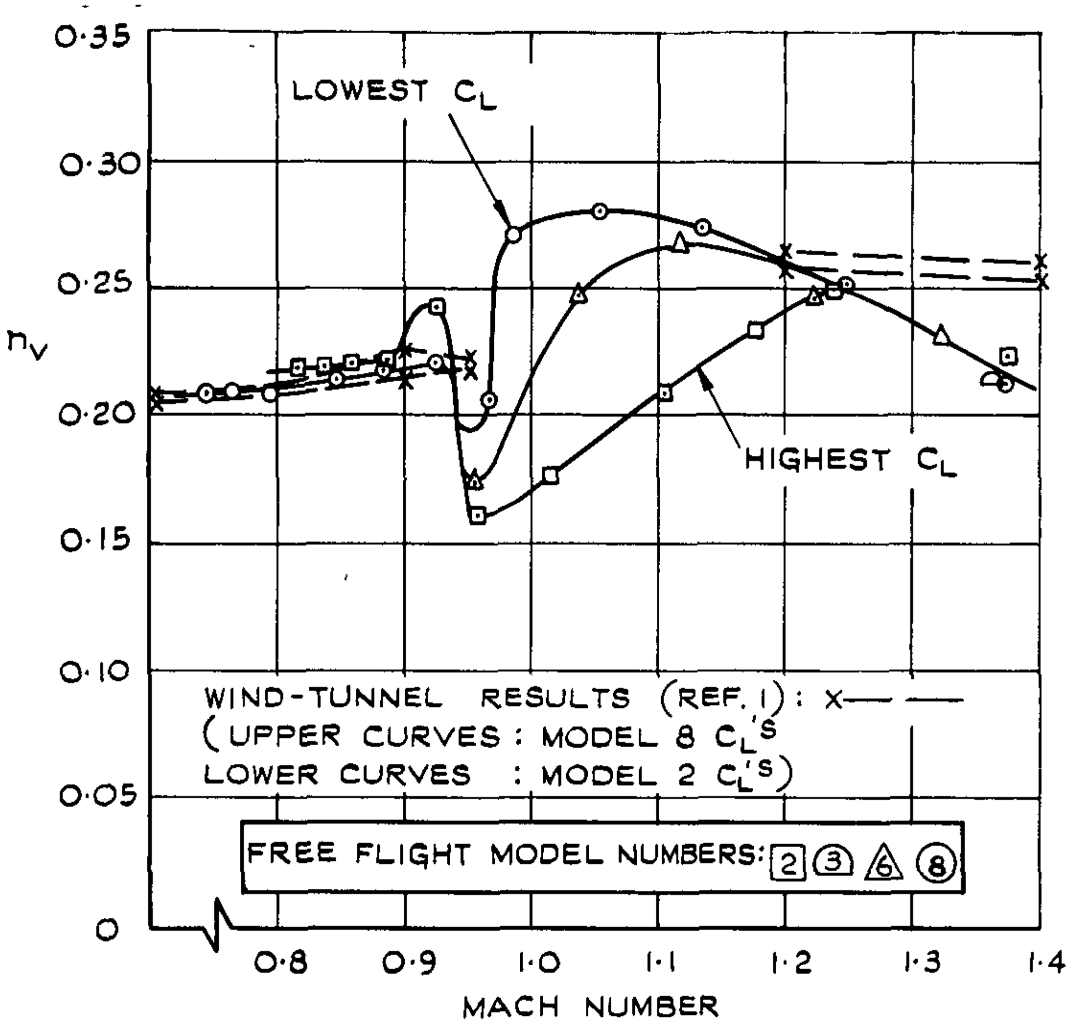

FIG. 31 YAWING-MOMENT DERIVATIVE n_v

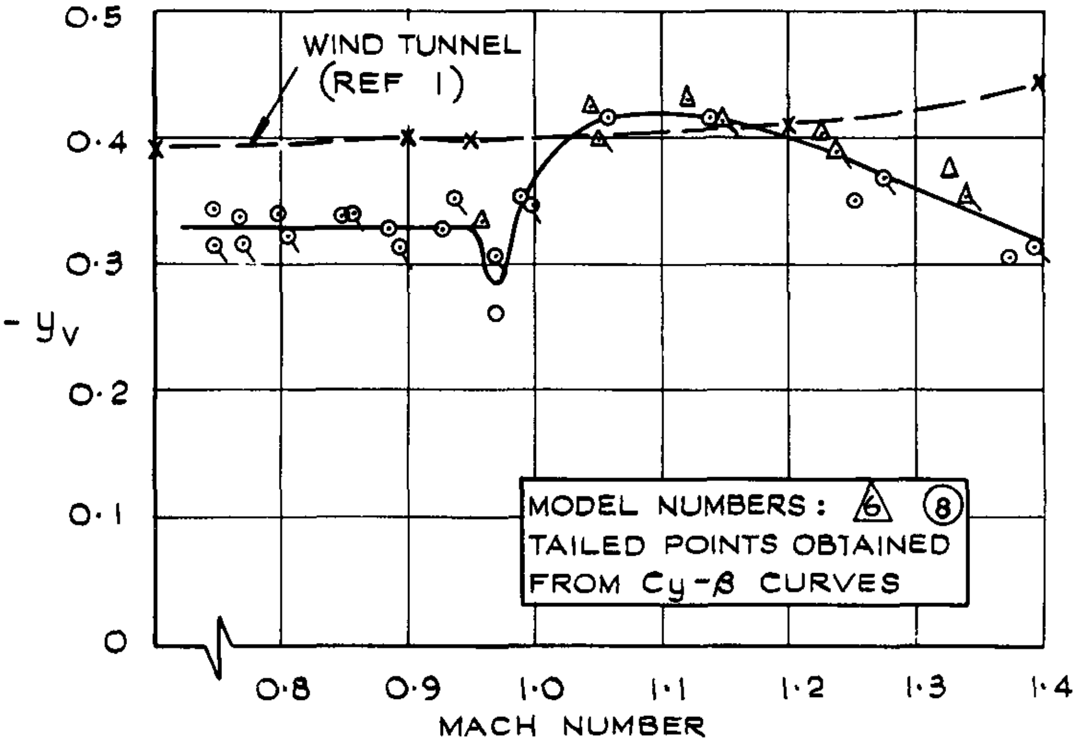

FIG. 32 SIDE-FORCE DERIVATIVE y_v

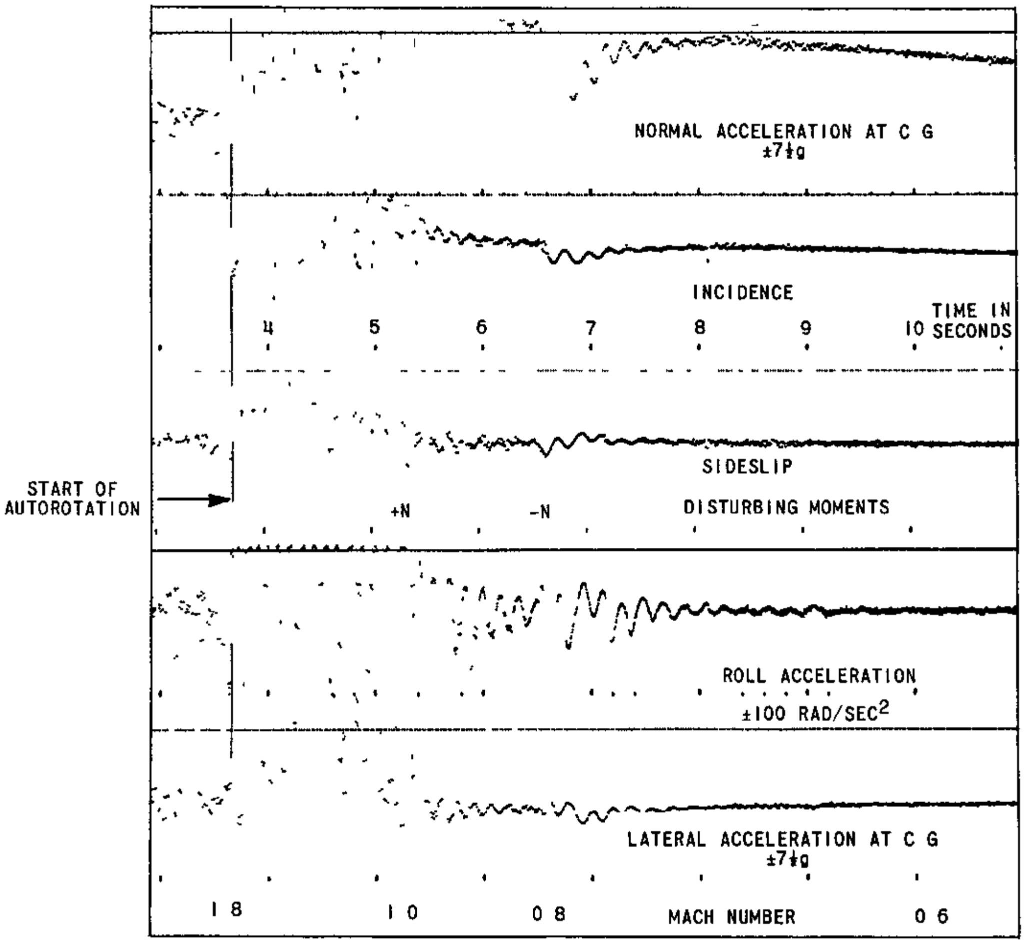

a Supersonic (Model 4)

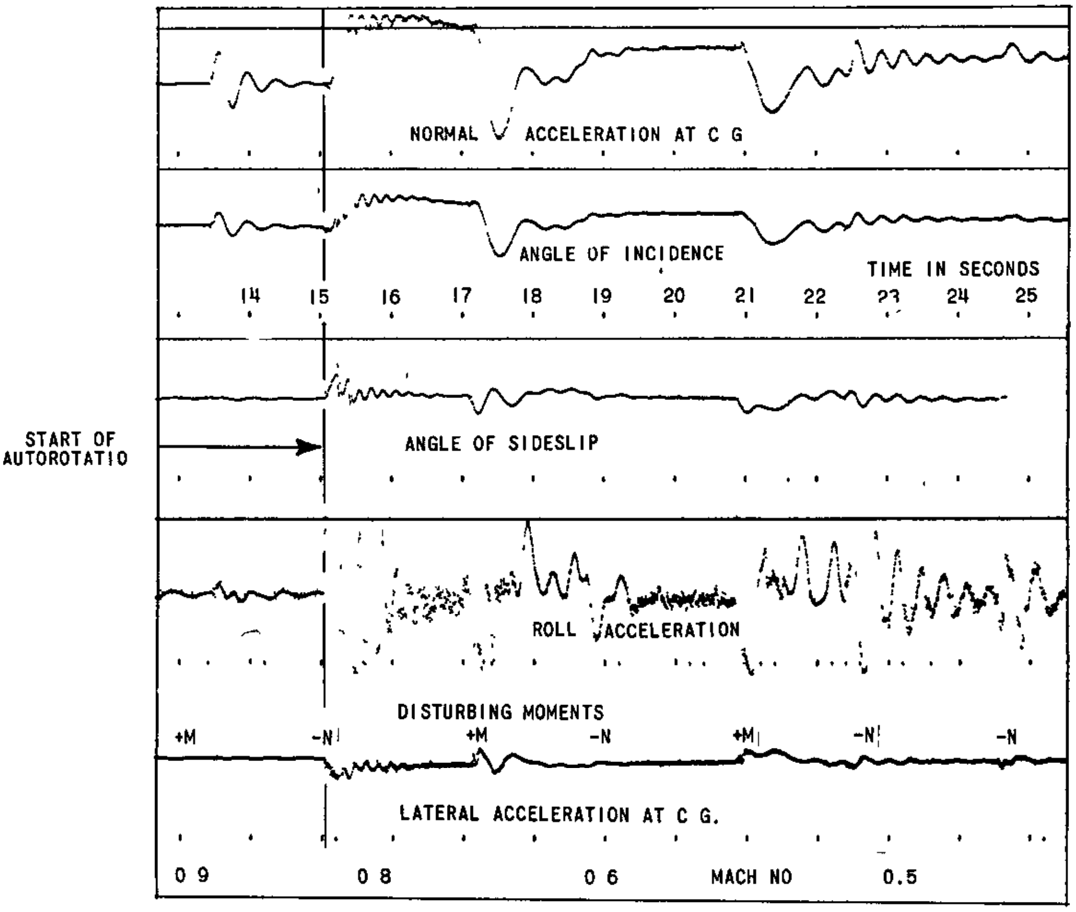

b Subsonic (Model 6)

Fig.33. Records of behaviour during autorotation

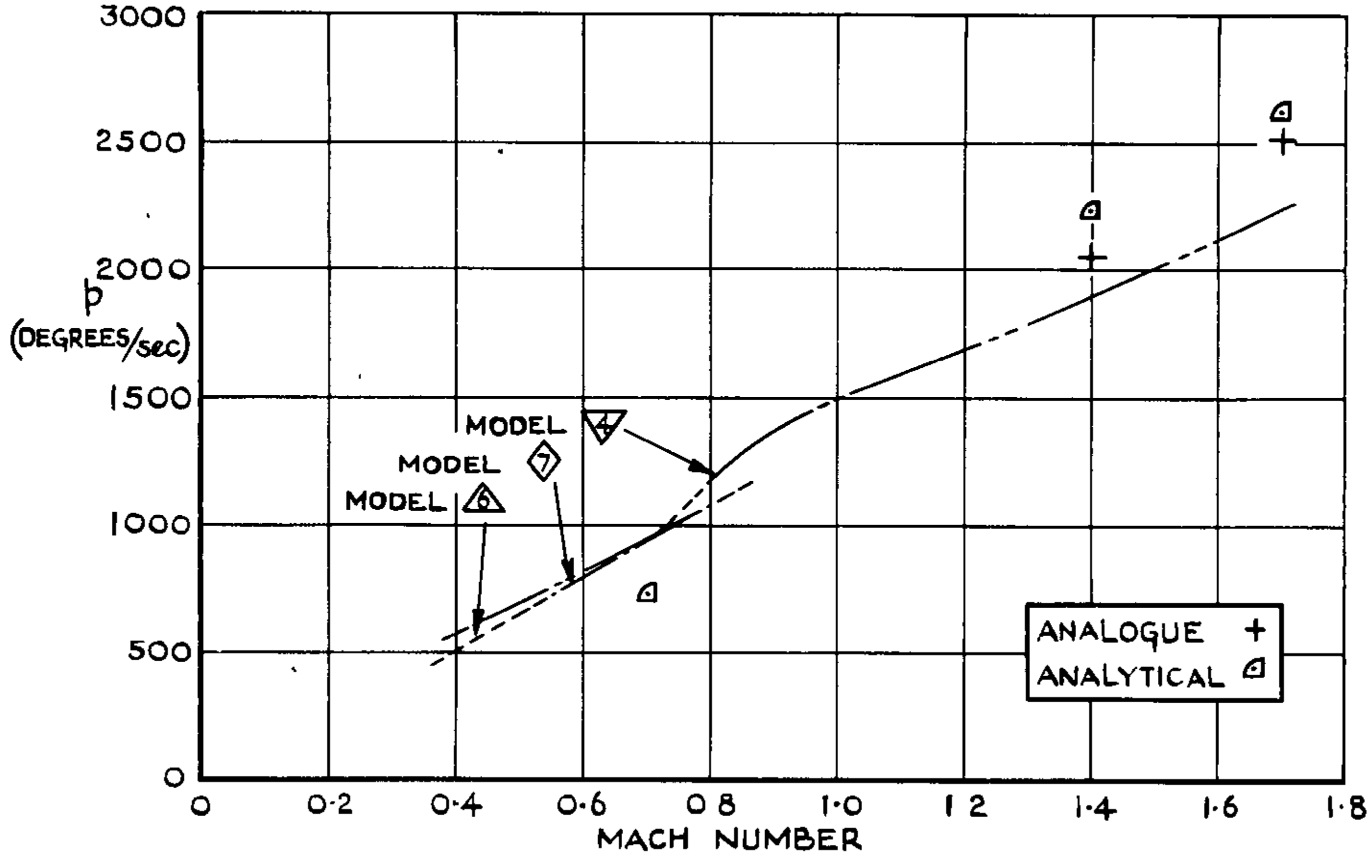

FIG. 34 MEAN RATE OF AUTOROTATION

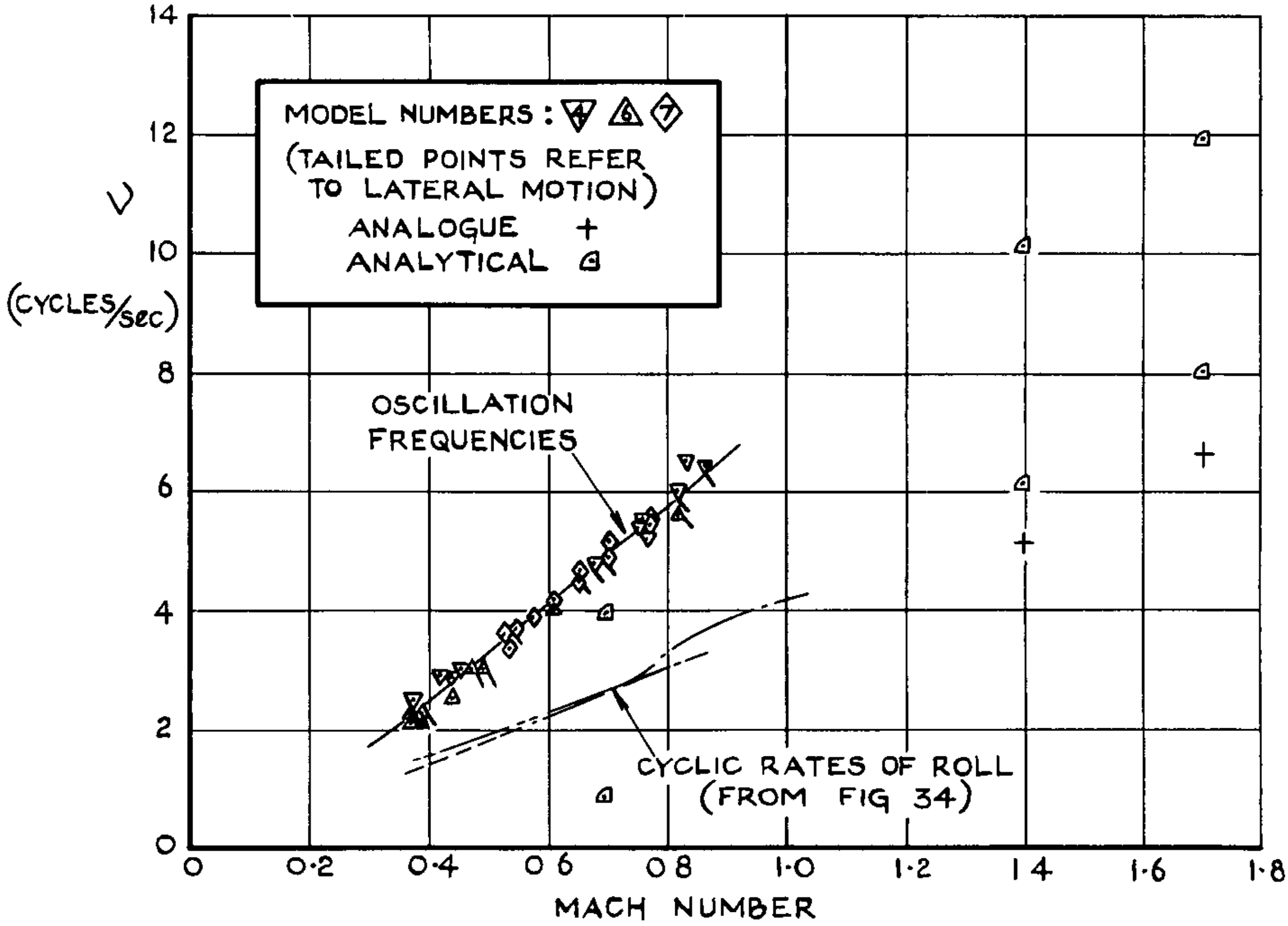

FIG. 35 FREQUENCIES OF COUPLED OSCILLATIONS DURING AUTOROTATION

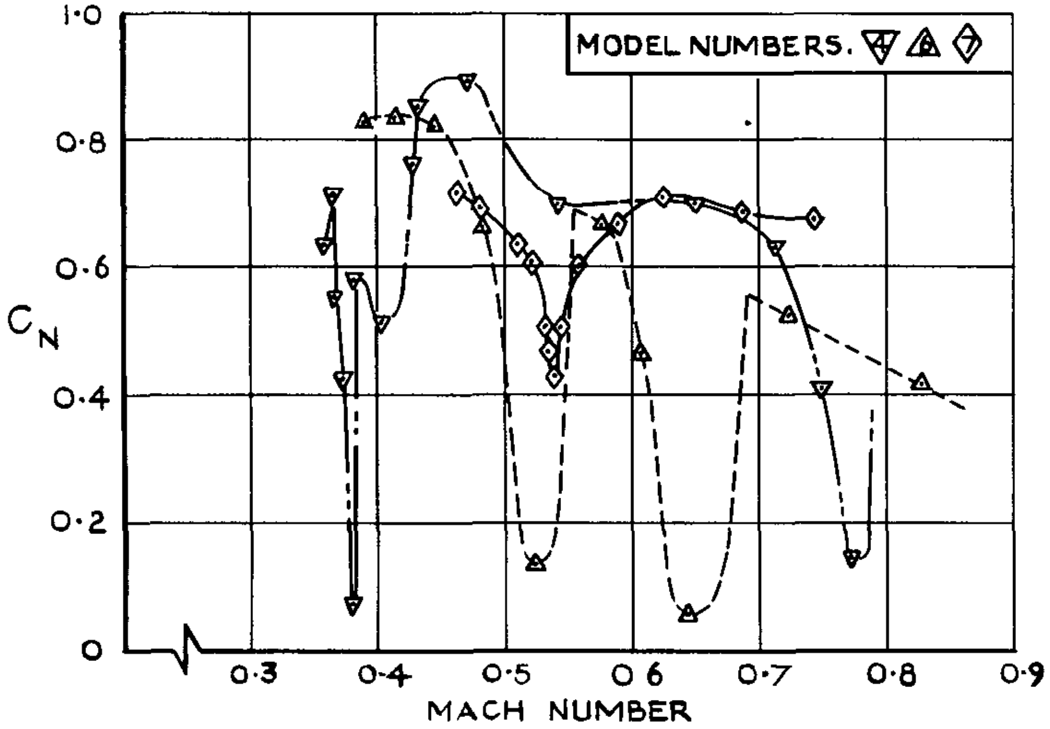

FIG. 36 NORMAL–FORCE COEFFICIENTS DURING AUTOROTATION

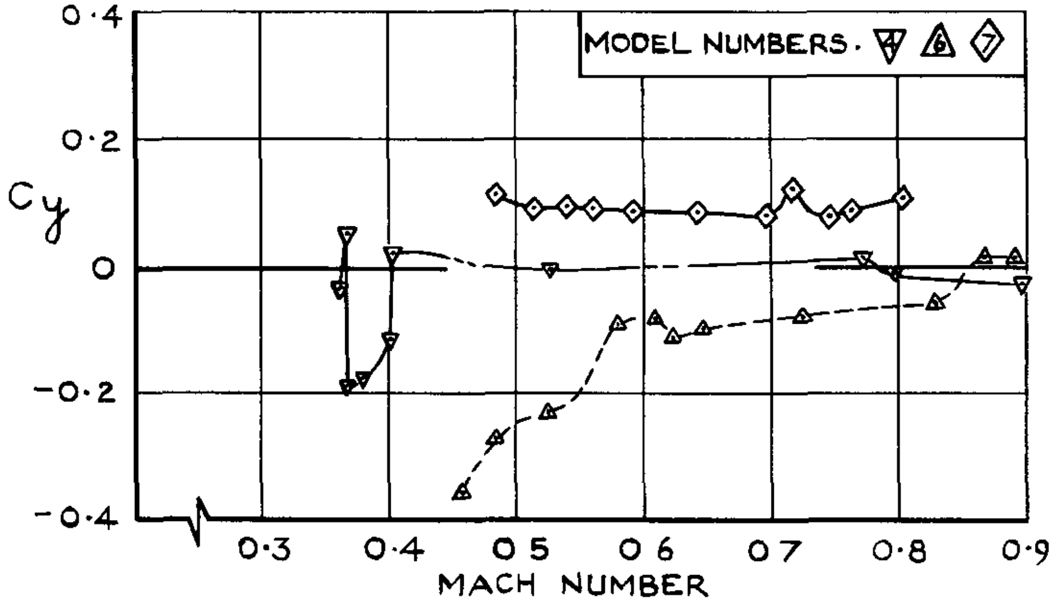

FIG. 37 SIDE–FORCE COEFFICIENTS DURING AUTOROTATION

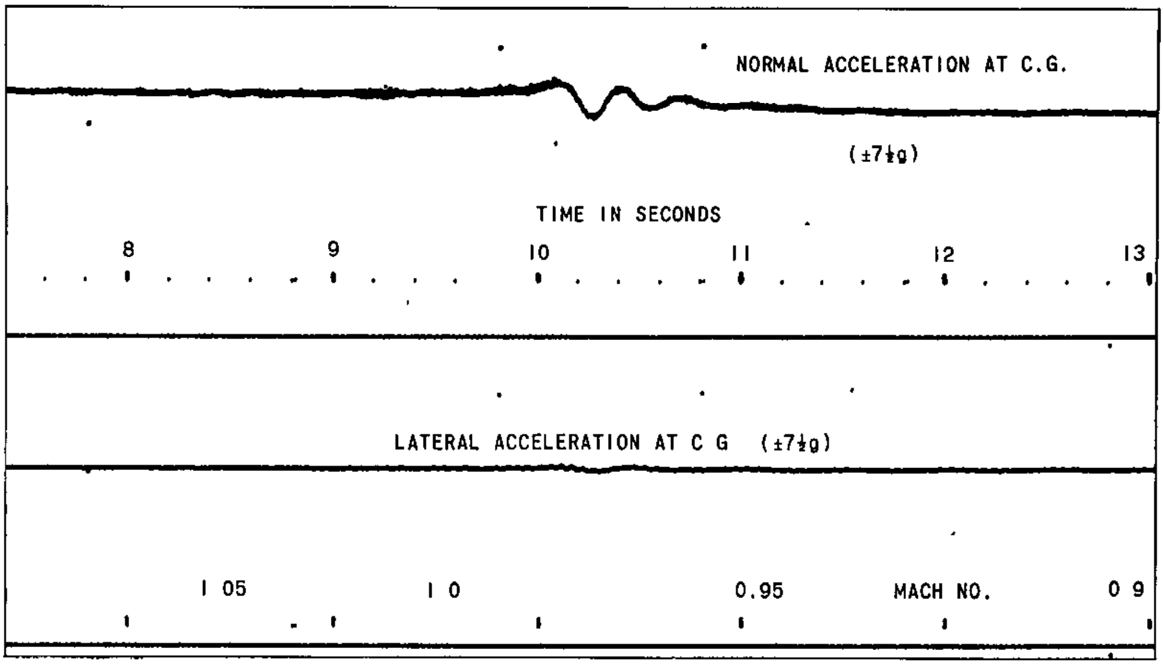

Fig 38. Oscillation excited by the transonic trim change (Model 3)

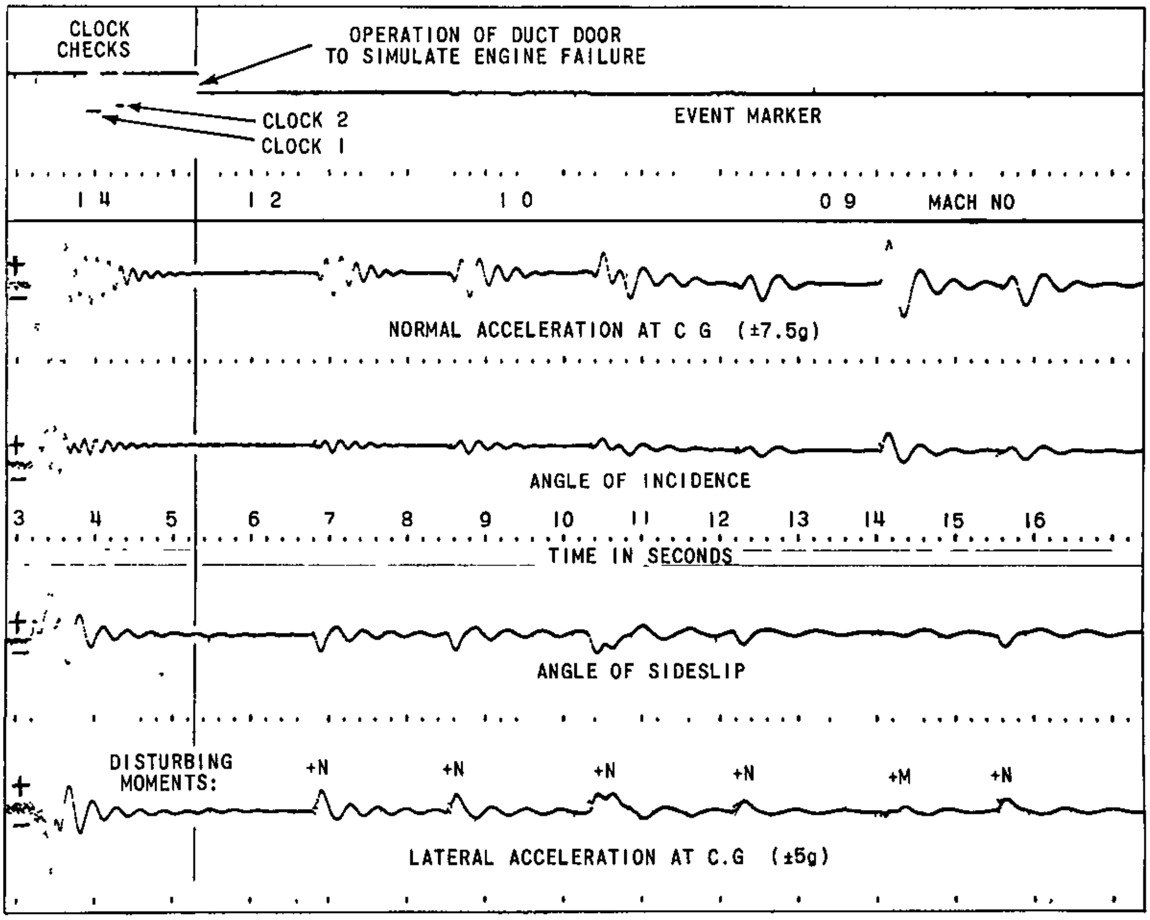

Fig.39. Effects of simulated engine failure at M=1.295. (Model 7)

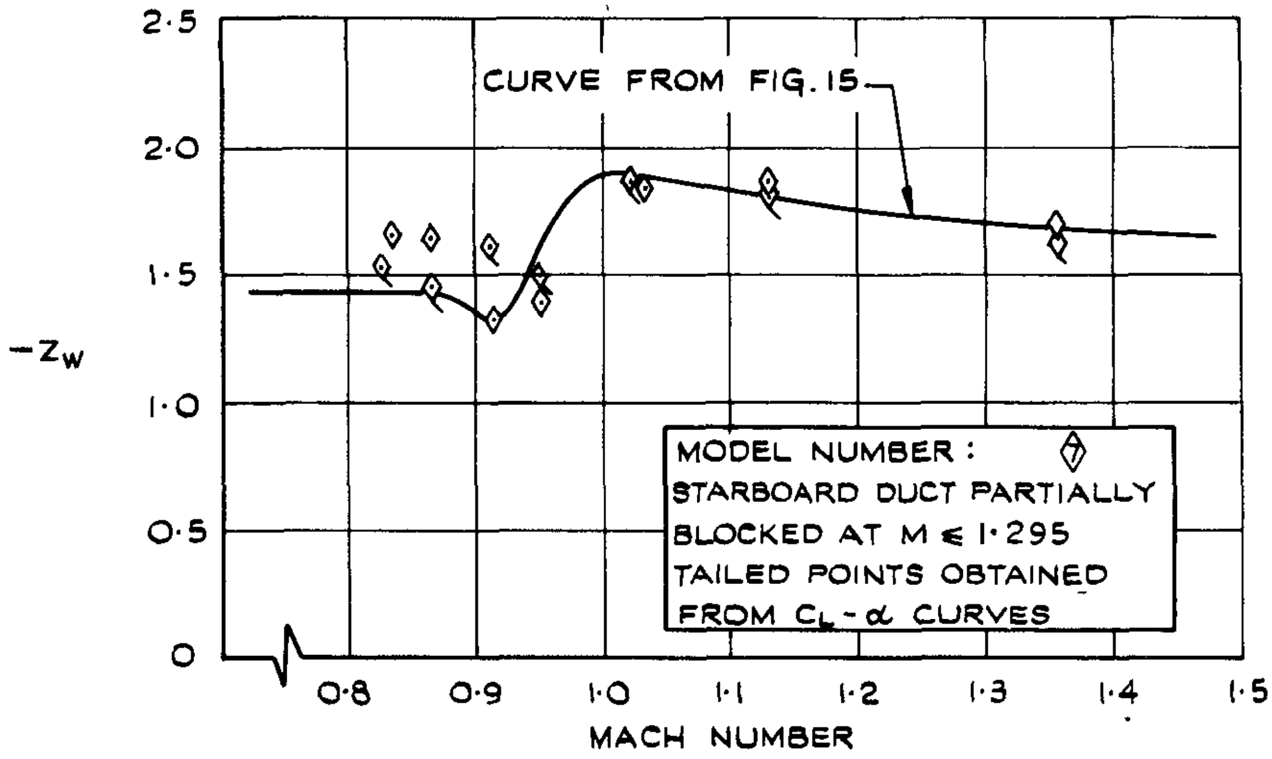

FIG. 40 EFFECT OF SIMULATED IDLE ENGINE ON z_W

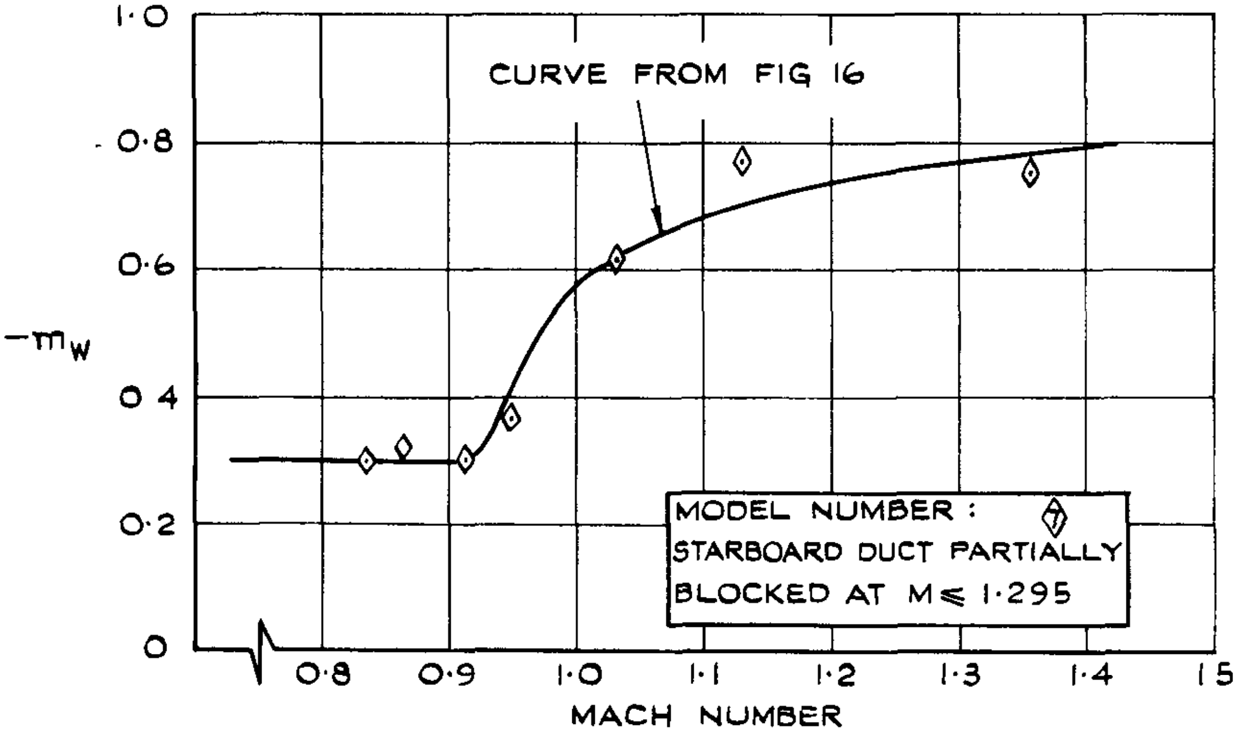

FIG 41 EFFECT OF SIMULATED IDLE ENGINE ON m_W

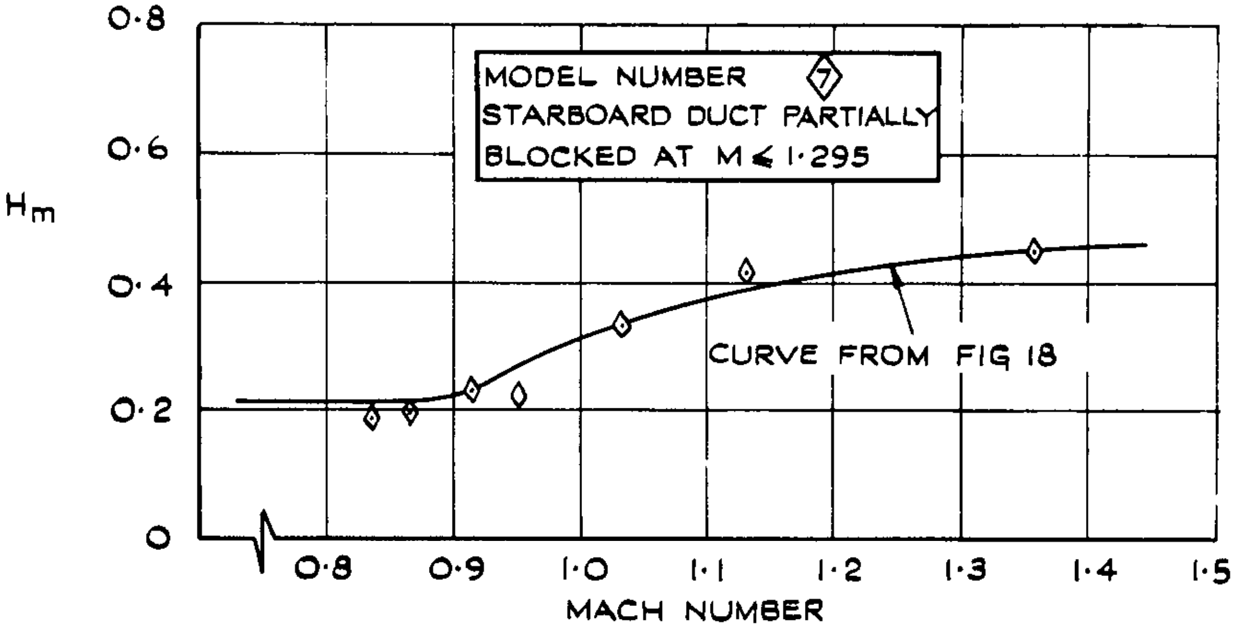

FIG. 42 EFFECT OF SIMULATED IDLE ENGINE ON MANOEUVRE MARGIN

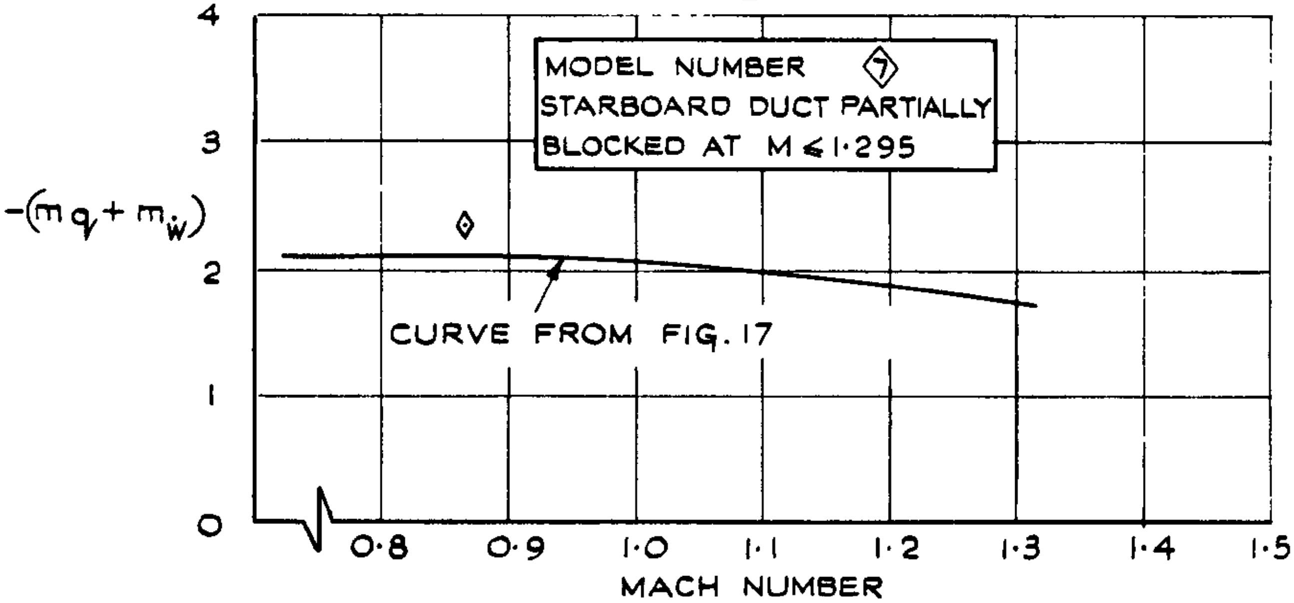

FIG. 43 EFFECT OF SIMULATED IDLE ENGINE ON ROTARY DAMPING IN PITCH

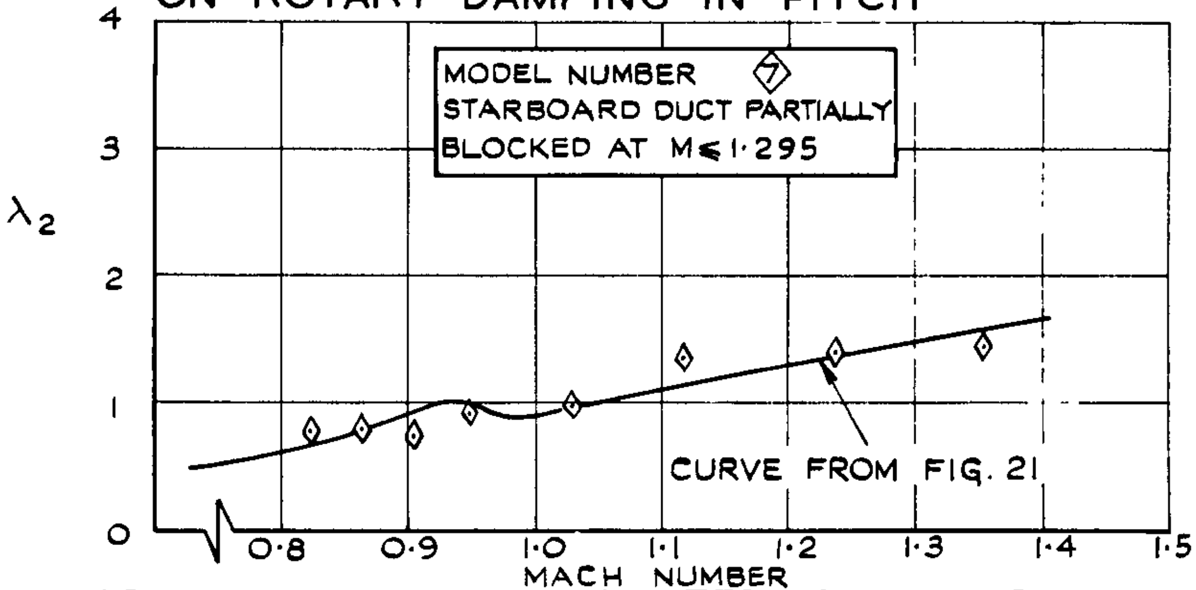

FIG. 44 EFFECT OF SIMULATED IDLE ENGINE ON LATERAL DAMPING

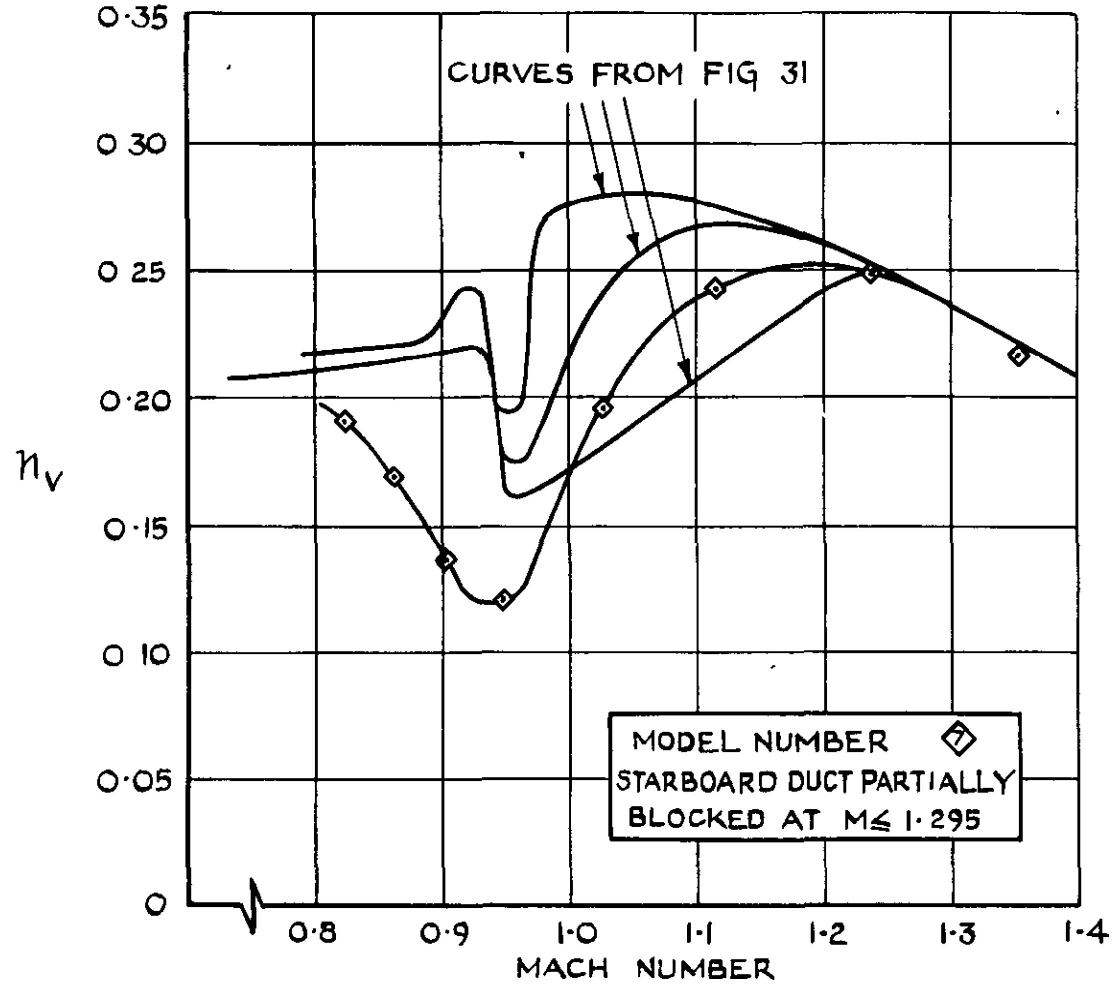

FIG. 45 EFFECT OF SIMULATED IDLE ENGINE ON n_v

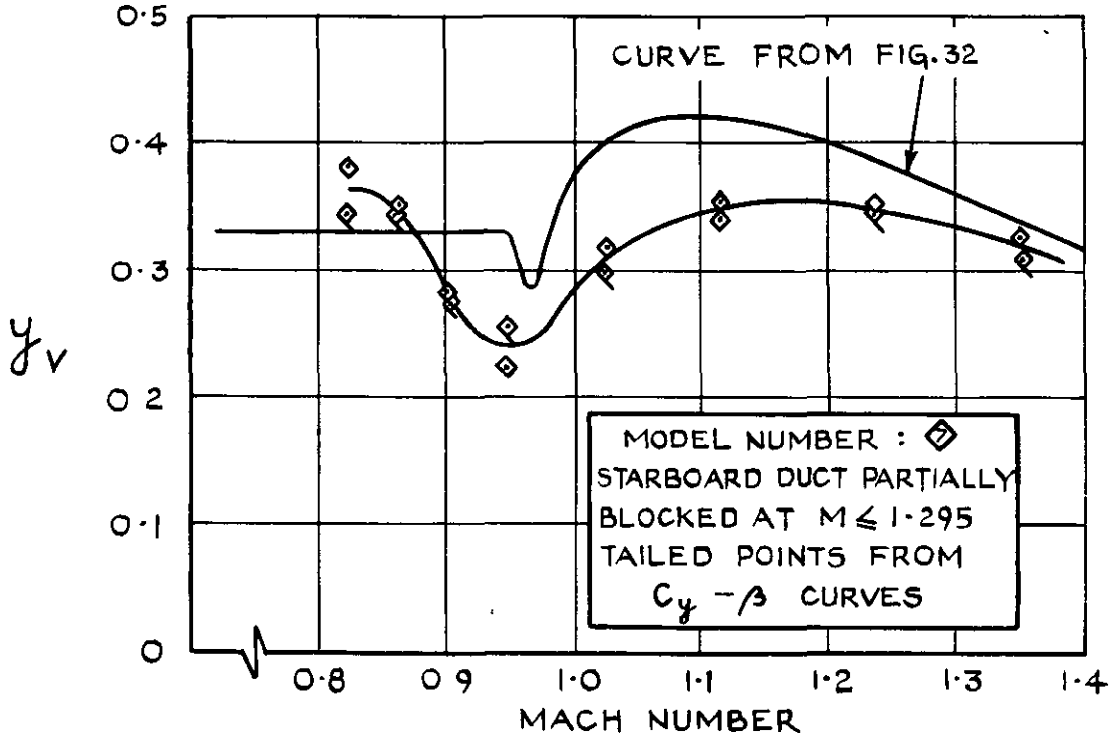

FIG. 46 EFFECT OF SIMULATED IDLE ENGINE ON y_v

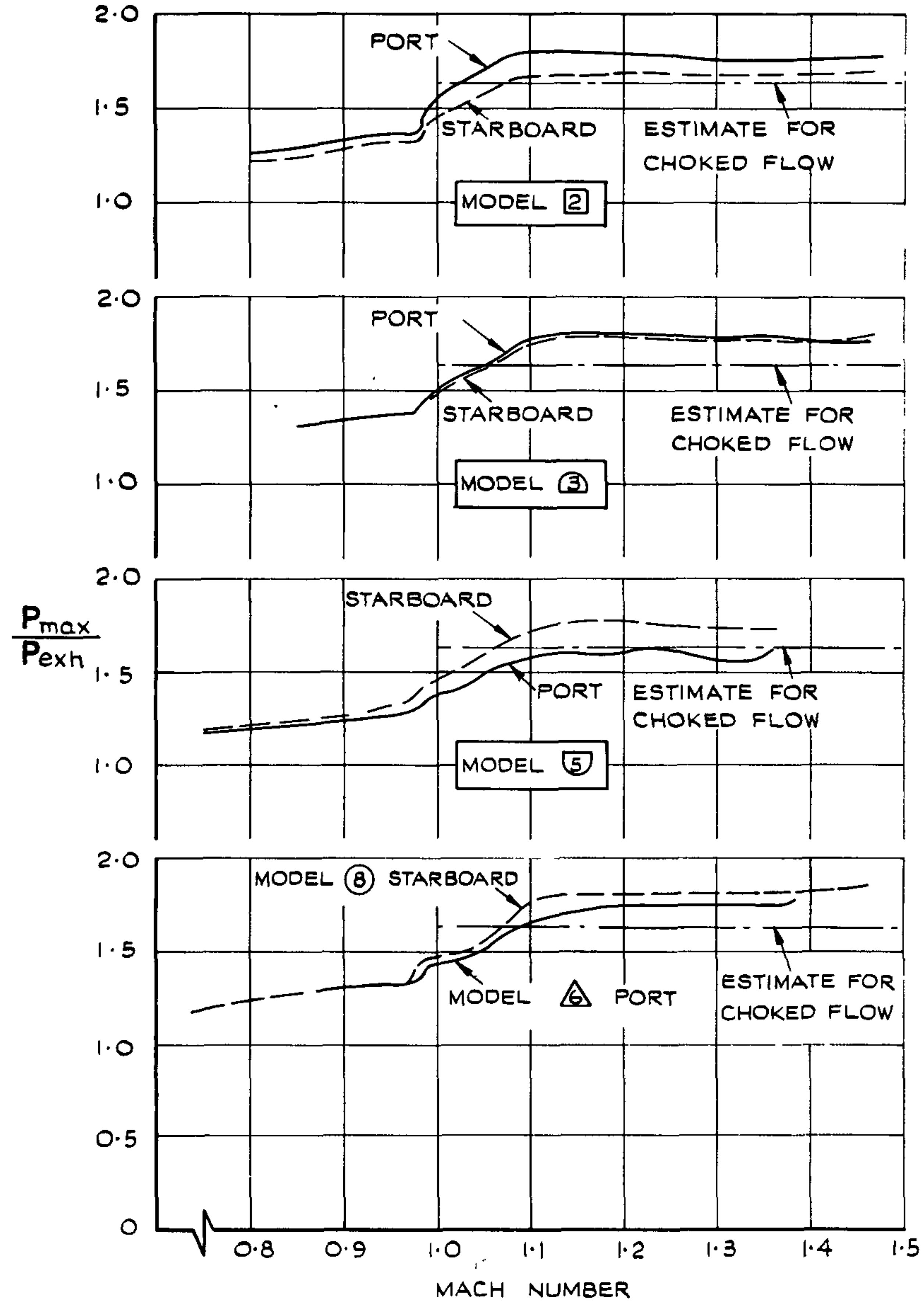

FIG. 47 DUCT INTERNAL PRESSURE RATIO

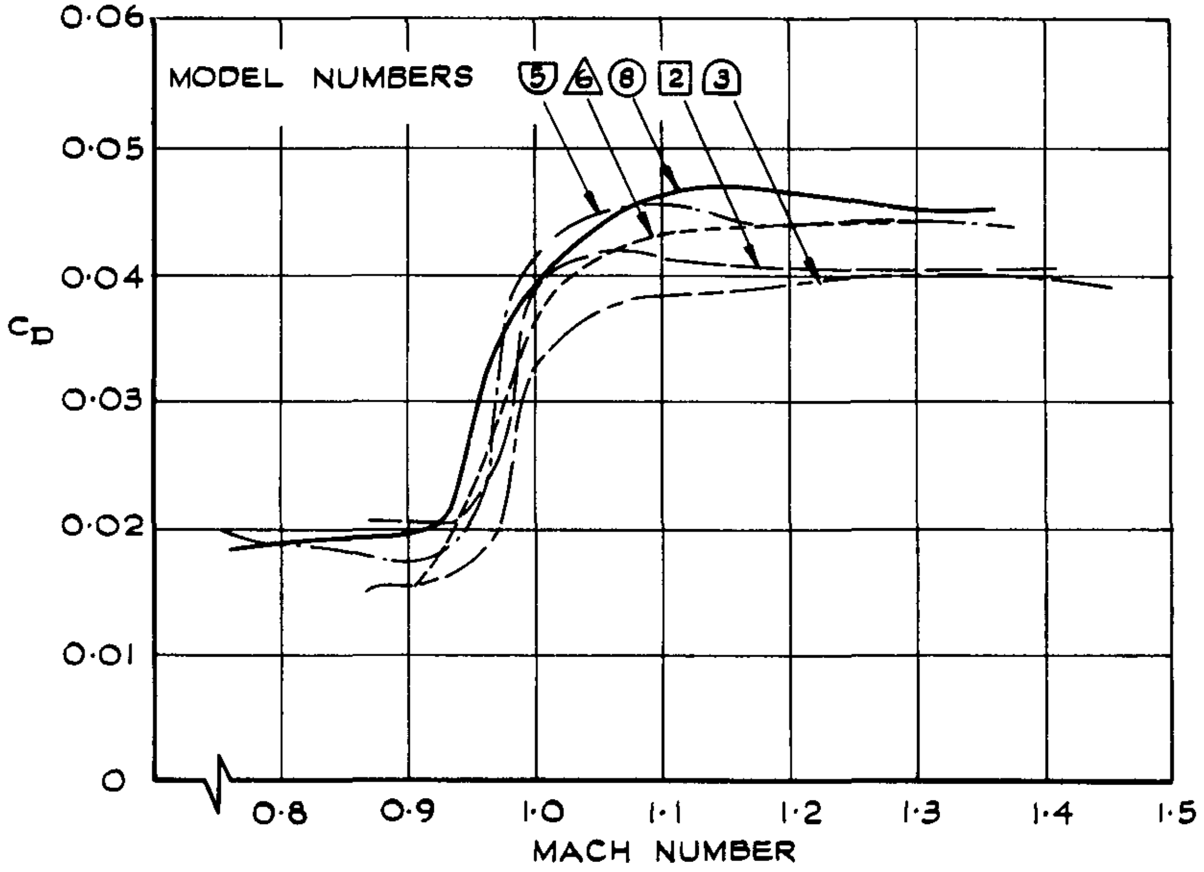

FIG. 48 TOTAL DRAG COEFFICIENT

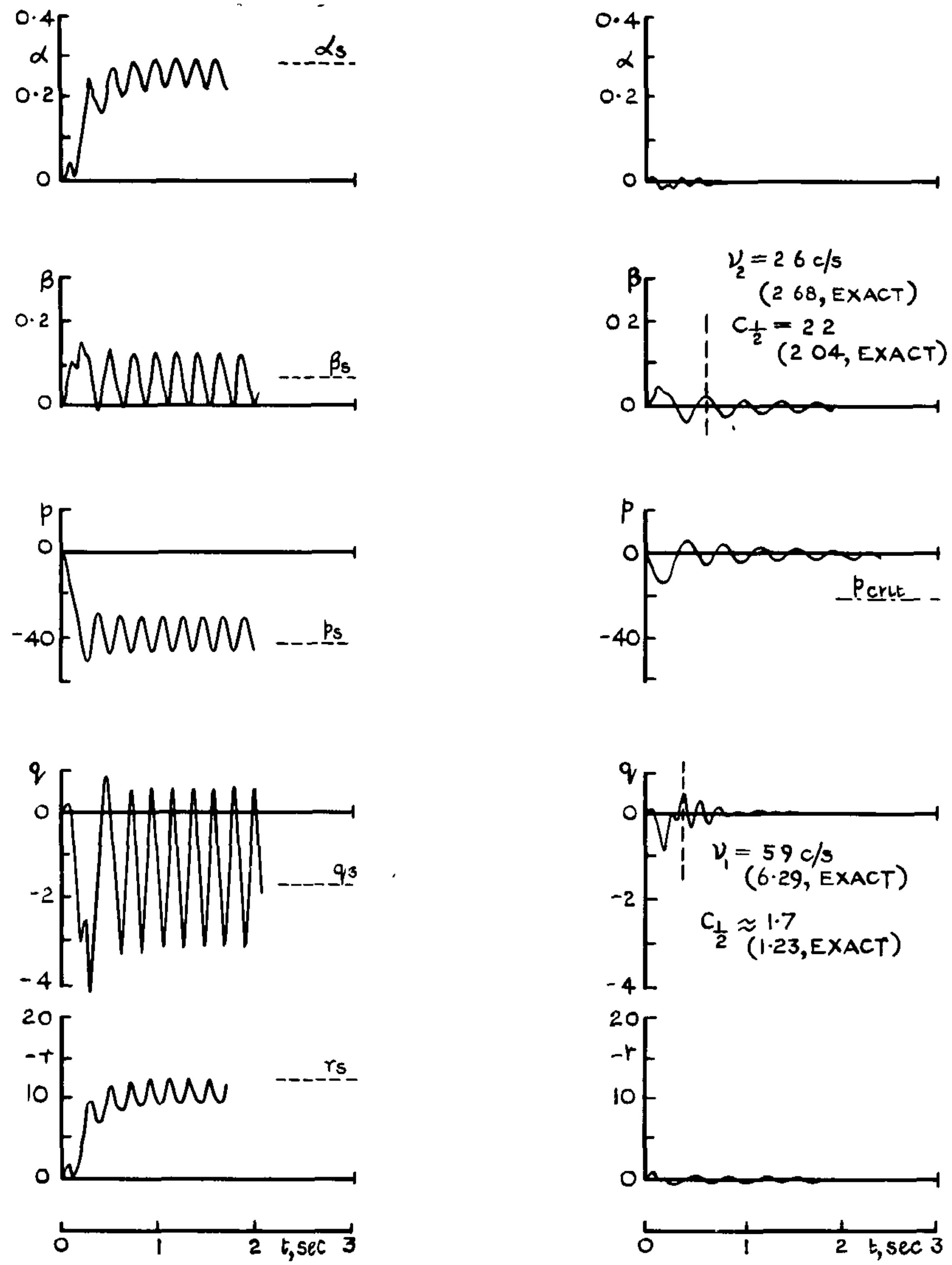

(a) $N_B = -408$ lb ft. FOR 0 07 sec
COMPARISON BETWEEN COUPLED
OSCILLATION AND APPROXIMATE
STEADY STATE VALUES

(b) $N_B = -204$ lb ft FOR 0·07 sec
COMPARISON BETWEEN FREQUENCIES
AND DAMPINGS FOR SEPARATED
OSCILLATIONS WITH EXACT VALUES

FIG. 49 THEORETICAL EFFECT OF HALVING PULSE–ROCKET YAWING MOMENT WITH c.g AT $0{\cdot}44\,\bar{c}$ (M=1·6)

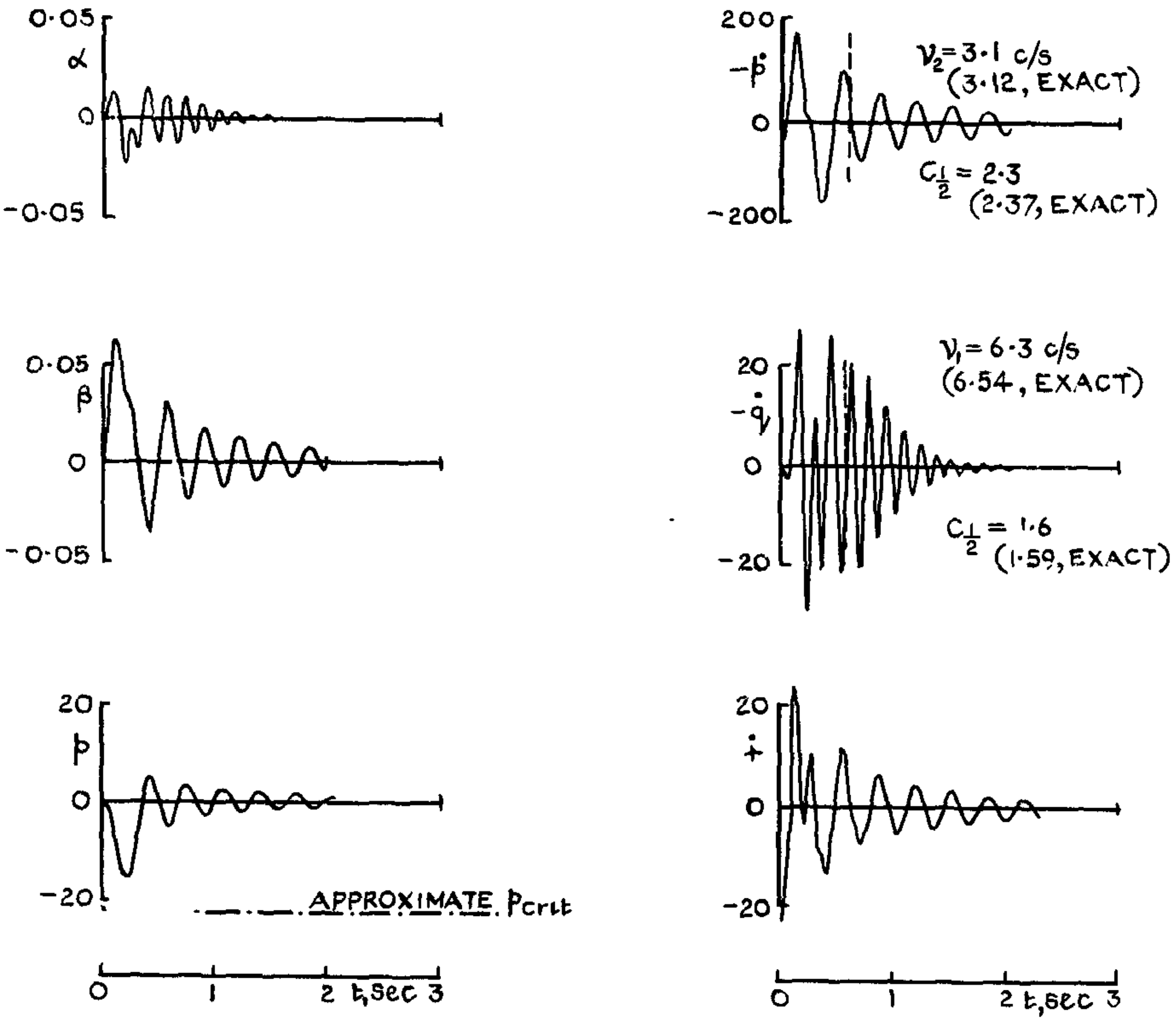

L_B = + 35 lb. ft, N_B = − 378 lb ft, AND Y_B = + 140 lb wt FOR 0·07 sec

FIG. 50 THEORETICAL RESPONSE TO LATERAL PULSE-ROCKET DISTURBANCE WITH c.g. AT 0·28$\bar{c}$ (M=1·6)

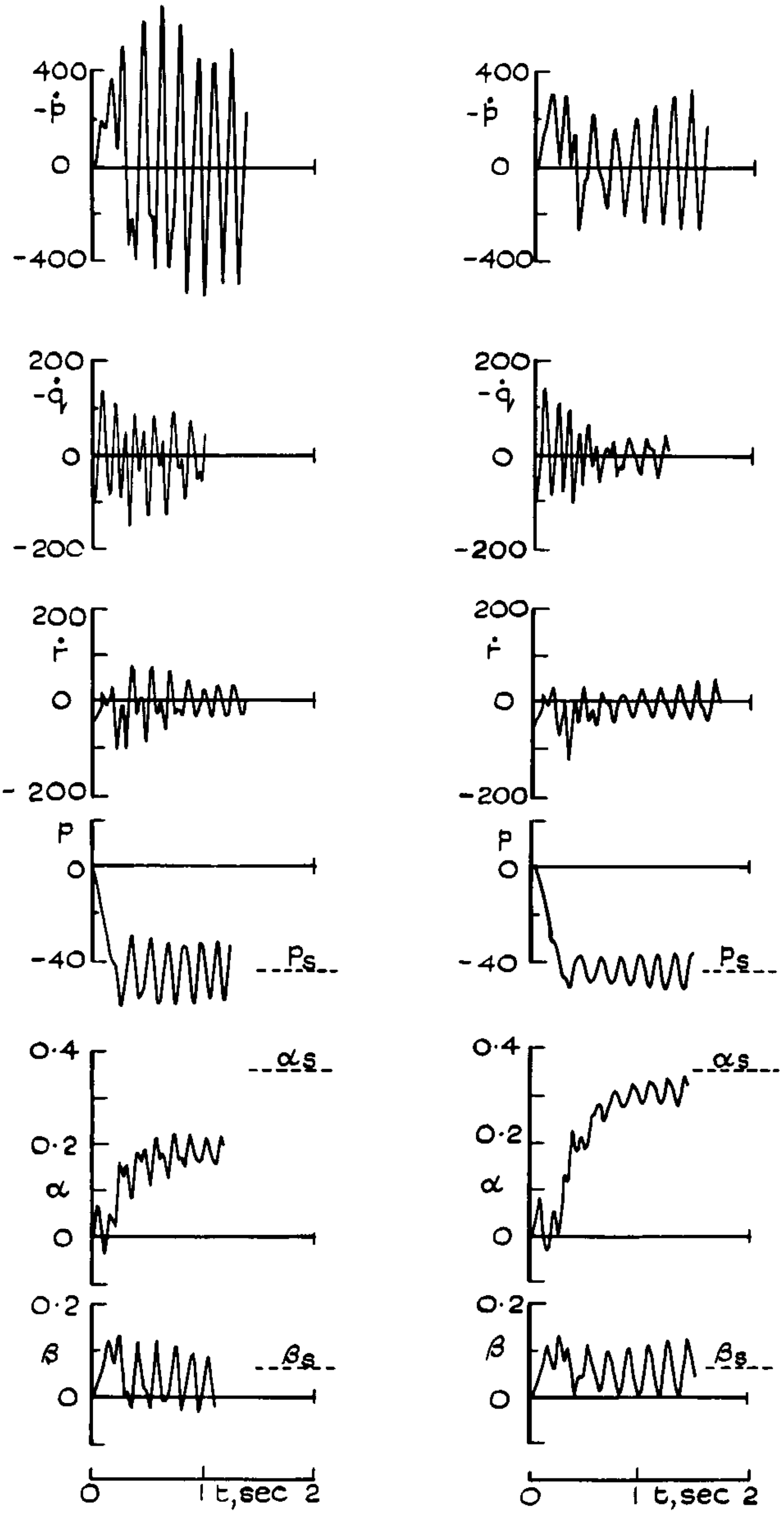

(i) $\ell_{vw} = -0.4$ (ii) $\ell_{vw} = 0$

$M_D = +840$ lb ft, $N_D = -560$ lb ft FOR 0·05 sec, $L_a = 13\cdot5$ lb ft

FIG. 51 (a) THEORETICAL RESPONSE TO DISTURBANCE CAUSED BY BOOSTER-ROCKET SEPARATION, WITH c.g AT $0\cdot264\bar{c}$ ($M=1\cdot7$)

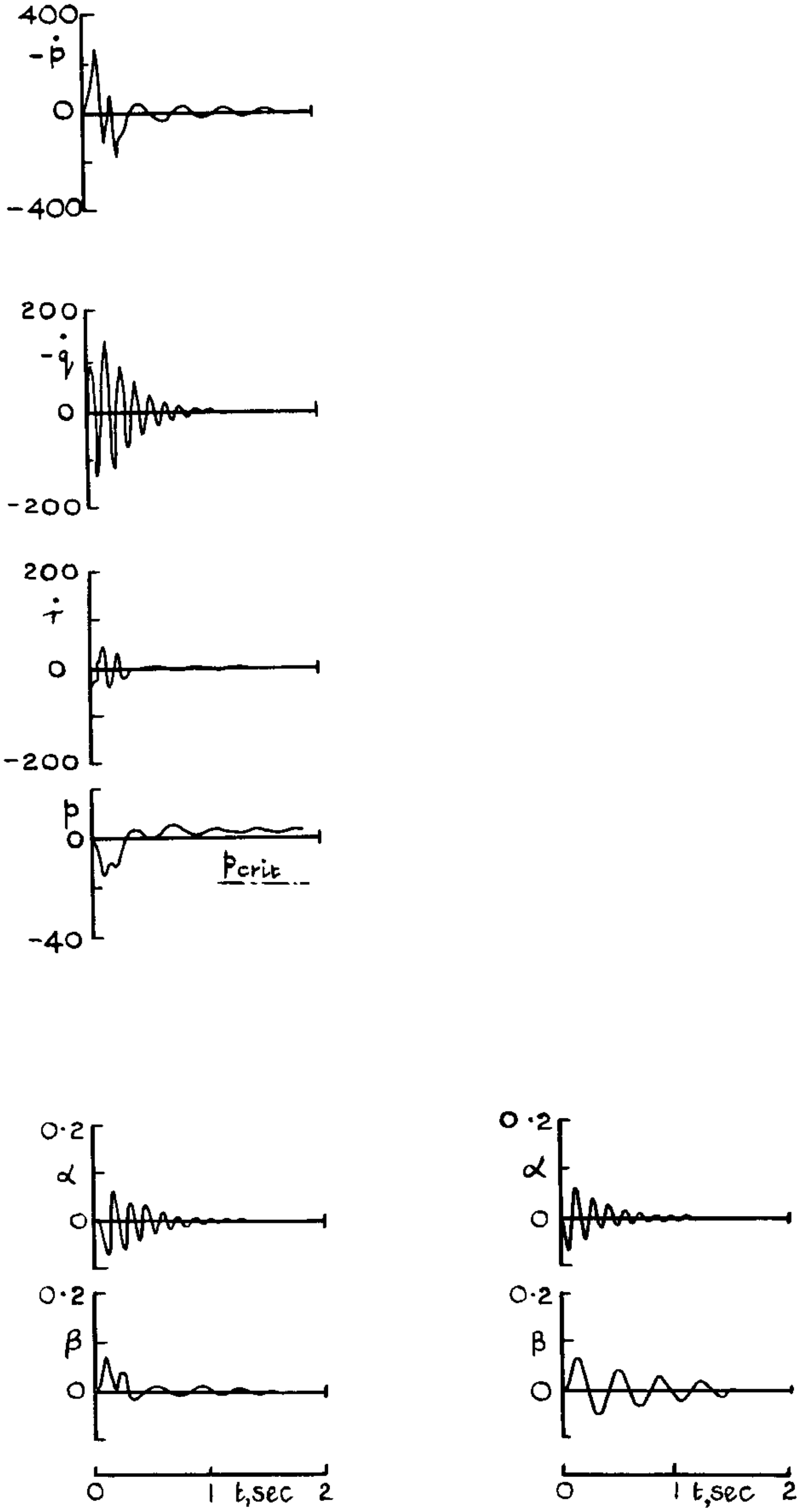

(b) $M_D = -840$ lb ft. $N_D = -560$ lb ft FOR 0·05 sec, $L_a = 13\ 5$ lb. ft.

(c) UNCOUPLED RESPONSES TO APPLIED MOMENTS

FIG. 51 (b & c) THEORETICAL RESPONSE TO DISTURBANCE CAUSED BY BOOSTER-ROCKET SEPARATION, WITH c.g. AT 0·264 $\bar{c}$ (M=1·7)

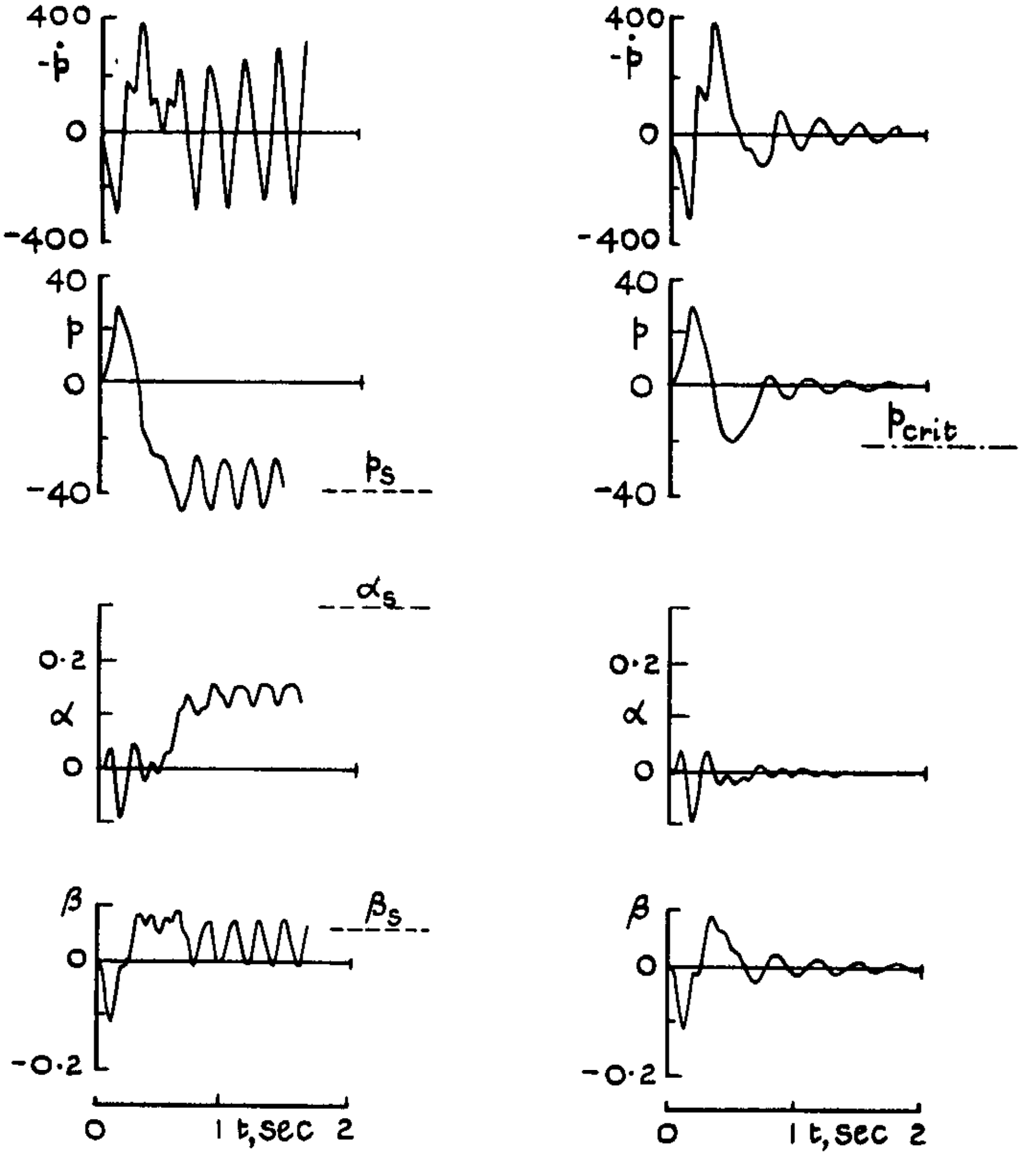

p_a = 1·75 rad/sec

p_a = 0

N_B = + 730 lb ft.
L_B = + 50 lb ft
Y_B = 200 lb wt
} FOR 0·05 sec

FIG. 52(a) THEORETICAL RESPONSES TO NEAR-CRITICAL LATERAL DISTURBANCES, WITH c.g. AT 0·264 $\bar{c}$ (M=1·4)

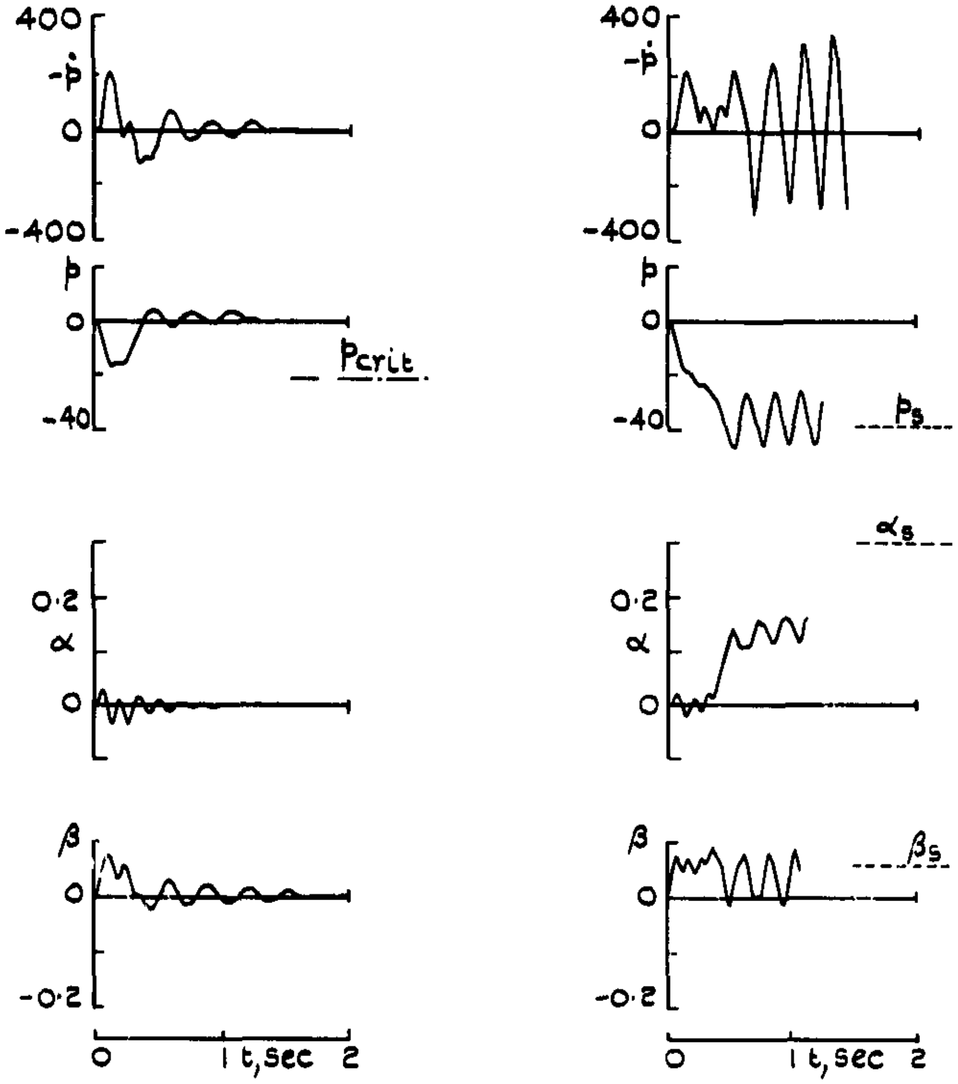

$p_a = 1{\cdot}75$ rad sec $\qquad$ $p_a = 0$

$$\left.\begin{array}{l} N_B = -480 \text{ lb. ft.} \\ L_B = 0 \\ Y_B = 200 \text{ lb wt} \end{array}\right\} \text{FOR } 0{\cdot}05 \text{ sec}$$

FIG. 52(b) THEORETICAL RESPONSES TO NEAR-CRITICAL LATERAL DISTURBANCES, WITH cg AT 0·264 $\bar{c}$ (M=1·4)

Printed in England for Her Majesty's Stationery Office by the
Royal Aircraft Establishment, Farnborough. Dd.125875 K.5

A.R.C. C.P. No. 918 533.6.013.412/413 :
November 1965 533.6.011.35/5

Hunt, G.K.
Ross, Jean. A. (Appendix)

FREE-FLIGHT MODEL MEASUREMENTS OF THE DYNAMIC STABILITY OF A SUPERSONIC STRIKE AIRCRAFT (TSR2)

Longitudinal and lateral stability derivatives have been obtained in free flight from eight 1/12-scale models of the TSR2, at Mach numbers between 0.7 and 1.4 and Reynolds numbers between 7 and 15 million.

The measurements indicate some loss of longitudinal and lateral stability at transonic speeds, and the loss of yaw stiffness n_v is shown to be dependent on C_L. At supersonic speeds the sideslip derivatives ℓ_v, n_v and y_v diminish continuously with increasing Mach number.

/The

A.R.C. C.P. No. 918 533.6.013.412/413 :
November 1965 533.6.011.35/5

Hunt, G.K.
Ross, Jean. A. (Appendix)

FREE-FLIGHT MODEL MEASUREMENTS OF THE DYNAMIC STABILITY OF A SUPERSONIC STRIKE AIRCRAFT (TSR2)

Longitudinal and lateral stability derivatives have been obtained in free flight from eight 1/12-scale models of the TSR2, at Mach numbers between 0.7 and 1.4 and Reynolds numbers between 7 and 15 million.

The measurements indicate some loss of longitudinal and lateral stability at transonic speeds, and the loss of yaw stiffness n_v is shown to be dependent on C_L. At supersonic speeds the sideslip derivatives ℓ_v, n_v and y_v diminish continuously with increasing Mach number.

/The

A.R.C. C.P. No. 918 533.6.013.412/413 :
November 1965 533.6.011.35/5

Hunt, G.K.
Ross, Jean. A. (Appendix)

FREE-FLIGHT MODEL MEASUREMENTS OF THE DYNAMIC STABILITY OF A SUPERSONIC STRIKE AIRCRAFT (TSR2)

Longitudinal and lateral stability derivatives have been obtained in free flight from eight 1/12-scale models of the TSR2, at Mach numbers between 0.7 and 1.4 and Reynolds numbers between 7 and 15 million.

The measurements indicate some loss of longitudinal and lateral stability at transonic speeds, and the loss of yaw stiffness n_v is shown to be dependent on C_L. At supersonic speeds the sideslip derivatives ℓ_v, n_v and y_v diminish continuously with increasing Mach number.

/The

DETACHABLE ABSTRACT CARDS

The aerodynamic effects of a sudden engine failure were produced at $M = 1.3$ on two models, but the response was negligible. The sideslip derivatives n_v and y_v were considerably reduced at transonic speeds by flying with a simulated idle engine.

Four of the models autorotated after lateral disturbances. Some of the characteristics of this behaviour have been determined from the flight records and by simulating the motion on an analogue computer.

The aerodynamic effects of a sudden engine failure were produced at $M = 1.3$ on two models, but the response was negligible. The sideslip derivatives n_v and y_v were considerably reduced at transonic speeds by flying with a simulated idle engine.

Four of the models autorotated after lateral disturbances. Some of the characteristics of this behaviour have been determined from the flight records and by simulating the motion on an analogue computer.

The aerodynamic effects of a sudden engine failure were produced at $M = 1.3$ on two models, but the response was negligible. The sideslip derivatives n_v and y_v were considerably reduced at transonic speeds by flying with a simulated idle engine.

Four of the models autorotated after lateral disturbances. Some of the characteristics of this behaviour have been determined from the flight records and by simulating the motion on an analogue computer.

C.P. No. 918

Published by
HER MAJESTY'S STATIONERY OFFICE
To be purchased from
49 High Holborn, London w.c.1
423 Oxford Street, London w.1
13A Castle Street, Edinburgh 2
109 St Mary Street, Cardiff
Brazennose Street, Manchester 2
50 Fairfax Street, Bristol 1
35 Smallbrook, Ringway, Birmingham 5
80 Chichester Street, Belfast 1
or through any bookseller

C.P. No. 918

S.O. CODE No. 23-9017-18